Technische Universität München
Lehrstuhl für Messsystem- und Sensortechnik

Laser Speckle Based Surface Measurement Techniques Relevant to Fusion Devices

Martin Jakobi

Vollständiger Abdruck der von der Fakultät für Elektrotechnik und Informationstechnik der Technischen Universität München zur Erlangung des akademischen Grades eines

Doktor-Ingenieurs

genehmigten Dissertation.

Vorsitzender:		Univ.-Prof. Dr.-Ing. G. Färber
Prüfer der Dissertation:	1.	Univ.-Prof. Dr.-Ing. habil. A.W. Koch
	2.	Hon.-Prof. Dr. rer. nat. R. Wilhelm

Die Dissertation wurde am 05.05.2000 bei der Technischen Universität München eingereicht und durch die Fakultät für Elektrotechnik und Informationstechnik am 07.08.2000 angenommen.

Abstract

In this thesis, laser-speckle-based surface measurement techniques, which are relevant to fusion, have been investigated. In fusion devices plasma-wall interactions cause surface microrelief changes, such as erosion or redeposition. Phase-shifting speckle interferometry has been examined in order to detect surface microrelief changes and to determine erosion depths or redeposition heights. A novel spatial phase-shifting speckle interferometer with four cameras has been developed, which may allow to measure surface contours of a measurement object relative to a reference object. Surface contours can be reconstructed three-dimensionally by a novel method using a wavelet transformation and the Bayesian probability theory.

Kurzfassung

In der vorliegenden Arbeit werden Laser-Speckle-Verfahren zur Oberflächenvermessung untersucht, die zum Einsatz in Fusionsreaktoren geeignet sind. In Fusionsreaktoren verursachen Plasma-Wand-Wechselwirkungen Oberflächenstrukturveränderungen, wie beispielsweise Erosionen oder Redepositionen. Die phasenschiebende Speckle-Interferometrie wird genauer untersucht, um Oberflächenstrukturveränderungen feststellen und Erosionstiefen oder Redepositionshöhen bestimmen zu können. Ein neues phasenschiebendes Speckle-Interferometer mit vier Kameras wird entwickelt, welches die Möglichkeit bietet, Oberflächenformen eines Messobjektes relativ zu einem Referenzobjekt vermessen zu können. Die Anwendung der Wavelet-Transformation und der Bayesschen Wahrscheinlichkeitstheorie erlaubt die dreidimensionale Rekonstruktion von Oberflächenformen mit Hilfe eines neuen Verfahrens.

Contents

Introduction

Thermonuclear fusion [1] is one of the most promising future energy resources, but it is far from being applied. Fusion of the hydrogen isotopes deuterium and tritium to helium shall supply energy. Temperatures of over 100 million degrees Kelvin are necessary to ignite the plasma, a low-density ionized gas composed of hydrogen isotopes. Due to these high temperatures the plasma has to be confined in magnetic fields in order to keep it away from any wall material. Since plasma is a complex, many-particle system, various experimental fusion devices have been built to examine the physical laws of plasma behavior, e.g. the ASDEX (Axially Symmetric Divertor Experiment) Upgrade tokamak and the Wendelstein 7-AS stellarator at Max-Planck-Institut für Plasmaphysik (IPP) in Garching, or the Joint European Torus (JET) in Culham [2]. These are large-scale experiments with a major plasma radius of up to 3 m [3]. The planned fusion reactor ITER (International Thermonuclear Experimental Reactor) shall be the first fusion reactor to produce thermal energy at the level of a commercial power plant. The major plasma radius may be about 6 m [4].

The plasma has to be confined in magnetic fields, but this confinement cannot be perfect. Plasma-wall interactions contaminate the plasma and damage the plasma chamber walls. Surface microrelief changes, such as erosion and redeposition, occur [5]. The tokamak research is concentrated on the divertor principle, a special magnetic field configuration [6]. In this region, most of the plasma-wall interactions and surface microrelief changes happen. It is of interest to detect surface microrelief changes and to determine erosion depths or redeposition heights. In order to perform such kind of measurements in-situ, the measurement has to be contactless at distances of up to several meters. Speckle interferometry, an optical laser measurement technique, may enable such measurements.

A very early observation of the interference of light was made by Newton, who observed colored rings, when two smooth surfaces, parallel and close to each other, were illuminated by white light. Much later, Young performed an experiment, in which two parallel slits were illuminated by light, and a

set of parallel interference lines were produced on a screen [7]. Numerous optical configurations employing the interference phenomenon were developed by scientists, e.g. Fabry and Pérot, Fizeau, Mach and Zehnder, or Michelson [8]. Most of these classical interferometers are applied in optical industry to determine the quality of specularly reflecting or smooth transparent objects, e.g. mirrors or lenses. The speckle phenomenon had been investigated by many scientists since the time of Newton who observed the scintillation or twikling for stars [9]. Speckle patterns which are formed by starlight which has propagated through the atmosphere are different in character to those which are formed by diffusely reflected laser light. In the early nineteen sixties, holography was developed, and interferometric measurements of diffusely reflecting or opaque objects became feasible [10]. In 1969, speckle interferometry allowed interferometric measurements of diffusely reflecting objects without the need of recording a hologram [11]. With the development of lasers, CCD cameras, computers and framegrabbers, speckle interferometry has become a powerful measurement technique with many applications [12].

This thesis consists of five chapters. The first chapter describes the basic principles of speckles and interferometry and several speckle measurement techniques, such as surface roughness measurement and phase-shifting methods. Temporal and spatial phase-shifting methods yield three-dimensional information, for instance, on deformation or surface contour of the measurement object. However, this information contains discontinuities due to the sinusoidal characteristics of laser light waves. In chapter 2, a new method to reconstruct a deformation or a surface contour three-dimensionally is explained. A wavelet transformation is used to detect the discontinuities and the Bayesian probability theory to find the optimal solution of a three-dimensional spline. The phase-shifting method of speckle interferometry is analyzed in chapter 3. This method allows to detect surface microrelief changes, e.g. erosion or redeposition, and to determine erosion depths or redeposition heights. Simulation and measurement results are shown. In chapter 4, the new four-camera speckle interferometer set-up, which has been developed to generate four phase-stepped interferograms simultaneously, is presented. This set-up may allow to measure the surface contour of a measurement object compared to the surface contour of a reference object, even if the measurement object is not vibration-isolated. Thus, erosions or redepositions of a few tens of micrometers may be measured, even if the surface contour of the measurement object is complex. Furthermore, limitations of speckle measurement techniques, which are relevant to fusion, are discussed in chapter 5. Finally, conclusions and suggestions for further research are presented.

Chapter 1

Speckle measurement techniques

Interference phenomena in scattered light, such as Fraunhofer's diffraction rings and Quételet's fringes, were of interest in the late nineteenth century. The first recorded laboratory observation of the speckle phenomenon appears to have been that by Exner [13, 14] who studied Fraunhofer's diffraction rings, which are formed when coherent light is diffracted by randomly distributed particles of equal size. He sketched the radially fibrous structure of the light pattern produced by candle light, transmitted through a glass plate on which he had breathed. The superposition of a very large number of waves with random phase led to strong local fluctuations in intensity. The radial nature of the pattern caused by the non-monochromatic light source was replaced by a fine granular structure employing a red filter, creating a light source with lower spectral bandwidth [15]. In 1914 von Laue published a photograph of Fraunhofer's diffraction rings produced by light from a carbon arc lamp illuminating a glass plate covered with lycopodium powder [16]. The photograph shows the radially fibrous structure noted by Exner, and this feature was extensively discussed and reviewed in literature [15, 17].

With the invention of the laser in 1960, highly coherent light became available, and scientists began to study the phenomenon of speckle, and practical applications began to be reported in literature. The surfaces of most materials are optically rough, i.e. the surface height variation is greater than one fourth of the wavelength of illuminating light. When light with a fair degree of spatial and temporal coherence is reflected from an optically rough surface, the light is scattered in all directions. The reflected waves created by different microscopic elements of the surface interfere and produce random fluctuations in intensity with dark and bright spots. This intensity distribution has a characteristic granular structure and is called speckle pattern

[17]. Figure 1.1 shows a typical speckle pattern recorded by a standard CCD

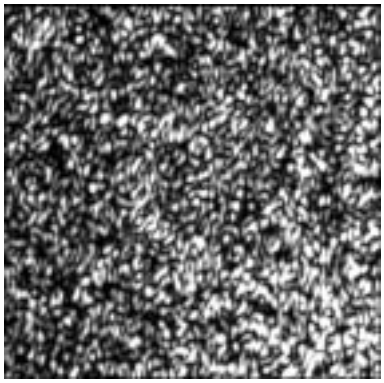

Figure 1.1: Typical speckle pattern.

camera. An aluminum surface has been illuminated by an argon laser with etalon, and the surface was imaged onto the CCD chip. In this case the speckle pattern is of high contrast.

Anyone who has seen a speckle pattern in reality will have observed the curious granular appearance. The speckle pattern moves if the head moves, and it seems impossible to focus the eye properly on the illuminated surface. If the speckle pattern is observed through a small hole, and if this hole is smaller than the pupil, the speckles appear larger. Speckles observed on an imaging system, e.g. with the eye or a camera, are called image speckles or subjective speckles [18]. For speckle patterns collected on a screen, the speckle size depends on the area of the surface that is illuminated. The smaller this area, the larger are the speckles. This type of speckles is called far-field speckles or objective speckles.

The speckle patterns contain information on surface characteristics, e.g. on surface roughness. They are random and can be described in statistical terms. Therefore speckles have the potential to be used for surface roughness measurements.

1.1 Measurement of surface roughness

The surface roughness can be regarded as variation of the surface height. There exists a great variety of distributions of surface height variations and a large number of parameters to characterize the surface roughness that might be considered. Since the speckle is a random phenomenon, only random and isotropic roughness will be considered. Thus the roughness can be characterized in a statistical manner. The most obvious parameter is the average

roughness

$$R_a = \frac{1}{N}\sum_{i=1}^{N}|\Delta r_i|, \tag{1.1}$$

also called the centerline average (CLA) roughness. This is the average of the surface height deviations Δr_i of N data points. This parameter is often used in manufacturing industry. The root-mean-square (rms)

$$\sigma_r = \left(\frac{1}{N}\sum_{i=1}^{N}(\Delta r_i)^2\right)^{1/2} \tag{1.2}$$

is commonly used in the optical industry. Other parameters, e.g. the skewness and the kurtosis, indicate further details of the surface height distribution. The skewness is defined in terms of a mean-cubed roughness and indicates whether the distribution of surface heights is biased towards positive or negative height deviations compared to a Gaussian distribution. The kurtosis is defined in terms of the fourth power of the surface height deviations. A Gaussian distribution has a kurtosis of 3. A higher value indicates a shallower distribution than the Gaussian distribution, and a lower value indicates a steeper distribution.

These parameters describe the properties of the surface height distribution point by point, i.e. the first-order statistics of the surface height distribution. The second-order statistics describe how rapidly the surface height varies from point to point on the surface. Thus the spatial structure of the surface roughness is analyzed. The most important parameters are the autocovariance and the power spectrum. The autocovariance is a measure of how well the surface height at one point can be predicted from the knowledge of the height at a second point. The heights at the two points are highly correlated when the two points are close together, and the correlation decreases when the distance between the two points is increased until there is no correlation between the two surface heights. The correlation length is the distance over which the correlation occurs and is a measure of the average lateral scale of the surface height variations. The power spectrum is given by the Fourier transform of the autocovariance and describes the spatial frequencies of the roughness. Further details of these and other parameters of the surface height distribution can be found in literature [19, 20, 21, 22, 23, 24, 25].

1.1.1 Statistics of speckle patterns

The statistics of speckle patterns were derived in detail by Goodman [26]. Assuming that the laser light is perfectly monochromatic and perfectly polarized, that the surface is rough compared to the wavelength of the laser

light, and that the elementary scattering areas of the surface are unrelated, the following statistical properties can be derived. Since the surface height distribution consists of a very large number of independent random variables, the central limit theorem predicts for the complex amplitudes of the reflected waves a circular Gaussian statistics, while the phase obeys uniform statistics [27]. The probability density function of the intensity I follows a negative exponential law [26]

$$p\left(I\right) = \frac{1}{\langle I \rangle} \exp\left(-\frac{I}{\langle I \rangle}\right). \tag{1.3}$$

The angular brackets indicate the average value over an ensemble of macroscopically similar, but microscopically different rough surfaces. The most probable intensity is zero and causes the very high contrast observed in the speckle patterns. The intensity can become infinite, but in reality it is limited by the total amount of energy reflected by the surface and by the minimum size of a speckle limited by diffraction theory. Another important first-order property of the speckle pattern is the standard deviation of intensity σ_I, which is equal to the mean intensity. The second-order statistics of a speckle pattern describe the spatial structure corresponding to the statistics of the surface roughness. The autocovariance or the autocorrelation can be used as a measure of the average speckle size. The Fourier transform of the autocovariance, the power spectrum, describes the distribution of speckle sizes in the pattern.

In the case of far-field speckles, i.e. free space propagation geometry, the width of the autocorrelation function of the intensity distribution provides a reasonable measure of the average width of a speckle. The average size of a speckle can be taken proportional to [28]

$$l \sim \frac{\lambda z}{q}. \tag{1.4}$$

The speckle size depends on the wavelength of the illumination light λ, the illuminated area of the surface with a diameter q, and the distance z between the surface and the observation plane, which is parallel to the illuminated surface. This explains that the speckle size increases when the illumination area decreases. In [29] the three-dimensional size of the speckles was derived from a circular scattering area. The cross-section of the speckle is an ellipse, and if the observation plane is parallel to the illuminated surface, the cross-section of the speckle becomes a circle. The speckle diameter is then given by equation (1.4), and the speckle length is derived by

$$l_z \sim \frac{\lambda z^2}{q^2}, \tag{1.5}$$

with distance z between the observation plane and the surface, and diameter q of the illuminated area.

In the case of image speckles, i.e. speckles recorded by an imaging system, the speckle diameter

$$l \sim \frac{\lambda z}{2q_{AP}} \tag{1.6}$$

depends on the wavelength λ, the radius q_{AP} of the aperture of the viewing lens, and the distance z between the viewing lens and the image plane parallel to the illuminated surface [30]. This explains why the speckle size increases when the aperture decreases as mentioned before.

1.1.2 Speckle contrast

The speckle patterns discussed above are fully developed, i.e. the surface is rough compared to the wavelength, and the incident light is perfectly coherent, so that the standard deviation σ_I is equal to the mean intensity $\langle I \rangle$, and the speckle contrast

$$C = \frac{\sigma_I}{\langle I \rangle} \tag{1.7}$$

is equal to unity. The reduction of the speckle contrast can be caused, for example, by a reduction of the roughness of the surface, by a reduction of the coherence of the light, or by a superposition of either coherent or incoherent background light to the speckle pattern [26, 31, 32].

If the roughness of the surface is smooth compared to the wavelength of the light, the speckle pattern is partially developed, and the speckle contrast is less than unity. If the roughness of the surface is increased, the speckle contrast is also increased until it approaches unity, as the roughness of the surface approaches one fourth of the wavelength of the light. Thus it is possible to measure the roughness of the surface over the range of the root-mean-square roughness σ_r of about 0.02λ to about 0.25λ. This implies values of σ_r of between about 10 nm and 130 nm when an argon laser (458 nm - 514 nm) is used. To extend the range to larger σ_r values, either a helium-neon laser or infrared wavelengths can be used. The range can also be extended to larger values if the angle of incidence is varied, e.g. if an oblique illumination is used.

If the coherence of the light source is reduced, the speckle contrast depends on the surface roughness, even if the surface roughness is greater than one fourth of the wavelength of the light. Either the spatial or the temporal coherence of the light source may be reduced. A detailed review of the theory of speckles in partially coherent light is given by Parry [33]. The use of partially spatial coherent light has the effect of limiting the range of surface

roughness for which the contrast varies [34, 35]. Thus there is no advantage in using partially spatial coherent light. If the temporal coherence of the light is reduced while the spatial coherence is maintained, the contrast decreases. In order to reduce the temporal coherence, light with a finite bandwidth or a mixture of several discrete laser lines can be used.

The dependence of the speckle contrast on the surface roughness for light with a finite bandwidth can be calculated by means of simplifying assumptions. The light is spatially coherent, the frequency spectrum is of a Gaussian shape with a finite spectral bandwidth, i.e. a root-mean-square spectral deviation σ_b from the central value $2\pi/\lambda$, the surface height distribution is Gaussian, the light is incident normal to the surface, and the far-field speckle pattern is viewed in the specular direction. Thus the speckle contrast is given by [33, 36, 37]

$$C = \frac{1}{\left(1 + (4\sigma_b\sigma_r)^2\right)^{1/4}}, \tag{1.8}$$

where σ_r is the rms surface roughness. The calculation is more complicated for non-specular directions [38]. The range of surface roughness, over which the contrast varies, is increased if the spectral bandwidth is reduced.

The second-order statistics indicate that the speckles become elongated radially from the specular direction, which is not observed under monochromatic illumination. A change of the monochromatic wavelength leads to a change in the phase of the scattered wave, resulting in a shift of each speckle position in the radial direction. Since the speckle pattern produced by polychromatic light is composed of a sum of the speckles produced independently by all monochromatic components of the light, the radially fibrous structure appears in the polychromatic speckle pattern. The radially fibrous structure occurs in the far-field speckle patterns and not in the image speckle patterns [33].

In the speckle patterns created by polychromatic light from a mixture of several discrete laser lines, e.g. six lines of a multifrequency argon laser in the blue and green, also the radially fibrous structure occurs, which depends both on the temporal coherence of the light and on the surface roughness. The theoretical dependence of the speckle contrast on the surface roughness was calculated by Parry [33]. A multifrequency argon laser can be used to measure the surface roughness between about $\sigma_r = 0.5$ μm and 2.0 μm.

Instead of using all lines of a multifrequency laser, it is possible to use just two discrete wavelengths of a multifrequency laser or two different lasers. In the case of dichromatic speckle patterns, the dependence of the contrast

$$C_I = \langle \left(\frac{I_1}{\langle I_1 \rangle} - \frac{I_2}{\langle I_2 \rangle} \right)^2 \rangle^{1/2} \tag{1.9}$$

on the root-mean-square σ_p of the optical path fluctuations and on the spectral difference between the two illuminating wavelengths is given by [39, 40]

$$C_I = 2^{1/2} \left(1 - \exp\left(-\sigma_p^2 \left(k_{\lambda 1} - k_{\lambda 2}\right)^2\right)\right)^{1/2}, \tag{1.10}$$

where k_λ is the wave number with

$$k_\lambda = \frac{2\pi}{\lambda}. \tag{1.11}$$

Both intensities, I_1, generated by λ_1, and I_2, generated by λ_2, have to be recorded simultaneously by two detectors or sequentially by one detector. The root-mean-square of the optical path fluctuation σ_p is proportional to the root-mean-square surface roughness σ_r. The difference of the two speckle intensity distributions increases when the surface roughness increases. The range of the surface roughness over which the contrast C_I varies, depends on the difference $|k_{\lambda 1} - k_{\lambda 2}|$ of the two wave numbers. The range of the surface roughness which can be measured, can be extended if the two wavelengths are chosen to be closer together. However, the precision of the roughness measurement is reduced correspondingly. If an argon laser (497 nm and 502 nm) is used, a surface roughness σ_r up to $\sigma_r = 3.8$ μm can be measured [18, 40].

1.1.3 Correlation techniques

The radially fibrous structure observed in polychromatic speckle patterns in the far field can be analyzed to determine the surface roughness, since this structure will vanish more and more with increasing surface roughness. The spatial autocorrelation function C_s of the speckle intensities in the observation plane describes the radially fibrous structure, also called speckle elongation [41, 42]:

$$C_s\left(\vec{x}_1, \vec{x}_2\right) = \frac{\left\langle I\left(\vec{x}_1\right) I\left(\vec{x}_2\right)\right\rangle - \left\langle I\left(\vec{x}_1\right)\right\rangle \left\langle I\left(\vec{x}_2\right)\right\rangle}{\left(\left\langle I^2\left(\vec{x}_1\right)\right\rangle - \left\langle I\left(\vec{x}_1\right)\right\rangle^2\right)^{1/2} \left(\left\langle I^2\left(\vec{x}_2\right)\right\rangle - \left\langle I\left(\vec{x}_2\right)\right\rangle^2\right)^{1/2}}, \tag{1.12}$$

with location vectors $\vec{x}_i = (x_i, y_i)$, $i \in \{1, 2\}$. The angular brackets denote the averages over the pixels of the regions with respective centers $\vec{x}_i$ of the speckle image. For a smooth surface the intensity distributions of the differing wavelengths resemble each other. The angular dispersion leads to a radial broadening of the superposed intensities of all used wavelengths for larger distances from the optical axis. With increasing surface roughness, the decorrelation of the monochromatic speckle patterns is intensified, and

the speckle elongation of the total intensity pattern will gradually decrease. The two dimensions l_x and l_y of the speckles in the x- and y-direction of the observation plane can be determined by the widths of the spatial autocorrelation function in the x- and y-direction [41]. The information processing of the mean autocorrelation widths and the standard deviations of the autocorrelation widths allow surface roughness measurements from only one speckle pattern in the range of $\sigma_r = 0.05$ μm to 5 μm, using an argon laser [41]. The measuring range can be extended to up to 10 μm using other wavelengths [43].

The radially fibrous structure observed in polychromatic speckle patterns is difficult to analyze. Another technique is to measure the correlation between two speckle patterns produced by illuminating the surface with coherent light of either two differing wavelengths or of two differing angles of incidence. Ruffing derived theoretical solutions for both far-field and image plane geometry and also for partially and fully developed speckle patterns [44, 45].

The correlation coefficient C_{12} of the speckle intensities I_1 and I_2 of two different speckle patterns is defined by

$$C_{12} = \frac{\langle I_1 I_2 \rangle - \langle I_1 \rangle \langle I_2 \rangle}{\left(\langle I_1^2 \rangle - \langle I_1 \rangle^2\right)^{1/2} \left(\langle I_2^2 \rangle - \langle I_2 \rangle^2\right)^{1/2}}, \tag{1.13}$$

where the angular brackets denote the ensemble average. Assuming perfectly monochromatic and perfectly polarized light, fully developed speckle patterns, a plane, perfectly conducting and isotropically rough surface, and a circular Gaussian statistics of the complex field amplitude of the scattered light, the dependence of the correlation coefficient on the surface roughness can be derived for both the spectral speckle correlation (SSC) and the angular speckle correlation (ASC). The formulas of the correlation coefficients consist of a roughness-dependent and a space-dependent term. The space-dependent term can be eliminated by optimally chosen spatial measuring conditions.

For the far-field geometry, the object plane of the surface is in the front focal plane, and the observation plane is in the back focal plane of a collimating lens. Thus the observation plane is the Fourier plane, and the far field is the Fourier transform of the object field.

The correlation coefficient for the SSC in the far field is given by

$$C_{12}^S = \exp\left(-\left(2\sigma_r \left(k_{\lambda 1} - k_{\lambda 2}\right) \cos\alpha\right)^2\right), \tag{1.14}$$

if the illumination and the observation are performed symmetrically to the direction of the surface normal at angle α, and the detection of the speckle

pattern is performed on the optical axis [44]. The range of the surface roughness which can be measured, can be varied by choosing suitable pairs of wavelengths.

The correlation coefficient for the ASC in the far field is derived by

$$C_{12}^{A} = \exp\left(-\left(2\sigma_r k_\lambda \Delta\alpha \sin\alpha\right)^2\right), \tag{1.15}$$

if the angle of incidence is changed by $\Delta\alpha$ between the capture of the two speckle images instead of using two differing wavelengths. This leads to a shift of the speckle pattern depending on the focus length x_f of the collimating lens, the illumination and observation angle α, and the change of the angle $\Delta\alpha$. The shift must be compensated, e.g. by shifting one speckle pattern, or by searching the maximum of the correlation coefficient for different shifts between the two speckle patterns. The range of the measurable surface roughness can be varied by choosing the angle variation $\Delta\alpha$.

The image plane geometry is shown in Fig. 1.2 and consists of a twofold

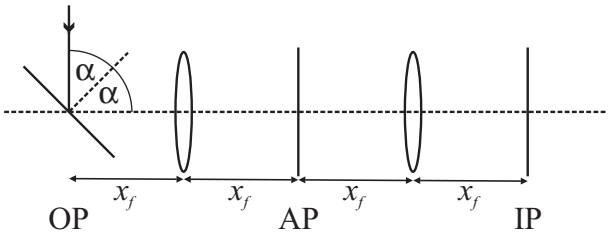

Figure 1.2: Image plane geometry. AP: aperture plane, IP: image plane, OP: object plane.

Fourier transform set-up and an aperture in the aperture plane that realizes a spatial filtering. It is assumed that a Gaussian aperture is positioned on the optical axis in the aperture plane and that the illumination and the observation is performed symmetrically as shown in Fig. 1.2. The correlation coefficient for the SSC is given by equation (1.14) [45]. It is the same result as obtained for the SSC in the far-field geometry.

The same result as in equation (1.15) can be derived for the ASC in the image-plane geometry, if two different positions for the aperture in the aperture plane are chosen for recording the two speckle patterns. The ASC method in the image-plane geometry is difficult to realize because of the geometrical arrangement of the two apertures.

The correlation coefficient of partially developed speckle patterns, i.e. in the case of a smooth surface compared to the wavelengths of light, depends on the number of the independent scattering areas of the surface. Thus

the measurement of the surface roughness is only possible with an a priori knowledge of the number of independent scattering areas of the surface [46].

The range of the surface roughness, which can be measured with the ASC and the SSC method, is at least the range of about 0.3 μm up to 10 μm, if visible light is used. Smaller surface roughness can be determined, but in the case of partially developed speckle patterns an a priori knowledge has to be considered. The upper bound can be extended and surface roughness measurements of up to 32 μm are reported in [44].

1.1.4 Discussion

The theory applied for different roughness measurement techniques is far from being complete. A major difficulty arises when the surface is modeled mathematically. Often, a Gaussian surface height distribution is assumed, but the results depend more or less on the form of the surface height distribution function. Since the contrast of a partially developed speckle pattern is strongly dependent on the surface height distribution, the roughness measurement by speckle contrast is in this case less attractive [47]. In [44] cylindrical surfaces instead of plane surfaces, and surfaces with non-isotropic surface roughness, e.g. different machined surfaces, were considered for the SSC and the ASC. The theory becomes more complex, and for a more complex surface profile the analytical determination of the surface roughness will be difficult or impossible. However, if comparative measurements, rather than absolute measurements, are to be made on surfaces with similar statistics, the described surface roughness measurement techniques will work well.

For the evaluation of experimental data, the law of large numbers [48] is applied to replace the average over an ensemble of rough surfaces by the average of a sufficient number of independent intensity values from one surface, which can be determined experimentally. These intensity values can be obtained when the surface is moved and different illuminated surface areas are recorded. For many applications, the ensemble average can be replaced by the spatial average over the speckle pattern [18, 44]. Thus, real-time measurements are achievable.

Practical intensity measurements must be made through finite detector apertures and are always a smoothened or integrated version of the ideal point-intensity. Thus, the statistics of the measured speckle pattern will be different from the ideal statistics [26]. However, for comparative rather than absolute measurements, using the same detector, this effect of smoothing or integrating does not need to be considered when the detector size is much smaller than the speckle size.

The simulation of different speckle measurement techniques [49, 50, 51],

e.g. contrast measurement, ASC or SSC, allows, for instance, to consider different surface height distributions and a more complex illumination and observation geometry. Hence, simulation results can be obtained which cannot be derived analytically, thereby improving the theoretical knowledge.

1.2 Interferometry

Classical interferometry refers to experiments involving the interference of two coherent waves which are reflected at mirrors in an interferometer. The field amplitude of a light wave is commonly described by the complex quantity [7]

$$\vec{E}\left(x,t\right) = \vec{e}E_0 \exp\left(-j\left(\vec{k}_\lambda \vec{x} - \omega t - \Phi\right)\right), \tag{1.16}$$

where E_0 is the amplitude, $\vec{e}$ is the unit vector of the electric field, $\vec{k}_\lambda$ the wave vector, ω the angular frequency, t the time, Φ the spatial phase, and $\vec{x} = (x, y, z)$. The intensity is a measure of the energy flowing through an area in a given time interval, and is derived by time averaging of the modulus of the Poynting vector. For a linear, homogeneous, and isotropic dielectric medium, the intensity is given by

$$\begin{aligned} I\left(\vec{x},t\right) &= \frac{c\epsilon}{2}\left|\Re e\left(\vec{E}\left(\vec{x},t\right)\vec{E}^*\left(\vec{x},t\right)\right)\right| \\ &= \frac{c\epsilon}{2}E_0^2, \end{aligned} \tag{1.17}$$

where c is the velocity of the light, $\vec{x}$ the spatial coordinate, ϵ the permittivity, $\Re e$ the real part of the complex quantity, and * the complex conjugate.

The light waves are subject to the superposition principle. This means that, if two waves

$$\vec{E}_1\left(\vec{x},t\right) = \vec{e}_1 E_{01} \exp\left(-j\left(\vec{k}_{1\lambda}\vec{x} - \omega t - \Phi_1\right)\right), \tag{1.18}$$

$$\vec{E}_2\left(\vec{x},t\right) = \vec{e}_2 E_{02} \exp\left(-j\left(\vec{k}_{2\lambda}\vec{x} - \omega t - \Phi_2\right)\right), \tag{1.19}$$

with

$$\vec{k}_{i\lambda} = \frac{2\pi}{\lambda_j}\vec{e}_{i\lambda} \tag{1.20}$$

and $i, j \in \{1, 2\}$, are superposed, the resulting field $\vec{E}_g$ simply becomes the sum, i.e.

$$\vec{E}_g = \vec{E}_1 + \vec{E}_2, \tag{1.21}$$

and the intensity

$$\begin{aligned} I_g &= \frac{c\epsilon}{2}\left|\Re e\left(\vec{E}_g\vec{E}_g^*\right)\right| \\ &= \frac{c\epsilon}{2}\Big[E_{01}^2 + E_{02}^2 + 2E_{01}E_{02}\cos\left(\Phi_1 - \Phi_2\right) \\ &\quad \cdot\cos\Big(\left(\vec{k}_{1\lambda} - \vec{k}_{2\lambda}\right)\vec{x}\Big)\vec{e}_1\cdot\vec{e}_2\Big]. \end{aligned} \tag{1.22}$$

In the absence of the spatial phases Φ_1 and Φ_2, equal wavelengths with $\lambda = \lambda_1 = \lambda_2$, $\vec{e}_1$ parallel to $\vec{e}_2$ (the other cases will be discussed later), and, for the sake of simplicity, the axis chosen such that the propagation vectors $\vec{k}_{1\lambda}$ and $\vec{k}_{2\lambda}$ lie in the xy-plane and have equal but opposite angels α_k with the y-axis, i.e. α_k and $-\alpha_k$. Thus,

$$\left(\vec{k}_{1\lambda} - \vec{k}_{2\lambda}\right)\vec{x} = \frac{4\pi}{\lambda}x\sin\alpha_k, \tag{1.23}$$

and the intensity is given by

$$\begin{aligned} I_g &= \frac{c\epsilon}{2}\left(E_{01}^2 + E_{02}^2 + 2E_{01}E_{02}\cos\left(\frac{4\pi}{\lambda}x\sin\alpha_k\right)\right) \\ &= I_1 + I_2 + 2\left(I_1I_2\right)^{1/2}\cos\left(\frac{4\pi}{\lambda}x\sin\alpha_k\right), \end{aligned} \tag{1.24}$$

where I_1 and I_2 are the intensities of the two superimposing waves. The intensity varies along any line parallel to the x-axis and is known as interference fringe pattern. The intensity varies sinusoidally between the minimum value $I_1 + I_2 - 2\left(I_1I_2\right)^{1/2}$ and the maximum value $I_1 + I_2 + 2\left(I_1I_2\right)^{1/2}$.

1.2.1 Conventional interferometers

In order to obtain the interference fringe pattern, the waves must be coherent to each other. In practical terms this means that both waves must be generated by the same light source. The best-known interferometer which divides the amplitude of the waves, is the Michelson interferometer shown in Fig. 1.3. The amplitude of the incident light is divided by the beam splitter BS. The reflected and the transmitted waves propagate to the mirrors M1 and M2, respectively, where they are reflected back and recombine to form the interference pattern in the observation plane on the detector. The intensity is given by equation (1.22). If one of the mirrors, say M2, is not perfectly flat, it will distort the incident wavefront as well as the interference fringe pattern. If both waves propagate in the same direction, i.e. $\vec{k}_{1\lambda} = \vec{k}_{2\lambda}$, the intensity is given by the well-known formula

$$I_g = I_1 + I_2 + 2\left(I_1I_2\right)^{1/2}\cos\Delta\Phi \tag{1.25}$$

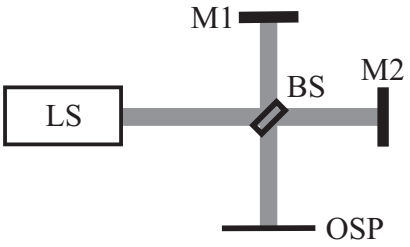

Figure 1.3: Michelson interferometer. BS: beam splitter, LS: Light source (laser), M1, M2: mirrors, OSP: observation plane.

with phase difference $\Delta\Phi = \Phi_1 - \Phi_2$. The phase difference depends on the path difference between the two optical paths of the interferometer, the lengths x_1 between beam splitter and mirror M1, and the length x_2 between beam splitter and mirror M2. If the deviation from the flatness of the mirror M2 is equal to Δx_2, the phase difference is given by

$$\Delta\Phi = (x_1 - (x_2 + \Delta x_2))\,\frac{4\pi}{\lambda}. \tag{1.26}$$

The maxima of the interference fringe pattern will occur when

$$\Delta\Phi = 2\pi n, \tag{1.27}$$

with $n \in \mathcal{Z}$. Hence, the path difference between equivalent points in the intensity variation, including the maxima, is a multiple of λ. Thus the interference fringe pattern maps the variation of the height of mirror M2 compared to mirror M1 as contours of the interval of $\lambda/2$. This demonstrates the ability of interferometry to map height variations with a sensitivity of the order of the wavelength of light.

The fringe contrast C_f, sometimes denoted as the visibility, is given by

$$C_f = \frac{I_{max} - I_{min}}{I_{max} + I_{min}}, \tag{1.28}$$

where I_{max} and I_{min} are the maximum and the minimum of a region of the interference fringe pattern. It has its maximum when the intensity I_1 is equal to I_2. The fringe contrast is reduced when the vectors of polarization are not parallel to each other, i.e. when the angle α_e between $\vec{e}_1$ and $\vec{e}_2$ is different from $0°$. The dependence of the interference fringe pattern on α_e is given by

$$I_g = I_1 + I_2 + 2\,(I_1 I_2)^{1/2} \cos(\Delta\Phi) \cos\alpha_e \tag{1.29}$$

from equations (1.22) and (1.25). The spatial position of the interference fringes, the minima and the maxima, does not change, only the fringe contrast is reduced.

Another commonly used interferometer is the Mach-Zehnder interferometer shown in Fig. 1.4, which is employed for measuring changes in density

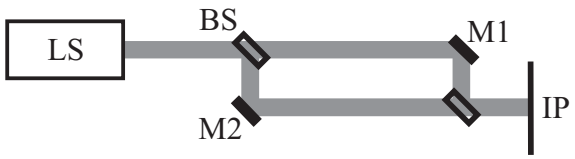

Figure 1.4: Mach-Zehnder interferometer. BS: beam splitter, IP: image plane, LS: laser, M1, M2: mirrors.

occurring as result of pressure or temperature changes of transparent objects, since such changes produce changes in the refractive index. The phase change $\Delta\Phi$ is derived by

$$\Delta\Phi = \frac{2\pi}{\lambda} x \Delta n, \tag{1.30}$$

when the change of the refractive index Δn is constant over the distance x. The advantage of this type of interferometer is that the light is divided into two separated beams and passes only once through the reference and the object path.

1.2.2 Out-of-plane displacement-sensitive interferometer

Probably the simplest concept of a speckle interferometer, proposed by Leendertz [11], which combines two speckle fields, is based on the Michelson interferometer, in which both mirrors are replaced by rough surfaces. The set-up is shown in Fig. 1.5. Both surfaces are imaged in the image plane and the

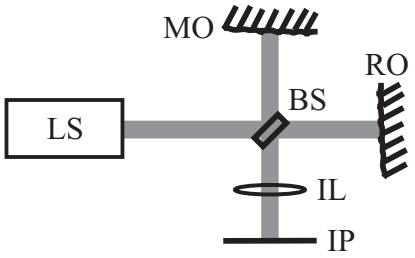

Figure 1.5: Michelson interferometer set-up with rough surfaces. BS: beam splitter, LS: laser, M1, M2: mirrors, MO: measurement object, RO: reference object.

images are recorded, for instance, by a CCD camera. The coherent addition

of the two speckle fields, reflected from the two rough surfaces, will result in a third field, similar in brightness distribution statistics, but different in detail. The intensity at a given elementary area of the image plane, corresponding in size to one speckle, is given by [52, 53] (b: before)

$$I_b = I_1 + I_2 + 2\left(I_1 I_2\right)^{1/2} \cos \Phi, \tag{1.31}$$

where Φ is the phase difference between the two waves. If the reference object is moved a distance x_d parallel to the surface normal, the resulting phase change is given by

$$\Delta\Phi = \frac{4\pi}{\lambda} x_d. \tag{1.32}$$

After the displacement, the intensity at this elementary area will be changed to (a: after)

$$I_a = I_1 + I_2 + 2\left(I_1 I_2\right)^{1/2} \cos\left(\Phi + \Delta\Phi\right). \tag{1.33}$$

This means that the correlation between the two speckle patterns before and after the movement has changed. The correlation coefficient, equation (1.13), of the intensities I_1 and I_2 is derived by [30]

$$C_{12}\left(\Delta\Phi\right) = \frac{1 + R_I^2 + 2R_I \cos \Delta\Phi}{\left(1 + R_I\right)^2}, \tag{1.34}$$

assuming that I_1, I_2, and Φ are independent variables,

$$\langle \cos \Phi \rangle = \langle \cos\left(\Phi + \Delta\Phi\right) \rangle = 0, \tag{1.35}$$

$$\left\langle I^2 \right\rangle = 2\left\langle I \right\rangle^2, \tag{1.36}$$

for $I = I_1$ and for $I = I_2$,

$$\left\langle I_1 \right\rangle = R_I \left\langle I_2 \right\rangle, \tag{1.37}$$

and that I_1, I_2, and Φ remain unchanged when the change giving rise to $\Delta\Phi$ is introduced. When

$$\Delta\Phi = \left(2n + 1\right)\pi, \tag{1.38}$$

with $n \in \mathcal{Z}$, the correlation coefficient between I_1 and I_2 will have the minimum value of

$$C_{12} = \left(\frac{1 - R_I}{1 + R_I}\right)^2, \tag{1.39}$$

but when $\Delta\Phi$ takes the value $2n\pi$, the correlation coefficient will have the maximum value of unity. If it is possible to detect the positions with the

minimum and the maximum values of the correlation coefficient, the change in phase, i.e. the displacement of the reference surface, can be measured.

If the geometry of this interferometer is changed, and either or both the illumination and the observation direction are no longer parallel to the surface normal, the phase change $\Delta\Phi$ is derived by

$$\Delta\Phi = \frac{2\pi}{\lambda}\left(\vec{k}_{il} - \vec{k}_o\right)\vec{x}_d, \tag{1.40}$$

where $\vec{k}_{il}$ is the illumination direction, $\vec{k}_o$ is the observation direction, and $\vec{x}_d$ is the surface displacement. In that case, the phase change depends both on the in-plane and the out-of-plane displacement.

Another speckle interferometer set-up with a smooth reference beam is based on the Mach-Zehnder interferometer and is shown in Fig. 1.6. The

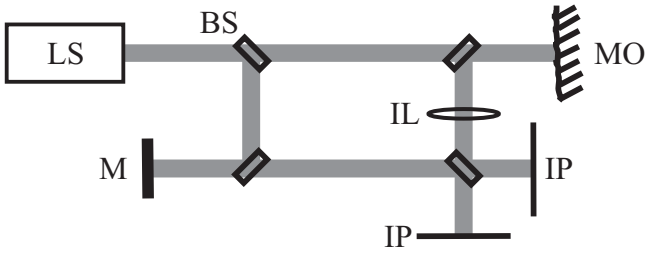

Figure 1.6: Smooth reference interferometer. BS: beam splitter, IL: image lens, IP: image plane, LS: laser, M: mirror, MO: measurement object.

illumination direction of both the reference mirror and the object surface is parallel to the surface normal. The object surface is imaged in the image planes by the image lens. This interferometer set-up can be applied in the same way for the measurement of changes of the object surface as the Michelson interferometer set-up with rough surfaces. The same equations are valid.

If the reference mirror is replaced by a rough surface and a second image lens is employed, the Mach-Zehnder interferometer set-up with two rough surfaces, as shown in Fig. 1.7, is obtained. Both the reference and the object surface are imaged by an image lens in the image planes, and two speckle fields are superposed. The equations described before are valid, and the applications are discussed later.

1.2.3 Shearing interferometer

Shearing interferometers compare the phase of a wavefront with that of the same wavefront displaced laterally by a small distance. There are numer-

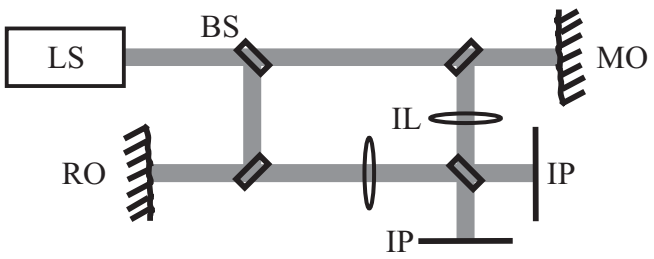

Figure 1.7: Mach-Zehnder interferometer set-up with rough surfaces. BS: beam splitter, IL: image lens, IP: image plane, LS: laser, MO: measurement object, RO: reference object.

ous ways to construct a speckle shearing interferometer [54, 55]. One of the simplest set-ups, applied by Leendertz [54], uses a Michelson interferometer set-up, as shown in Fig. 1.8, to provide the shearing of the wavefront. The

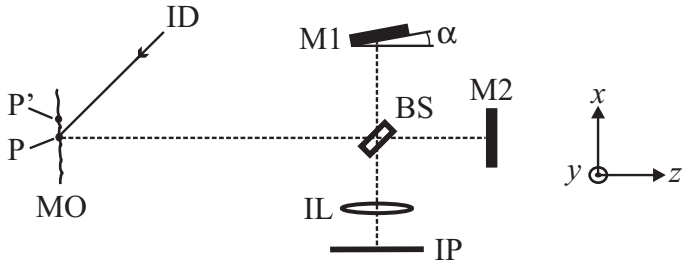

Figure 1.8: Shearing interferometer. BS: beam splitter, ID: illumination direction, IL: image lens, IP: image plane, M2: mirror, MO: measurement object.

measurement object is imaged by the image lens through an optical arrangement consisting of a beam splitter and two orthogonal plane mirrors. The intensity at a point in the image plane corresponds to the superposition of the light scattered from two adjacent points of the measurement object, e.g. the points P and P'. The distance between the two points is the lateral shear x_s in the object plane. The lateral shear between the two images may be varied by tilting one of the mirrors by a small angle α. If the measurement object is displaced by $\vec{x}_d$ and $\vec{x}'_d$ at the points P and P', the phase change $\Delta\Phi$ is derived by

$$\Delta\Phi = \frac{2\pi}{\lambda}\left(\vec{k}_{il} - \vec{k}_o\right)\left(\vec{x}_d - \vec{x}'_d\right). \tag{1.41}$$

When the shear is small compared to the displacement, the phase change is indicative of the derivative of the displacement in the direction of the shear.

When the illumination direction $\vec{k}_{il}$ and the observation direction $\vec{k}_o$ are normal, the phase change

$$\Delta\Phi = \frac{4\pi}{\lambda}\,(x_d - x'_d) \tag{1.42}$$

depends mostly on the first derivative of the displacement, the deformation in the direction of the shear, i.e. the x-direction [30]. The dependence on the derivative in the y-direction can similarly be obtained by shearing in the y-direction.

The phase change indicates abrupt changes in the surface displacement, the deformation only in the direction of the shear. However, this interferometer set-up has advantages. The optical set-up is very simple, thus relaxing the vibration isolation requirement. The coherence length requirement of the laser source is greatly reduced because the difference between the measurement path and the reference path is very small and independent of the distance to the measurement object.

1.2.4 In-plane displacement-sensitive interferometer

The set-up shown in Fig. 1.9, proposed by Leendertz [11], enables the mea-

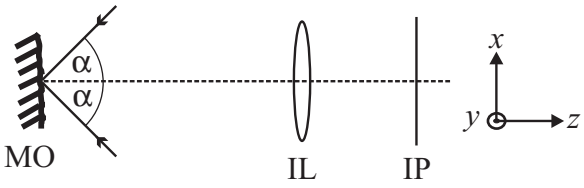

Figure 1.9: In-plane displacement-sensitive interferometer. IL: image lens, IP: image plane, MO: measurement object.

surement of the displacement component lying in the plane of the measurement object. In order to simplify the interpretation of the measured phase change dependent on the displacement, the two coherent illumination beams should preferably be plane, incident at equal angles α on either side of the surface normal, and the surface should be imaged by the imaging lens in the image plane. Each illuminating beam generates its own speckle pattern, which superimposes coherently with the speckle pattern generated by the complementary scattered beam in the image plane. If the surface is displaced in the out-of-plane direction, i.e. the z-direction, equal path length changes are introduced for both beams. Thus the resulting speckle pattern in the image plane will remain unchanged. This set-up is independent of any

displacement in the out-of-plane direction. Displacements in the y-direction do not produce any change in the path length. If the surface is displaced by a small distance x_d in the x-direction (in-plane), the path length of one beam will be increased by $x_d \sin\alpha$, while the path length of the other beam will be decreased by the same amount, and the total path difference of $2x_d \sin\alpha$ will result. The phase change is given by

$$\Delta\Phi = \frac{4\pi}{\lambda} x_d \sin\alpha. \tag{1.43}$$

This set-up allows to measure the in-plane displacements independently of out-of-plane displacements. Alternative methods are reported in literature [56, 57], including the measurement of the x- and y-component of the displacement simultaneously.

1.2.5 Fringe formation

The speckle patterns may be digitized by a frame grabber [58] if, for instance, a CCD camera is located in the image plane of the speckle interferometer. This kind of interferometry is known as video speckle interferometry or electronic speckle pattern interferometry (ESPI). Interference fringe patterns occur after processing two appropriate speckle patterns, e.g. after adding or subtracting. When the intensities of two speckle patterns are given by

$$I_{gb} = I_1 + I_2 + 2\left(I_1 I_2\right)^{1/2} \cos\Phi, \tag{1.44}$$

before, and

$$I_{ga} = I_1 + I_2 + 2\left(I_1 I_2\right)^{1/2} \cos\left(\Phi + \Delta\Phi\right), \tag{1.45}$$

after the phase change $\Delta\Phi$, the addition of these intensities results in

$$I_{g+} = 2I_1 + 2I_2 + 4\left(I_1 I_2\right)^{1/2} \cos\left(\Phi + \frac{\Delta\Phi}{2}\right) \cos\left(\frac{\Delta\Phi}{2}\right). \tag{1.46}$$

The areas of maximum correlation of the two speckle patterns have maximum fringe contrast, but the minimum value of the fringe contrast is non-zero where the two speckle patterns are uncorrelated.

The result of subtracting the two intensities given by

$$I_g = 4\left(I_1 I_2\right)^{1/2} \sin\left(\Phi + \frac{\Delta\Phi}{2}\right) \sin\left(\frac{\Delta\Phi}{2}\right), \tag{1.47}$$

has negative and positive values. Since a monitor requires positive values, the absolute value

$$I_{g-} = |I_g| \tag{1.48}$$

is used. The fringe maxima obtained by adding, correspond to the fringe minima obtained by subtracting the intensities. The fringe minima have the intensity value of zero, while the addition fringe minima do not. Hence, the subtraction fringes have a better fringe contrast than do addition fringes.

1.2.6 Shape measurement

Several interferometric methods for surface shape measurement, also known as contouring techniques, have been developed [30, 59, 60, 61, 62, 63]. Most of these methods are based on the use of either two differing wavelengths or two differing illumination directions. In ESPI the shape of the optically rough measurement object is compared with a master optical wavefront or a reference object. A flat, spherical or cylindrical master wavefront may be generated by conventional optical components. More complex master wavefronts can be reconstructed from a hologram [64].

Employing the two-wavelength method, the interferometer set-ups shown in Figs. (1.5), (1.6), and (1.7), can be applied to measure the difference in depth between the master wavefront and the measurement object parallel to the viewing direction. Assuming that the reflectivity coefficient of the surfaces does not change for a small change of the wavelength, and that the intensities I_1 and I_2 remain constant, the intensities I_{g1} and I_{g2} for the wavelengths λ_1 and λ_2, respectively, are given by

$$I_{g1} = I_1 + I_2 + 2\left(I_1 I_2\right)^{1/2} \cos\left(\Phi_1 + \frac{4\pi}{\lambda_1} x_d \cos\alpha\right), \tag{1.49}$$

and

$$I_{g2} = I_1 + I_2 + 2\left(I_1 I_2\right)^{1/2} \cos\left(\Phi_2 + \frac{4\pi}{\lambda_2} x_d \cos\alpha\right), \tag{1.50}$$

where α is the angle of incidence and x_d the normal separation between the measurement surface and the master surface. The subtraction of I_{g1} and I_{g2} yields

$$\begin{aligned} I_{g-} &= |I_{g1} - I_{g2}| \\ &= \Big|4\left(I_1 I_2\right)^{1/2} \sin\left(\frac{\Phi_1 + \Phi_2}{2} + 2\pi x_d \left(\frac{1}{\lambda_1} + \frac{1}{\lambda_2}\right)\cos\alpha\right) \\ &\quad \cdot \sin\left(\frac{\Phi_1 - \Phi_2}{2} + 2\pi x_d \left(\frac{1}{\lambda_1} - \frac{1}{\lambda_2}\right)\cos\alpha\right)\Big|. \end{aligned} \tag{1.51}$$

Since

$$\frac{1}{\lambda_1} + \frac{1}{\lambda_2} >> \frac{1}{\lambda_1} - \frac{1}{\lambda_2}, \tag{1.52}$$

and because of the low spatial resolution of a CCD camera, only the second sinus term is detected. Thus,

$$I_{g-} \sim \left|\sin\left(\frac{\Phi_1 - \Phi_2}{2} + \frac{\pi}{\Lambda} x_d\right)\right|, \tag{1.53}$$

with the synthetic wavelength

$$\Lambda = \frac{\lambda_1 \lambda_2}{2|\lambda_2 - \lambda_1| \cos\alpha}, \tag{1.54}$$

produces fringes occurring at intervals of $x_d = \Lambda$. Hence, the surface shape of the measurement object compared to that of the master surface (or the master surface introduced by the master wavefront), i.e. the normal distance between the measured and the master surface, is mapped out at intervals of Λ. The fringe sensitivity may be varied by changing the difference between the two wavelengths. When a multifrequency argon laser is used, the synthetic wavelength is in the range of 2 μm to 24 μm. The range can be extended up to tens of millimeters when the two wavelengths are very close together, e.g. when using an optical parametrical oscillator.

The rate at which a speckle pattern decorrelates due to the wavelength change depends on the surface roughness as well as on the change of the wavelength. If the wavelength difference is such that

$$\Lambda > 8\sigma_r, \tag{1.55}$$

good fringe contrast will be obtained [65, 66]. This implies values of the rms surface roughness σ_r of 3 μm for the largest synthetic wavelength $\Lambda = 24$ μm, achievable if an argon laser is employed.

The use of two differing angles of incidence, also known as two-source method, leads to the synthetic wavelength

$$\Lambda = \frac{\lambda}{\cos\alpha_1 - \cos\alpha_2}, \tag{1.56}$$

depending on the difference between the two angles.

1.2.7 Limitations

Intensity measurements are an integrated version of the ideal point intensity and can be expressed in the form

$$I_G = \frac{1}{G} \iint\limits_G w(x,y)\, I(x,y)\, dx\, dy, \tag{1.57}$$

with the detector area G, the point intensity $I(x, y)$ at the coordinate position (x, y), and the weighting function $w(x, y)$ describing the detector response at different coordinates. If the speckle size is larger than the detector size, the speckles are fully resolved. Otherwise several speckles are integrated over the detector area.

For fringe patterns gained by adding two speckle patterns, the speckles should be fully resolved, and the noise in the smooth reference beam should be minimized to optimize the fringe contrast. For interferometers with a speckled reference beam, the fringe contrast is very poor. Therefore such interferometers are not practical [67].

For fringe patterns gained by subtracting two speckle patterns, the ratio between the mean intensity $\langle I_2 \rangle$ of the smooth reference beam and mean intensity of the speckled beam $\langle I_1 \rangle$ should ideally be 2. But a value of up to 20 still gives reasonable fringe contrast. The maximum fringe contrast for interferometers with a speckled reference beam is obtained when the mean intensities of the two beams at the image plane are equal [67]. The speckles need not to be fully resolved in order to obtain an acceptable fringe contrast [68, 69, 70, 71]. Thus, larger apertures can be applied in the case of limited laser power.

The spatial resolution and the dynamic range of CCD cameras are considerably smaller than those of photographic and holographic emulsions. When the fringe spacing becomes comparable to the speckle size, the fringe contrast decreases and goes to zero when they become equal. Thus, the fringe spacing should be larger than twice the speckle size as well as larger than twice the pixel size.

The object size observed is limited by the available laser power, the camera sensitivity and the imaging system. The geometry of the imaging system is shown in Fig. 1.10. The illuminated area G_{MO}, a circle with radius q_{MO},

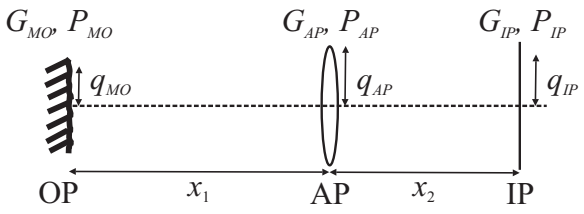

Figure 1.10: Imaging set-up. AP: aperture plane, IP: image plane, OP: object plane.

is imaged by the image lens in the image plane with the area G_{IP}, a circle with radius q_{IP}. Assuming a circular aperture with a radius q_{AP}, the power

of the reflected laser light in the aperture plane

$$P_{AP} = \rho \frac{G_{AP}}{x_1^2} P_{MO} \tag{1.58}$$

depends on the power of the illuminating laser light P_{MO}, the distance x_1 between object and aperture plane, the area of the aperture G_{AP}, and the scattering coefficient ρ. Without any losses, the power in the image plane P_{IP} is equal to the power in the aperture plane P_{AP}. Since the object is imaged in the image plane, q_{IP} is related to q_{MO} by

$$q_{IP} = \frac{x_2}{x_1} q_{MO}. \tag{1.59}$$

Hence,

$$x_1^2 G_{IP} = x_2^2 G_{MO}. \tag{1.60}$$

If the spatial distribution of the laser power is a uniform over the cross-section of the laser beam or a circular Gaussian distribution symmetrical to the optical axis, the intensity in the image plane is given by

$$\begin{aligned} I_{IP} = \frac{P_{IP}}{G_{IP}} &= \rho P_{MO} G_{AP} \frac{1}{G_{IP} x_1^2} \\ &= \rho P_{MO} G_{AP} \frac{1}{G_{MO} x_2^2}. \end{aligned} \tag{1.61}$$

The intensity in the image plane is inversely proportional to x_1^2, and related to x_2^2 by the imaging system. Consideration of diffraction in the aperture plane results in the same dependence

$$I_{IP} \sim \frac{1}{x_1^2}. \tag{1.62}$$

Rayleigh proposed that two components of equal intensity should be considered to be just resolved when

$$\Delta y = 1.22 \frac{\lambda x_2}{2 q_{AP}}, \tag{1.63}$$

where Δy is the distance between two points in the image plane which are related to two points on the measurement surface which can be just resolved. This quantity is a measure of the spatial resolution and is proportional to the speckle size given by equation (1.6).

1.3 Temporal phase-shifting methods

The sign of the phase difference $\Delta\Phi$ is unknown when fringe patterns are obtained by adding or subtracting intensities. The interference formula for the Michelson interferometer, equation (1.25),

$$I_g = I_1 + I_2 + 2\left(I_1 I_2\right)^{1/2} \cos\Delta\Phi,$$

contains the three unknown variables I_1, I_2, and $\Delta\Phi$. If I_1 and I_2 are known, e.g. the separately measured intensities of the two beams, $\Delta\Phi$ modulo π can be derived. Assuming that the phases $\Delta\Phi_1$ and $\Delta\Phi_2$ of two adjacent measuring points, e.g. between two adjacent pixels of a CCD camera, are given by

$$\Delta\Phi_1 = \Delta\Phi_{01} + n\pi \tag{1.64}$$

and

$$\Delta\Phi_2 = \Delta\Phi_{02} + m\pi, \tag{1.65}$$

with

$$\Delta\Phi_{01}, \Delta\Phi_{02} \in \left[-\frac{\pi}{2}, \frac{\pi}{2}\right[, \tag{1.66}$$

the phases modulo π can be calculated, i.e. $\Delta\Phi_{01}$ and $\Delta\Phi_{02}$. In the absence of perturbations, the result can be determined clearly when

$$|\Delta\Phi_2 - \Delta\Phi_1| < \pi. \tag{1.67}$$

This requirement may be fulfilled for mirrors, but not for optically rough surfaces. A practical set-up that employs this method is given in [72].

The intensity of a detector pixel may be expressed as [73]

$$I = I_0\left(1 + \gamma\cos\Delta\Phi\right), \tag{1.68}$$

where the three unknown variables are the background intensity I_0, the visibility or modulation γ, and the phase difference $\Delta\Phi$. If one of the two mirrors in the Michelson interferometer is moved a distance x_d parallel to the surface normal, and when this direction is the viewing and illumination direction, the additional phase change

$$\beta = \frac{4\pi}{\lambda} x_d \tag{1.69}$$

is introduced, and equation (1.68) yields

$$I_g = I_0\left(1 + \gamma\cos\left(\Delta\Phi + \beta\right)\right). \tag{1.70}$$

The temporal variation of the relative phase shift β between the measurement beam and the reference beam is known as temporal phase shifting (TPS).

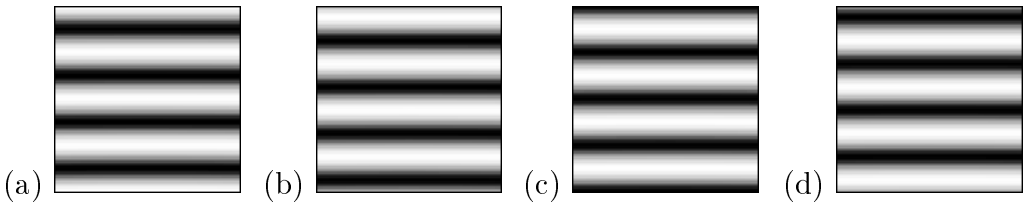

Figure 1.11: Frames of intensity data with phase shifts of $\pi/2$.

At least three intensity measurements of I_g with differing phase shifts are required to determine the phase difference $\Delta\Phi$. Figure 1.11 shows four different frames of intensity data with phase shifts of $\pi/2$ (90°). The first and the third frame have a phase shift of π, and thus the intensities are complementary.

When the phase shift changes by the amount $\Delta\beta$ during the integration time of the detector, e.g. a pixel of a CCD camera, the intensity is given by [74, 75]

$$I_i = \frac{1}{\Delta\beta} \int_{\beta_i - \Delta\beta/2}^{\beta_i + \Delta\beta/2} I_0 \left(1 + \gamma_0 \cos\left[\Phi + \beta\left(t\right)\right]\right) d\beta\left(t\right), \tag{1.71}$$

$$I_i = I_0 \left(1 + \gamma \cos\left(\Phi + \beta_i\right)\right), \tag{1.72}$$

with

$$\gamma = \gamma_0 \frac{\sin\left(\Delta\beta/2\right)}{\Delta\beta/2}, \tag{1.73}$$

where $\beta\left(t\right)$ is the relative phase shift between the measurement and the reference beam as function of time, β_i the average value of the phase shift, γ and γ_0 the visibilities or fringe visibilities. The term $1/\Delta\beta$ normalizes the result. A special case is the so-called phase stepping, where the phase is constant during image capturing ($\Delta\beta = 0$) and is then changed between the image capturing processes. The phase-stepping method has the maximum visibility $\gamma = \gamma_0$. When the phase is integrated, i.e. $\Delta\beta \neq 0$, the visibility γ is reduced. The integration of the intensity over a full period ($\Delta\beta = 2\pi$) of the phase shift reduces the visibility γ to zero. To obtain good visibility, the integration period is restricted to

$$\Delta\beta \in \left]0, \pi\right[. \tag{1.74}$$

The integration of the phase reduces the visibility, but it has the advantage that it reduces the noise during the integration time. To achieve measurements with a precision of $\lambda/100$, the interferometer set-up has to be placed on a vibration-isolated table, and the beam paths have to be enclosed to minimize the effects of vibration and air turbulence [73].

1.3.1 Phase-shifting algorithms

Equation (1.72) is applicable to any kind of phase-shifting method. At least three intensities I_i with differing average phase shifts β_i are required to determine the phase Φ modulo π or 2π. The following algorithms are different in the required number of different intensities I_i, the amount of phase shift between intensity measurements and how much they are prone to errors in the phase shift or to perturbations, such as vibration and turbulence. An overview of several algorithms is given in [73, 76].

The three-frame algorithm requires a minimum amount of three intensity measurements with equal and known phase shifts

$$\beta_{i+1} - \beta_i = \beta_{c1}, \quad i = 1, 2, 3 \tag{1.75}$$

and is the simplest one to use. Two phase step sizes commonly used are $\pi/2$ and $2\pi/3$. This simplifies the calculation, but this algorithm is very sensitive to errors in the phase shift β_{c1}.

A frequently used algorithm is the four-frame algorithm, which requires four intensity measurements with phase shifts of $\beta_{c1} = \pi/2$. The Carré algorithm is a variation of this algorithm, but the phase shift is treated as unknown [77]. Thus, the phase shift does not need to be calibrated. A linear phase shift of β_i is assumed and yields four equations

$$I_{11} = I_{01}\left(1 + \gamma_1 \cos\left(\Phi_1 - \frac{3}{2}\beta_{c1}\right)\right), \tag{1.76a}$$

$$I_{21} = I_{01}\left(1 + \gamma_1 \cos\left(\Phi_1 - \frac{1}{2}\beta_{c1}\right)\right), \tag{1.76b}$$

$$I_{31} = I_{01}\left(1 + \gamma_1 \cos\left(\Phi_1 + \frac{1}{2}\beta_{c1}\right)\right), \tag{1.76c}$$

$$I_{41} = I_{01}\left(1 + \gamma_1 \cos\left(\Phi_1 + \frac{3}{2}\beta_{c1}\right)\right). \tag{1.76d}$$

From these equations the phase modulo π can be calculated using

$$\Phi = \arctan \frac{\left\{\left[3\left(I_{21} - I_{31}\right) - \left(I_{11} - I_{41}\right)\right]\left[\left(I_{21} - I_{31}\right) + \left(I_{11} - I_{41}\right)\right]\right\}^{1/2}}{\left(I_{21} + I_{31}\right) - \left(I_{11} + I_{41}\right)}, \tag{1.77}$$

and the phase shift with

$$\beta_{c1} = 2\arctan\left(\frac{3\left(I_{21} - I_{31}\right) - \left(I_{11} - I_{41}\right)}{\left(I_{21} - I_{31}\right) + \left(I_{11} - I_{41}\right)}\right)^{1/2}. \tag{1.78}$$

Assuming that the phase shift β_{c1} is near $\pi/2$, the visibility is given by

$$\gamma = \frac{1}{2I_0}\left(\frac{1}{2}\left[(I_{21}-I_{31})+(I_{11}-I_{41})\right]^2 + \frac{1}{2}\left[(I_{21}+I_{31})-(I_{11}+I_{41})\right]^2\right)^{1/2}. \quad (1.79)$$

When the phase shift is off by 10°, the estimation of γ will be off by ± 10 % [76]. The phase calculation can be extended to Φ modulo 2π when the signs of $\sin\Phi$ and $\cos\Phi$ are considered. These signs can be determined from

$$I_{21} - I_{31} = -2\beta_{c1} I_{01} \sin\frac{\beta_{c1}}{2}\sin\Phi_1, \quad (1.80)$$

and

$$(I_{21}+I_{31}) - (I_{11}+I_{41}) = 8\beta_{c1} I_{01}\cos\frac{\beta_{c1}}{2}\sin^2\frac{\beta_{c1}}{2}\cos\Phi_1, \quad (1.81)$$

when $\beta_{c1} \in]0,\pi[$ is assumed. The result of the Carré algorithm, called the wrapped phase, is shown in Fig. 1.12, where the four frames of intensity data

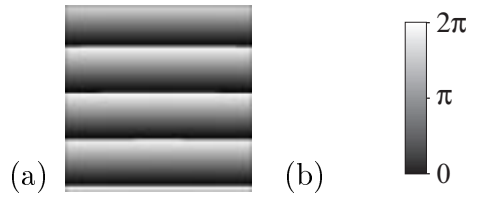

Figure 1.12: Phase-shifting image (a) of the frames of Fig. 1.11 and (b) gray scales of the phase-shifting image.

of Fig. 1.11 are used. The phase difference is 2π for a change in gray scales from black, over different levels of gray, to white. The discontinuities, the changes from black to white for adjacent pixels, may be eliminated by phase-unwrapping methods. Another algorithm using four intensity measurements and eliminating the errors caused by linear adjustment derivations, is described in [78]. A further algorithm which is insensitive to phase shift errors, is the five-frame or Hariharan algorithm [79, 80]. Five intensity measurements I_i, $i = 1,\ldots 5$, with linear phase shifts of $\pi/2$ between the intensity measurements lead to the simple calculation

$$\Phi = \arctan\frac{2\,(I_2 - I_4)}{2I_3 - I_5 - I_1}. \quad (1.82)$$

This algorithm reduces the possibility of having the numerator and the denominator tend to zero. Thus, the uncertainty in the calculation is reduced, and this algorithm can tolerate large errors in the phase shift. The Hariharan algorithm is a special case of the $(N+1)$-frame algorithm, which has an extra intensity measurement with a 2π phase shift relative to the first intensity measurement [81]. This extra intensity measurement helps to reduce the error sensitivity.

For a total number of N intensity measurements with known average values of the phase shifts β_i, with $i = 1 \ldots N$, the phase can be calculated using a least-squares method. The values β_i do not need to be evenly spaced and can be spread over a range greater than 2π. However, the choice of β_i influences the sensitivity to phase shift errors. If the integration period $\Delta\beta$ in equation (1.31) is constant for every intensity measurement, the least-squares solution is given in [74, 82]. A generalized least-squares solution is developed in [83].

In general, the calculation of the phase can be expressed as

$$\Phi_1 = \arctan \frac{g_1}{h_1}. \tag{1.83}$$

When the signs of g_1 and h_1 correspond to the signs of $\sin \Phi 1$ and $\cos \Phi 1$, respectively, the phase Φ_1 modulo 2π can be derived. In speckle interferometry the phase change $\Delta\Phi$, with $\Phi_2 = \Phi_1 + \Delta\Phi$, has to be determined. The phase change may be introduced by a deformation or a wavelength change. Phase Φ_2 is derived by

$$\Phi_2 = \arctan \frac{g_2}{h_2}, \tag{1.84}$$

in the same way as phase Φ_1, and, for instance, with the Carré algorithm from a second set of phase-shifted intensity measurements

$$I_{12} = I_{02}\left(1 + \gamma_2 \cos\left(\Phi_2 - \frac{3}{2}\beta_{c2}\right)\right), \tag{1.85a}$$

$$I_{22} = I_{02}\left(1 + \gamma_2 \cos\left(\Phi_2 - \frac{1}{2}\beta_{c2}\right)\right), \tag{1.85b}$$

$$I_{32} = I_{02}\left(1 + \gamma_2 \cos\left(\Phi_2 + \frac{1}{2}\beta_{c2}\right)\right), \tag{1.85c}$$

$$I_{42} = I_{02}\left(1 + \gamma_2 \cos\left(\Phi_2 + \frac{3}{2}\beta_{c2}\right)\right). \tag{1.85d}$$

The phase change

$$\Delta\Phi = \Phi_2 - \Phi_1 \tag{1.86}$$

may be derived using equations (1.83) and (1.84):

$$\Delta\Phi = \arctan\frac{g_2}{h_2} - \arctan\frac{g_1}{h_1}. \tag{1.87}$$

More accurate results are obtained by

$$\begin{aligned}\Delta\Phi &= \arctan\frac{\sin(\Phi_2 - \Phi_1)}{\cos(\Phi_2 - \Phi_1)} \\ &= \arctan\frac{\sin\Phi_2\cos\Phi_1 - \cos\Phi_2\sin\Phi_1}{\cos\Phi_1\cos\Phi_2 + \sin\Phi_1\sin\Phi_2},\end{aligned} \tag{1.88}$$

and thus

$$\Delta\Phi = \arctan\frac{g_2h_1 - g_1h_2}{h_1h_2 + g_1g_2}. \tag{1.89}$$

The phase change $\Delta\Phi$ is calculated directly from all the measured intensities given in (1.76a) to (1.76d) and (1.85a) to (1.85d).

1.3.2 Phase-shifter calibration

Some of the algorithms are sensitive to errors in the phase shift, and the algorithms which are tolerant to phase errors, require calibrations for the best performance. The most obvious way to determine the phase shift is to use equation (1.78) of the Carré algorithm. A simpler equation can be found using five intensity measurements I_i, with $i = 1 \ldots 5$ [79]:

$$\beta = \arccos\frac{I_5 - I_1}{2(I_4 - I_2)}. \tag{1.90}$$

The third intensity I_3 is not needed for this calculation. These calculations assume equal phase shifts between the intensity measurements, and the phase shift between two intensity measurements cannot be determined.

In phase-shifting speckle interferometry, the phase shift between two speckle images may be determined if the phase shift is equal for any pixel of the speckle pattern. Assuming that the phase shift β is in the range $[0, \pi[$, it is given by

$$\beta = \arccos C_{12}, \tag{1.91}$$

where C_{12} is the correlation function of equation (1.12), the correlation between two speckle images I_1 and I_2, and the ensemble average $\langle\rangle$ is replaced by the average over the pixels of the speckle images.

1.3.3 Phase modulation

The most common method used to introduce the time-varying phase shift in TPS systems is translating a mirror in the interferometer by a piezoelectric transducer, e.g. the mirror M1 in Fig. 1.3 or the reference mirror in Fig. 1.6. The phase shift

$$\beta = \frac{4\pi}{\lambda} x_d \tag{1.92}$$

depends on the change of the path length $2x_d$ introduced by the movement of the mirror by the amount x_d.

To introduce a phase shift of $\pi/2$, the path length has to be changed by the amount of $\lambda/4$, i.e. in the range of 100 nm to 200 nm for the visible light. Alternative methods for producing a phase shift are tilting a plane-parallel plate, moving a glass wedge, translating a grating, using an acoustic-optic or an electro-optic modulator, or rotating a half-wave plate when the object and the reference beams are perpendicularly polarized to each other [73, 76, 84]. Another method is to stretch an optical single-mode fiber. When a polarization-preserving fiber is used, the fringe contrast and the visibility do not decrease due to the change of the state of polarization [85].

1.3.4 Visibility

The visibility γ in equation (1.70)

$$\begin{aligned} I &= I_0 \left(1 + \gamma \cos\left(\Phi + \beta\right)\right) \\ &= I_o + I_r + 2 \left(I_o I_r\right)^{1/2} \cos\left(\Phi + \beta\right) \end{aligned} \tag{1.93}$$

for the temporal phase-shifting methods depends on the ratio between the object intensity I_o and the reference intensity I_r. The larger the visibility, the more accurate are the results, i.e. the calculated phase Φ, when perturbations disturb the phase calculation. If both the reference wave and the object wave are smooth, the maximum visibility $\gamma = 1$ is obtained with equal intensities, i.e. $I_o = I_r$.

In phase-shifting speckle interferometry one speckle field is superposed by either another speckle field or a smooth reference wave. Thus, the background intensity I_0 and the visibility γ are different for each pixel of the detector. The phase calculation leads to less accurate results for pixels which either have a low visibility or which saturate.

For fully resolved speckle patterns, i.e. when the pixel size is smaller than the speckle size, the optimum configuration of a speckle interferometer with a smooth reference wave is given in [86]. The reference beam intensity I_r has to be set at one fourth of the saturation intensity I_{sat} of the detector,

and in any case the intensity I_r should exceed the mean object intensity $\langle I_o \rangle$ over the whole speckle pattern. The visibility increases with the ratio of the reference intensity to the mean object intensity $I_r : \langle I_o \rangle$ in the range of 1 up to an intensity ratio where the visibility reaches its maximum. For larger intensity ratios the visibility decreases again. Measurements may be performed until the intensity $\langle I_o \rangle$ becomes less than the electronic noise of the detector, e.g. a ratio of 100 : 1 [87]. An optimal ratio of 5.7 : 1 with a mean speckle intensity of 0.06 I_{sat} is derived in [88] for a two-wavelength speckle interferometer.

In the case where two fully resolved speckle fields are superposed, the mean intensities $\langle I_r \rangle$ and $\langle I_o \rangle$ should be equal and must never exceed one fourth of the saturation intensity I_{sat} [89]. Differences in the intensities I_r and I_o do not have a severe impact on the phase calculation.

Measurements may be carried out with speckles considerably smaller than the pixel size. In the case of a smooth reference wave, the best visibility is obtained with fully resolved speckle patterns. However, the phase calculation is not affected too much by errors, when it is integrated over several speckles per pixel [90]. In the case where two speckle fields are superposed, the integration over more than 50 speckles per pixel leads to satisfactory results [71]. It may be useful not to resolve the speckle pattern perfectly in some cases, e.g. by limited laser power or by reducing the effect of decorrelation [91].

1.4 Spatial phase-shifting methods

Temporal phase-shifting methods require a time sequence of intensity measurements. Thus, this method is susceptible to time-dependent perturbations, for instance, the measurement object together with the measurement set-up have to be placed on a vibration-isolated table. In the spatial phase-shifting methods the intensity measurements are recorded simultaneously, either by several detectors with an appropriate phase shift for each of the intensity measurements or by spatial-carrier methods based on a large tilt between the reference and the measurement wavefronts. An overview of different spatial phase-shifting methods is given in [92].

1.4.1 Phase-stepping methods

The phase-stepping methods in spatial phase shifting generate simultaneously at least three spatially separated phase-stepped interferograms. Thus, this is a multichannel method with at least three parallel channels. The

interferograms with different phase shifts may be separated by means of polarization optics [93, 94] or diffraction gratings [95, 96, 97, 98].

In [99] a computer-generated diffractive optical element is used as a modified phase grating to diffract the light into four channels with a known phase shift between each channel. The four phase-stepped speckle images are recorded with one CCD camera. Thus, the set-up is simple, but the lateral resolution is reduced.

The three-channel polarization approach with three CCD cameras developed by van Haasteren [100, 101] uses quarter-wave plates to introduce the phase shifts between the object and the reference beams which are perpendicularly polarized to each other. Three speckle images with phase steps of $\pi/2$ may be recorded simultaneously. Since the employed components, such as the quarter-wave plates, depend on the wavelength of the light, only measurements with one wavelength may be performed without changing the amount of the phase shift. Thus, this set-up allows measurements with only one wavelength but without reduction of the lateral resolution. A more compact set-up, where four phase-stepped speckle images are recorded with two CCD cameras, is reported in [102]. However, the spatial resolution is reduced.

The same formulas used for the temporal phase shifting may be applied for the spatial phase shifting, see equation (1.70) and the phase-shifting algorithms in section 1.3.1.

1.4.2 Spatial carrier methods

The spatial carrier methods require only one speckle image, in which a large tilt is introduced between the smooth reference and the measurement wavefront, instead of several phase-stepped speckle images. The intensity of a pixel (i, n) of the speckle image is also given by equation (1.70)

$$I(i,n) = I_0(i,n)\left(1 + \gamma(i,n)\cos\left[\Phi(i,n) + \beta_i\right]\right), \tag{1.94}$$

with

$$\beta_i = \omega_s i, \tag{1.95}$$

where (i, n) corresponds to the spatial coordinates (x, y) and ω_s is a spatial carrier frequency generated by tilting the plane reference wavefront. The phase shift between two adjacent pixels, e.g. the pixels $(i + 1, n)$ and (i, n), is ω_s. Since the object wave is a speckle field, the variables I_0, γ, and Φ are not at all constant over all pixels. If the background intensity I_0, the visibility γ and the phase Φ vary slowly with the spatial carrier frequency, the phase may be calculated from the intensities of at least three adjacent pixels in the x-direction. The spatial carrier frequency obeys these conditions in the bright

parts of the speckle field, i.e. in the speckle spots [103, 104, 105, 106]. Thus, phase $\Phi(i,n)$ can be determined from N intensity values of adjacent pixels in the x-direction in the speckle spots, i.e. the speckle size in the x-direction has to be greater than N pixels.

The standard phase-shifting algorithms explained in section 1.3.1 may be applied if the phase shift β_i is chosen accordingly. Generally, the spatial carrier methods require much more complex processing and more computing time to determine the phase than do the phase-stepping methods. The two basic approaches are the Fourier transform method, where a filtering process in the spatial frequency domain is applied, and methods which are equivalent to the Fourier transform method, but the filtering process is performed in the space domain [92].

The spatial carrier methods require a minimum speckle size of several pixels, and the phase is calculated from intensities of adjacent pixels. Thus the lateral resolution is reduced. For the out-of plane measurement of larger displacements the performance of the spatial carrier methods becomes comparable to that of the temporal phase shifting when the Fourier transform method is applied [87].

1.5 Phase unwrapping

Most of the phase-shifting algorithms result in an equation of the form

$$\Phi = \arctan \frac{g}{h}, \tag{1.96}$$

where g and h are functions of phase-shifted intensity measurements. The solution of this equation is the wrapped phase of the form of a sawtooth function with discontinuities, i.e. with edges when fraction g/h changes by 2π. This problem exists in all methods of interferometry which consist of the interference of two sinusoidal wave functions. Methods which eliminate the edges are known as phase-unwrapping methods. The simplest method is realized by finding the edges and adding $\pm 2\pi$ to the wrapped phase when passing an edge.

In speckle interferometry the calculated wrapped phase Φ is not perfect and is subject to errors caused, for instance, by perturbations, electronic noise, and speckle noise. Thus, phase unwrapping becomes more complicated and phase-unwrapping methods more complex. A good overview of phase-unwrapping methods is given in [107]. A novel approach to minimize the impairment of phase unwrapping and surface reconstruction by noise is described in chapter 2.

Chapter 2

Surface reconstruction

The temporal phase-shifting technique in speckle interferometry, described in section 1.3, results in several, differing speckle images. From these speckle images, a wrapped phase is calculated, which describes three-dimensionally and clearly the measured deformation or surface slope, but this phase contains edges. Since the error in the phase is larger at the edges than between the edges, four phase-shifted phase images with a bias phase step of $\pi/2$, are calculated. Since the edges now occur at different positions, the ill-conditioned phase near the edges is not used for unwrapping. The edge detection is performed by wavelet transformation because it analyzes on different scales. Thus it is possible to distinguish structures on large scales and disturbances on small scales. Finally, the Bayesian probability theory is used to find the most probable spline to the unwrapped phase. In this chapter the basics of wavelet theory and of Bayesian probability theory, and the three-dimensional reconstruction are described.

2.1 Wavelet theory

The wavelet theory is based on the use of a transformation with scaled and translated versions of a single function proposed by Morlet [108, 109] for the time-resolved frequency analysis of seismic data. Although the wavelet analysis is a young field of applied science, a lot of applications exist already, e.g. the time-resolved frequency analysis of acoustic signals [109, 110, 111], or signals of electrocardiographs [112, 113]. In mathematics, the wavelet transformation is used to solve differential equations numerically [114, 115], and in digital image processing [116, 117] it is employed for pattern recognition [118, 119] or image compression [120, 121, 122], e.g. for finger-print images [123, 124]. The optical implementation of the two-dimensional wavelet trans-

formation enables real-time applications [125, 126]. It is also being employed in fusion research [127, 128]. In speckle measurement techniques, the wavelet transformation is applied, for example, for surface roughness determination [129], speckle noise reduction [130], minima detection [131], and edge detection [132].

The wavelet transformation definition is based on a mother wavelet ψ. From the mother wavelet, a set of wavelets $\psi_{a,b}$ is generated by dilatations and translations, e.g. if it is one-dimensional:

$$\psi(x) = |a|^{-1/2} \psi\left(\frac{x-b}{a}\right). \tag{2.1}$$

The one-dimensional continuous wavelet transformation of the signal $f(x)$ is defined as

$$(T^{wav} f) = \langle f, \psi_{a,b} \rangle = \int f(x)\, \psi^*_{a,b}(x)\, dx. \tag{2.2}$$

The parameters a and b are continuous, and $a \neq 0$. The wavelets are scaled by factor a and translated by factor b. Thus, parameter a controls the frequency contents, and parameter b controls the location of the wavelets. The wavelet transformation can be interpreted as the decomposition of signal $f(x)$ into a set of frequency channels defined by the various wavelets, or can be interpreted as the correlation operation between signal $f(x)$ and the wavelet function $\psi_{a,b}(x)$ [125]. The mother wavelet and the dilated, translated versions of wavelets are normalized to [133]

$$\|\psi\| = \|\psi_{a,b}\| = \left[\int |\psi_{a,b}(x)|^2\, dx\right]^{1/2} = 1. \tag{2.3}$$

The signal may be completely reconstructed by the inverse wavelet transformation

$$f = C_\psi^{-1} \int_{-\infty}^{\infty} \int_{-\infty}^{\infty} \langle f, \psi_{a,b} \rangle \psi_{a,b} \frac{da\, db}{a^2}, \tag{2.4}$$

where C_ψ is a normalization constant and is defined as

$$C_\psi = 2\pi \int_{-\infty}^{\infty} \left|\hat{\psi}(\xi)\right|^2 |\xi|^{-1}\, d\xi. \tag{2.5}$$

$\hat{\psi}(\xi)$ is the Fourier transform of the mother wavelet $\psi(x)$:

$$\hat{\psi}(\xi) = \frac{1}{\sqrt{2\pi}} \int \exp(j\xi x) \psi(x)\, dx. \tag{2.6}$$

The inverse wavelet transformation (2.4) requires that C_ψ^{-1} be unequal to zero, i.e. that C_ψ will be finite:

$$C_\psi < \infty. \tag{2.7}$$

This condition is the admissible condition that the wavelet must satisfy. This restriction has to be considered when choosing the mother wavelet $\psi(x)$. It implies that

$$\hat{\psi}(0) = 0, \tag{2.8}$$

and therefore

$$\int \psi(x)\, dx = 0. \tag{2.9}$$

Hence, to have an admissible wavelet transformation, the mother wavelet must have a mean value of zero.

In practice, such wavelets are used which are localized both in time domain and in frequency domain [133]. Depending on the problem to be solved different mother wavelets are employed, e.g. the Morlet wavelet for the time-resolved frequency analysis of seismic data [109, 134], or the Mexican hat wavelet for pattern recognition in images [135, 136].

A method to create mother wavelets ψ satisfying the admissible condition (2.7) consists of differentiating a k times differentiable function φ:

$$\psi(x) := \varphi^{(k)}(x), \tag{2.10}$$

with $\varphi, \varphi^{(k)} \in L^2(\mathcal{R})$, and $\varphi^{(k)} \neq 0$ [137]. An example is the Mexican hat wavelet, the second derivative of a Gaussian function [135]. Until now, only one dimension is considered. In case it is two-dimensional, the mother wavelet is derived by

$$\vec{\psi}(\vec{x}) = \vec{\nabla}\varphi(\vec{x}), \tag{2.11}$$

with $\vec{x} = (x, y)$. With a dilation or scale parameter which is now called s, the dilated wavelets are

$$\vec{\psi}_s(\vec{x}) = \vec{\nabla}\varphi_s(\vec{x}), \tag{2.12}$$

with

$$\varphi_s(\vec{x}) = \varphi\left(\frac{\vec{x}}{s}\right). \tag{2.13}$$

The two-dimensional wavelet transformation with the translation vector $\vec{x}'$ can be expressed as

$$\begin{aligned} \vec{F}(s, \vec{x}') &= \iint f(\vec{x})\, \psi_s(\vec{x} - \vec{x}')\, dx\, dy \\ &= s\vec{\nabla}(f * \varphi_s)(\vec{x}'), \end{aligned} \tag{2.14}$$

with the convolution product

$$(f * \varphi)(\vec{x}') = \iint f(\vec{x})\, \varphi(\vec{x}' - \vec{x})\, dx\, dy. \tag{2.15}$$

This formula shows that the wavelet transformation is the gradient of function $f(\vec{x})$ smoothed by the dilated function $\varphi_s(\vec{x})$. The scale parameter s determines the region of the function over which smoothing will be done. An example is the two-dimensional Gaussian

$$\varphi_s(\vec{x}) = \frac{1}{2\pi s} \exp\left(-\frac{1}{2}\left|\frac{\vec{x}}{s}\right|^2\right), \tag{2.16}$$

which leads to the translated and dilated wavelets

$$\vec{\psi}_s(\vec{x}, \vec{x}') = \frac{-1}{2\pi s^3} \exp\left(-\frac{1}{2}\left|\frac{\vec{x} - \vec{x}'}{s}\right|^2\right)(\vec{x} - \vec{x}')\,. \tag{2.17}$$

One wavelet component dilated with $s = 1$ and translated with $\vec{x}' = (5, 5)$ is shown in Fig. 2.1. In one direction it is a Gaussian, and in the other

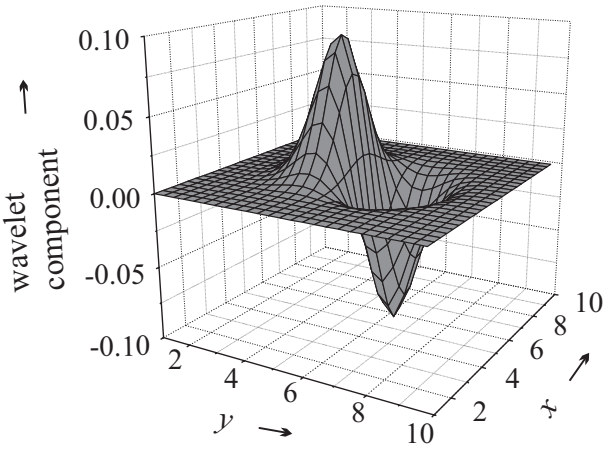

Figure 2.1: Two-dimensional wavelet component with $s = 1$ and $\vec{x}' = (5, 5)$.

direction it is the first derivative of a Gaussian. Figure 2.2(b) shows one line of the middle of Fig. 2.1, and Figs. 2.2(b), (c), and (d) show wavelet components with different translations and dilations. Using this wavelet, the wavelet transform can be used for searching structures in images, as shown in [128, 131, 132].

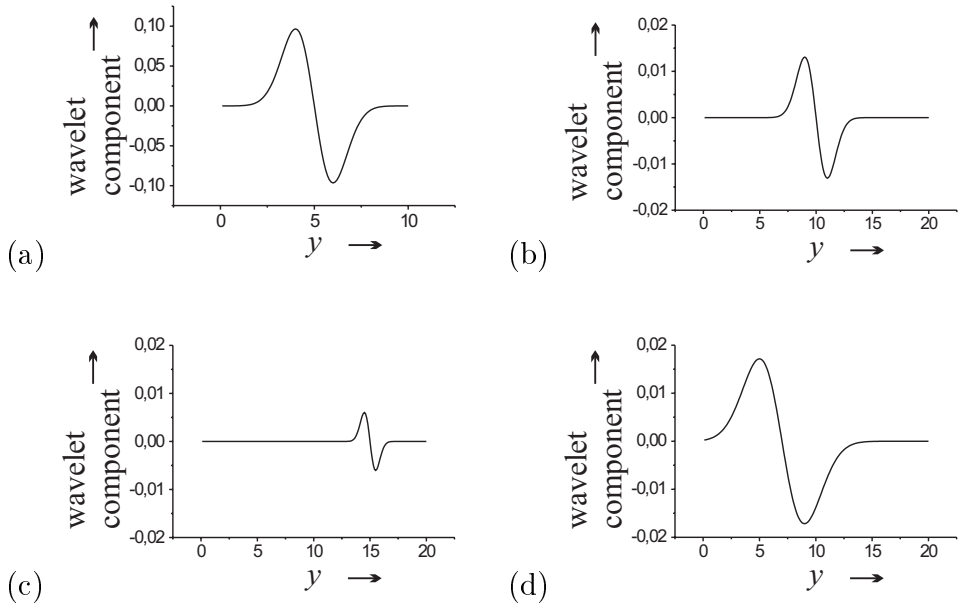

Figure 2.2: One-dimensional wavelet components with different translations and dilatations: $x = 5$, and (a) $s = 1$, $\vec{x}' = (5, 5)$, (b) $s = 1$, $\vec{x}' = (3, 10)$, (c) $s = 2$, $\vec{x}' = (5, 15)$, (d) $s = 0.5$, $\vec{x}' = (11, 7)$.

2.2 Bayesian probability theory

Data analysis with Bayesian probability theory is of great interest for extracting information from measured data. Since all measurements are affected by noise due to many different causes, such as vibration, temperature, air turbulence, or electrical noise, the Bayesian probability theory is an appropriate tool. The Bayesian probability theory is not new, but recently there has been a massive growth of interest in Bayesian methods. Developments in computer technology have made Bayesian methods feasible for solving problems with large numbers of parameters and with complex models. Thus, the Bayesian probability theory is applied in different fields [138], such as fusion research [128], speckle interferometry [131, 132], and signal processing [139].

2.2.1 Conditional probability

The Bayesian view of probability is that probabilities are always conditional, and this conditioning must be stated explicitly [140]. The probability reveals how much we believe that a proposition is true, and this belief should be based on all relevant information available. This simply means that only

two people having the same information should assign the same probability. Cox's work [141] shows the range of validity of the probability theory and its rules based on the concepts of the pioneers Bayes [142], Bernoulli [143], and Laplace [144]. These concepts have been reconsidered by Jeffreys [145].

The probability of the proposition A_i conditional on the data D and the information K (the knowledge) is given by

$$p\,(A_i|D,K)\,, \tag{2.18}$$

where the vertical bar '|' means 'given'. All items to the right of this conditioning symbol are taken as being true. The comma is read as the conjunction 'and'. The product rule

$$p\,(B,A_i|K) = p\,(B|A_i,K)\,p\,(A_i|K) \tag{2.19}$$

states that the probability that both B and A_i are true, given the information K, is equal to the probability that B is true, given that A_i and K are true, times the probability that A_i is true, given K. The sum rule is given by

$$p\,(B|K) + p\,(\mathrm{not}(B)|K) = 1, \tag{2.20}$$

and the marginalization rule is given by

$$p\,(B|K) = \sum_i p\,(B,A_i|K), \tag{2.21}$$

with a mutually exclusive and exhaustive set of possibilities $\{A_i\}$:

$$\sum_i p\,(A_i|K) = 1. \tag{2.22}$$

These rules are analogous to the rules of the frequency definition of the probability theory [140, 146].

2.2.2 Bayes' theorem

For data analysis problems, the probability $p\,(A_i|D,K)$ of the proposition A_i, given the data D and the information K, is of interest. The proposition A_i may be a hypothesis, a model or parameters, and the information K the physical knowledge of the problem. Bayes' theorem

$$p\,(A_i|D,K) = \frac{p\,(D|A_i,K)\,p\,(A_i|K)}{p\,(D|K)} \tag{2.23}$$

follows from the product rule (2.19) by turning around A_i and B. The fact that the probability of both A_i and D are true, implies $p(A_i,D|K) =$

$p(D, A_i|K)$. Bayes' theorem is the most important equation in Bayesian probability theory because it relates the probability that the proposition A_i is true, given the data, to the probability that the measured data would have been observed if the proposition A_i was true. The probability of $p(A_i|D, K)$ after measuring data D, is expressed by the probability $p(D|A_i, K)$ before measuring new data.

The terms in Bayes' theorem have formal names. The posterior probability $p\,(A_i|D, K)$ is expressed by the prior probability $p\,(A_i|K)$, the likelihood function $p\,(D|A_i, K)$, and the evidence $p\,(D|K)$. The evidence is simply a normalization factor calculated by the marginalization rule (2.21):

$$p\,(D|K) = \sum_i p\,(D|A_i, K)\, p\,(A_i|K). \tag{2.24}$$

The prior probability reveals the state of knowledge before measuring the data, and the posterior probability reveals the state of knowledge of the truth of the proposition A_i in the light of the measured data. The likelihood function reveals the probability of the measured data if proposition A_i were true. This means that Bayes' theorem encapsulates the process of learning.

Prior probability

The prior probability expresses the state of knowledge before the measurement of new data. This knowledge can, for example, be revealed as expectation values of observables O_ν [147]:

$$\langle O_\nu \rangle = \sum_i p\,(A_i|K)\, O_\nu\,(A_i). \tag{2.25}$$

In general, there exists an infinite number of probability distributions complying with equation (2.25). In order to use as few restrictions as possible, the probability distribution with the highest uncertainty is chosen [148]. Of course, this probability distribution has to comply with the expectation values. To quantify the uncertainty of the probability distribution, the Shannon entropy [149]

$$S = -\sum_i p\,(A_i|K) \ln p\,(A_i|K) \tag{2.26}$$

is used. If the proposition A_i is true, the entropy is equal to zero, if not, it is greater than zero [148]. Jaynes' principle of maximum entropy maximizes the entropy S on condition that $p\,(A_i|K)$ is normalized according to equation (2.22) and fulfills equation (2.25) for the expectation values. Starting with the Lagrange function

$$\mathcal{L} = S - \mu_0 \left(\sum_i p\,(A_i|K) - 1 \right)$$

$$-\sum_{\nu} \mu_\nu \left(\sum_i p\left(A_i|K\right) O_\nu\left(A_i\right) - \langle O_\nu \rangle \right), \tag{2.27}$$

and with Lagrange parameters μ_0 and μ_ν, the global maximum of $\mathcal{L}$ is determined via $\partial\mathcal{L}/\partial p\left(A_i|K\right) = 0$ [148] and yields the desired probability distribution

$$p\left(A_i|\mu_1, \mu_2, \ldots, \mu_n, K\right) = \frac{\exp\left(-\sum\limits_{\nu=1}^{n} \mu_\nu O_\nu\left(A_i\right)\right)}{\sum\limits_i exp\left(-\sum\limits_{\nu=1}^{n} \mu_\nu O_\nu\left(A_i\right)\right)}. \tag{2.28}$$

This probability distribution shows best the state of knowledge. Every probability distribution with lower entropy is incorrect, because the reduction of entropy needs additional information which is not given.

If the expectation values of the observables $\langle O_\nu \rangle$ with $\nu = 1, 2, \ldots k \leq n$, are known, the Lagrange parameters μ_ν can be derived. If, however, the expectation values of the observables are unknown, the hyperparameters μ_ν have to be integrated out according to the marginalization rule (2.21). This yields

$$\begin{aligned} p\left(A_i|K\right) = & \int_0^\infty p\left(A_i|\mu_1, \mu_2, \ldots, \mu_k, K\right) p\left(\mu_1|K\right) p\left(\mu_2|K\right) \ldots p\left(\mu_k|K\right) \\ & d\mu_1\, d\mu_2\, \ldots\, d\mu_k, \end{aligned} \tag{2.29}$$

where $p\left(\mu_\nu|K\right)$ are probabilities for the hyperparameters μ_ν, which control the expectation values $\langle O_\nu \rangle$. The hyperparameters μ_ν depend on the scale used for the observables, but the probability $p\left(\mu_\nu|K\right)$ has to be independent from the scale. In case of the most ignorant prior, the scale-invariant prior probability of hyperparameters according to Jeffreys [150] is

$$p\left(\mu_\nu|K\right) \sim \frac{1}{\mu_\nu}, \tag{2.30}$$

and is called Jeffreys' prior. This prior probability of hyperparameters is uniformly distributed over all scales. Now, the prior probability $p\left(A_i|K\right)$ can be calculated.

Likelihood function

The likelihood function $p\left(D|A_i, K\right)$ reveals the probability of the data $D = \{d_1, d_2, \ldots d_N\}$, assuming that the proposition A_i and the information K are true. Every data point consists of the value d_m and the error σ_m. The

assumption that the proposition A_i is true, yields theoretical data values $d_{t,m}$. Employing the principle of maximum entropy [140], the likelihood function is obtained. With the normalization

$$\sum_{m=1}^{N} p\left(D|A_i, \sigma_1, \sigma_2, \ldots, \sigma_N, K\right) = 1, \tag{2.31}$$

the first and the second moment

$$\langle d_m \rangle = d_{t,m}, \tag{2.32}$$

$$\langle (d_m)^2 \rangle = (d_{t,m})^2, \tag{2.33}$$

and the variances

$$\langle (d_m - d_{t,m})^2 \rangle = (\sigma_m)^2, \tag{2.34}$$

the global maximum of the Lagrange function is derived, as described before:

$$p\left(D|A_i, \sigma_1, \sigma_2, \ldots, \sigma_N, K\right) \sim \exp\left(-\frac{1}{2}\chi^2\right), \tag{2.35}$$

with

$$\chi^2 = \sum_{m=1}^{N} \left(\frac{d_m - d_{t,m}}{\sigma_m}\right)^2. \tag{2.36}$$

The probability depends on the difference between data values and theoretical data values, weighted with the errors. This normal distribution is the distribution with maximized entropy and the known moments one and two. The assumption that the errors are normally distributed, would lead to the same result, viz. to equation (2.35) [151].

If the errors σ_m are unknown, these hyperparameters are integrated out employing the marginalization rule (2.21) with

$$p\left(D|A_i, K\right) \sim \int_0^\infty p\left(D|A_i, \sigma_1, \sigma_2, \ldots, \sigma_N, K\right) p\left(\sigma_1|K\right) p\left(\sigma_2|K\right) \ldots p\left(\sigma_N|K\right) d\sigma_1 d\sigma_2 \ldots \sigma_N. \tag{2.37}$$

With Jeffreys' prior, as described before,

$$p\left(\sigma_m|K\right) \sim \frac{1}{\sigma_m}, \tag{2.38}$$

the likelihood function is calculated to be

$$p\left(D|A_i, K\right) \sim \exp\left(-\frac{N}{2} \ln \chi^2\right). \tag{2.39}$$

This is a Student's t-distribution [146].

The Bayesian probability theory contains the principle of the 14th century Franciscan monk Wilhelm von Ockham: 'it is vain to do with more what can be done with fewer' [152]. The simplest available theory to fit the facts well, revealed by the proposition A_i, should be preferred. This logical principle of economy is known as Ockham's Razor. In the Bayesian probability theory, the more complex model is chosen if the data give rise to the complex model, but the simpler model is preferred if it agrees with the data [140].

2.3 Unwrapping

Unwrapping methods are well-known in phase-shifting speckle interferometry. One method of unwrapping phase-shifting speckle interferometry images is realized by means of finding the edges in the phase-shifting image and adding $\pm 2\pi$ to the wrapped phase, when passing an edge. The described method uses a wavelet transformation to find the edges in a binary image. Since the error in the phase is larger at the edges than in between, four phase-shifted phase images are used to identify regions of well-conditioned input data. Thus, the hampering influence of the noise is minimized.

To perform a surface slope measurement, several phase-shifted images are necessary with at least two differing wavelengths of illuminating laser light. In case of a deformation measurement, two series with phase-shifted speckle images before and after the deformation are recorded with the same wavelength. The wrapped phase can be calculated with different algorithms, depending on the number of phase-shifted speckle images, and depending on the phase shift, as described in section 1.3.1.

The surface contour measurement, shown in Fig. 2.3, is performed with a speckle interferometer set-up, as shown in Fig. 1.5. An argon-ion laser with etalon illuminates the reference and the measurement object. A standard CCD camera with CCIR norm records the speckle images, which are digitized into 8-bit digital images by a framegrabber. The measured area shown in Fig. 2.3 is 5 mm $\times$ 5 mm, and 512 $\times$ 512 pixels of the CCD camera are used. The surface height difference is 24 μm, if the gray scales change from black over different levels of gray to white. The object surface is tilted 144 μm relative to the even reference surface, and the elevation is approximately 50 μm. The reference surface is moved by a computer-controlled piezoelectric transducer to introduce a phase difference between the reference and the measurement beam to realize the temporal phase shifting. A high-voltage amplifier is used to produce a linear ramping signal to drive the piezoelectric transducer device and to perform a movement of $\lambda/8$ (wave-

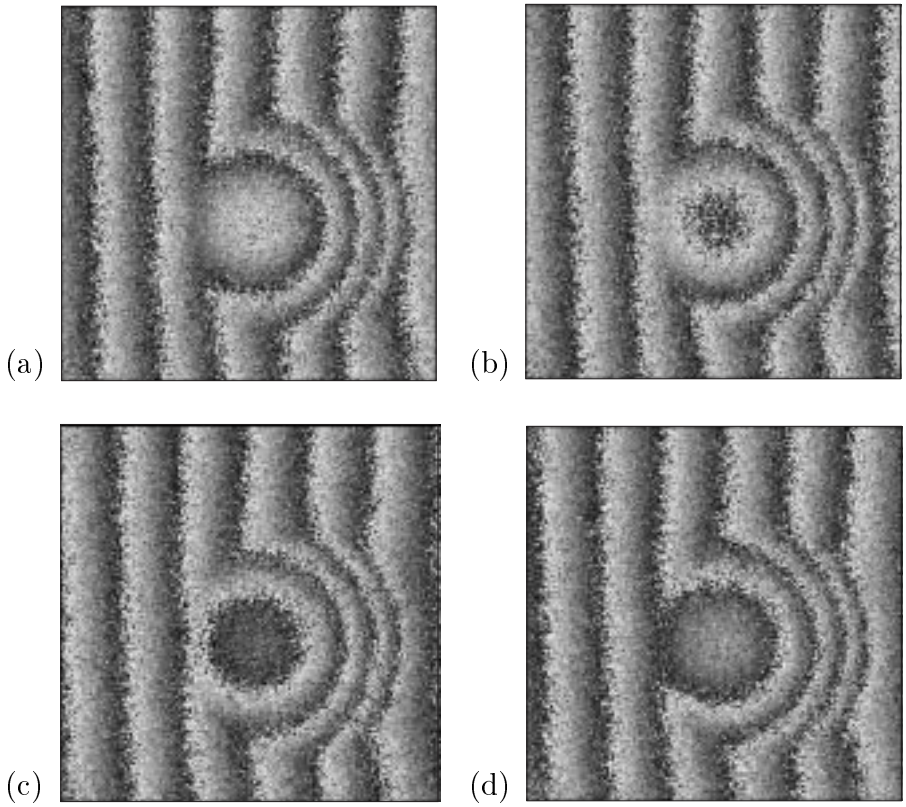

Figure 2.3: Phase-shifting images of a surface slope measurement with a bias phase step of $\pi/2$: (a) Φ_0, (b) Φ_{90}, (c) Φ_{180}, (d) Φ_{270}.

length λ of the illuminating laser beam) to realize a $\pi/2$ phase shift during the 40-ms integration time of the CCD camera.

To obtain the surface contour measurement shown in Fig. 2.3(a), four phase-shifted speckle images are recorded using the wavelength $\lambda_1 = 501.7$ nm, and four images using the wavelength $\lambda_2 = 496.5$ nm, with a resulting synthetic wavelength of 24 μm. The eight speckle images are taken to calculate the phase Φ_0 for any pixel (m, n) of the CCD camera with equation (1.89) by the Carré algorithm:

$$\begin{aligned}\Phi_0 &= \arctan \frac{h_1 g_2 - g_1 h_2}{g_1 g_2 + h_1 h_2} \\ &= \arctan \frac{g}{h}.\end{aligned} \tag{2.40}$$

The other three images are calculated according to

$$\Phi_{90} = \arctan \frac{h}{-g} \ , \tag{2.41}$$

$$\Phi_{180} = \arctan \frac{-g}{-h} \ , \tag{2.42}$$

and

$$\Phi_{270} = \arctan \frac{-h}{g} \ . \tag{2.43}$$

Four phase-shifting images are shown in Fig. 2.3, where the bias phase is stepped at $\pi/2$ (90°) intervals. When Φ_0 and Φ_{180} are subtracted, the result $\Phi_0 - \Phi_{180}$ will be a binary image, as shown in Fig. 2.4, with values of

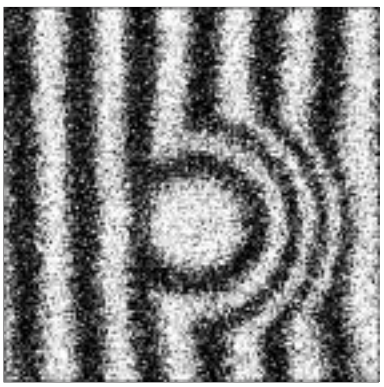

Figure 2.4: Binary image.

either $-\pi$ or $+\pi$. The binary image contains the same edges or changes from black to white, or vice versa, as do images Φ_0 and Φ_{180}. Because of the

arctan calculation the disturbances near the edges are much larger than the disturbances between two edges.

The unwrapping procedure is demonstrated one-dimensionally in Fig. 2.5. In Fig. 2.5(a) the correct unwrapping procedure is shown in the ideal case

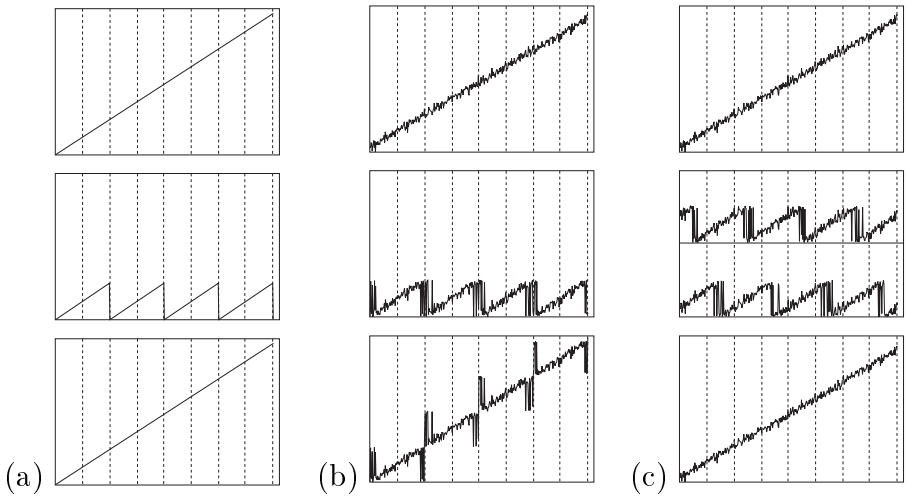

Figure 2.5: Unwrapping (a) without and (b) with disturbances, (c) selection of good data.

without noise, the original curve at the top, the wrapped curve in the middle, and the unwrapped curve without errors at the bottom. The original curve with low noise and the curve with disturbances near the edges caused by the arctan calculation, are shown in Fig. 2.5(b). Small errors near phase values of multiples of 2π cause larger errors near the edges in the wrapped as well as in the unwrapped phase. Figure 2.5(c) shows two original curves with a phase shift of π where the edges occur at different positions. The unwrapped curve without disturbances at the edges is obtained when the regions with good data are chosen from the two phase-shifted curves.

In the two-dimensional case it is possible to use good data from Φ_{90} and Φ_{270} in Fig 2.3, because the binary image in Fig. 2.4 identifies clearly the regions without disturbances. In black regions phase Φ_{90}, and in white regions phase Φ_{270} do not contain edges. First the boundaries of the black and white areas in Fig. 2.4 have to be found. Owing to the errors in the measured data, there are white pixels in black regions, and vice versa, which makes it difficult to identify the boundaries in a straightforward manner. Looking at the image, it is no problem to identify the different regions. One reason for this is that our brain analyzes images on different scales [120]; i.e. it averages over regions of different size. Since the error is on a smaller scale, black regions are identified as areas, which on average are black, because

there are more black pixels than white pixels, and vice versa. As Berger et al. demonstrated for the analysis of speckle deformation measurements with interference fringes, the wavelet transformation is an adequate tool for searching for structures in noisy speckle images [131], because it analyzes the data on different length scales. Here, the wavelet transformation has to fulfill two tasks. On the one hand, because of the presence of noise, it has to smooth the image, and on the other, it should be the gradient of the image, since structures therein are searched for.

As shown in [131], an appropriate two-dimensional wavelet for searching for structures in images is the first derivative of a two-dimensional Gaussian, given by equations (2.16) and (2.17)

$$\vec{\psi}_s\left(\vec{x},\vec{x}'\right) = \vec{\nabla}\varphi_s\left(\vec{x},\vec{x}'\right) = \vec{\nabla}\frac{1}{2\pi s}\exp\left(-\frac{1}{2}\left|\frac{\vec{x}-\vec{x}'}{s}\right|^2\right). \tag{2.44}$$

The two-dimensional wavelet transform $\vec{F}\left(s,\vec{x}'\right) = s\vec{\nabla}\left(f * \varphi_s\right)\left(\vec{x},\vec{x}'\right)$ of the image $f\left(x\right)$ is the gradient of the image smoothed by a Gaussian of width s. From the two components of the wavelet transform $F_1\left(s,\vec{x}'\right)$ and $F_2\left(s,\vec{x}'\right)$ the modulus

$$\left|\vec{F}\left(s,\vec{x}'\right)\right| = \left(\left[F_1\left(\vec{x}'\right)\right]^2 + \left[F_2\left(\vec{x}'\right)\right]^2\right)^{1/2} \tag{2.45}$$

of the gradient vector as well as its angle α are calculated with respect to the horizontal

$$\alpha\left(s,\vec{x}'\right) = \arctan\frac{F_2\left(s,\vec{x}'\right)}{F_1\left(s,\vec{x}'\right)}. \tag{2.46}$$

Using this information, it is possible to search for structures on different length scales. The edges in the image can be detected at the locations where the modulus has a maximum in the direction given by the gradient vector. This method does not depend on the complexity of the structures in the phase-shifting images. The only requirement is that the structures are on a different length scale than the noise. Hence, it is important to choose the appropriate length scale, i.e. the value of s, which determines the region over which the image will be smoothed. On the one hand, s has to be large enough for the noise to be smoothed. On the other hand, s must be small enough for the desired structure to remain; i.e. the distance between two consecutive edges has to be at least $2s$. In the example, the noise is nearly on the same scale as the speckle size, because the noise in the phase-shifting images depends on the speckle size. In Fig. 2.4 the distance between two consecutive edges is at least 30 pixels. The speckle size of the employed images is between 2 and 6 pixels, and the mean speckle size is 3 pixels. Thus, the length scale s is estimated to be larger than 3 and smaller than 15, and $s = 8$ is a suitable

choice. In addition, the modulus has to be large at the edges. Therefore pixels are identified as edges only if their modulus exceeds a given threshold. Small structures and single points disturb the result if this threshold is too small. Empirical studies have shown that a threshold value in the range of $15-25\%$ of the maximum value of the modulus is an optimal choice for this kind of measured data. Calculations for a wide variety of measured data of this kind corroborate an optimal threshold of 20%. The searched structures remain, and the noise is reduced. The corresponding edges are depicted in Fig. 2.6(d). Figure 2.6 shows the result for different length scales. If length

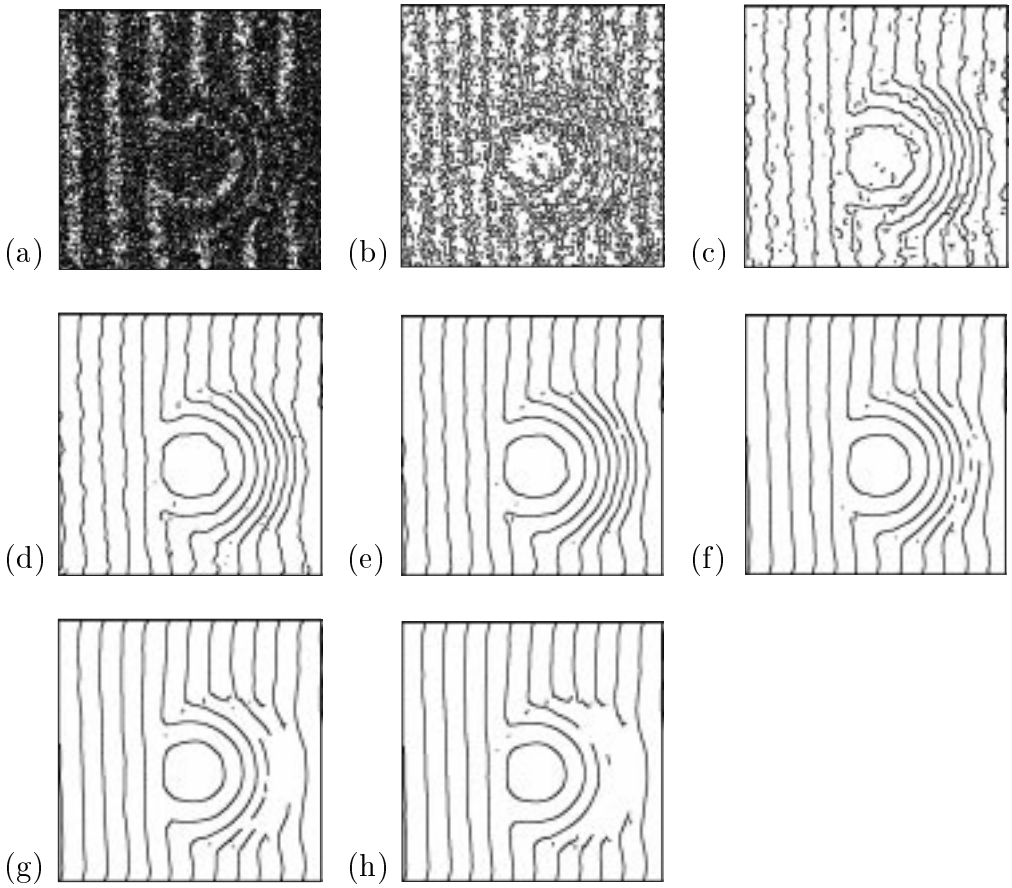

Figure 2.6: Edge detection with different length scales: (a) s=2, (b) s=4, (c) s=6, (d) s=8, (e) s=10, (f) s=12, (g) s=14, and (h) s=16.

scale s is too small, small structures will remain, as shown in Figs. 2.6(a) and (b). If s is too large, the desired structures will vanish, as shown in Figs. 2.6(g) and (h).

Using this method, it is possible to find lines which are boundaries be-

tween black and white regions in the binary image of Fig. 2.4. To identify the pixels in the image which belong to the same black or white region, it is necessary to have either closed lines or lines that begin and end at the border of the image. Furthermore, the lines must not cross one another. If this is the case, the regions can be clearly identified. With this information the edges from the wavelet analysis can be connected. The result is shown in Fig. 2.7.

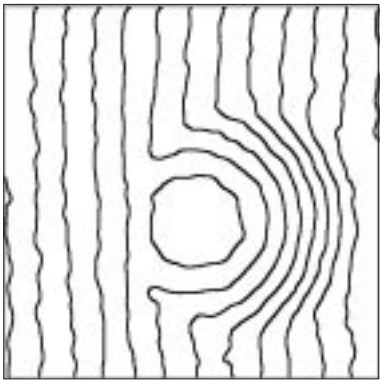

Figure 2.7: Closed lines of Fig. 2.6(d).

Now, the regions in the image and their colors can be identified. In black regions the data from ϕ_{90} are used, and in white regions the data from ϕ_{270}. The result is given in Fig. 2.8(a). There are still edges in the image, but the

(a) 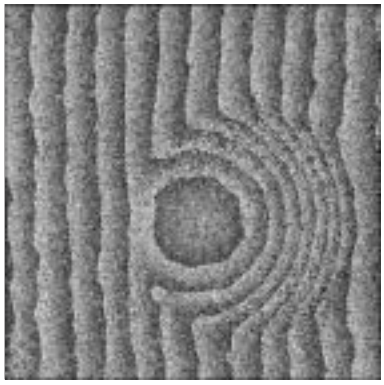 (b) 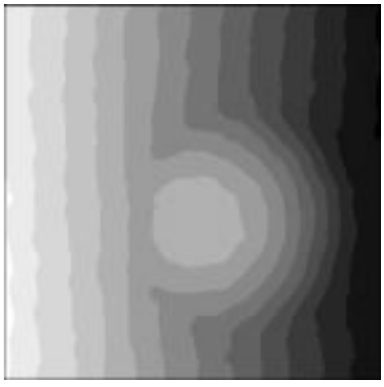

Figure 2.8: Wrapped image (a) by selection of good data and (b) the bias offset.

errors are much smaller than at the edges of a single phase-shifting image.

Now the unwrapping of this image is performed. Since the regions in the image are already identified, the only decision is either adding $+\pi$ or

$-\pi$ between neighboring regions. If the borderline between two regions is an edge in Φ_0, then $+\pi$ has to be added if there is a change from white to black, or $-\pi$ has to be added if there is a change from black to white. If the borderline between two regions is an edge in Φ_{180}, then $+\pi$ has to be added if there is a change from black to white, or $-\pi$ has to be added if there is a change from white to black. To decide if a borderline is an edge in Φ_0 or in Φ_{180}, the sample variance

$$\overline{\left[\Phi\left(\vec{x}\right)\right]^2} - \left[\overline{\Phi\left(\vec{x}\right)}\right]^2 \tag{2.47}$$

is calculated with

$$\overline{\Phi\left(\vec{x}\right)} = \frac{1}{n} \sum_{\vec{x} \in \text{line}} \Phi\left(\vec{x}\right) \tag{2.48}$$

along each line in both phase-shifting images. The edge is in the image with the larger variance value, since the error in the data is much larger in the edge region. Figure 2.8(b) shows the offset of the data, which is found from these considerations. Adding the data of Figs. 2.8(a) and 2.8(b) results in the unwrapped data shown in Fig. 2.9 and Fig. 2.10.

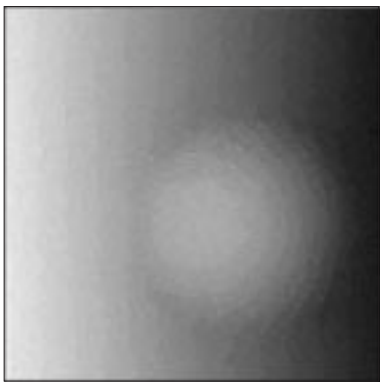

Figure 2.9: Unwrapped image of Fig. 2.8(a).

2.4 Spline reconstruction

Now the most probable surface should be reconstructed from the unwrapped image data. Bayes' theorem (2.23) states that the probability of a surface ρ, given the unwrapped image data D, is

$$p\left(\rho|D,K\right) \sim p\left(D|\rho,K\right) \cdot p\left(\rho|K\right), \tag{2.49}$$

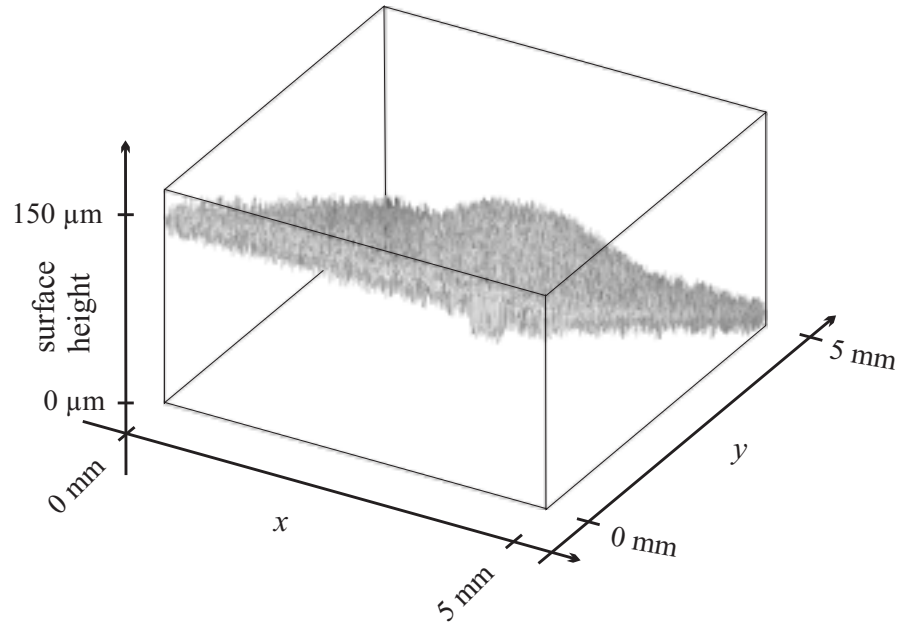

Figure 2.10: Unwrapped image of Fig. 2.8(a).

the maximum of which has to be found. From the nature of the problem, a two-dimensional spline is an appropriate representation for the surface model ρ.

To assign the prior probability $p(\rho|K)$ of the surface ρ, the maximum entropy principle [147] is used with the global curvature of the surface as relevant testable information, since a surface is expected, which is as smooth as possible. As Berger et al. demonstrated [131], an appropriate form of the prior probability for the reconstruction problem is given by

$$p(\rho|K) \sim \exp\left(-\frac{N}{2}\ln\Psi(\rho)\right), \tag{2.50}$$

where $N = (512)^2$ is the number of pixels of the image. The functional

$$\Psi(\rho) = \sum_{i,k}\left[\rho_{xx}^2(x_i, y_k) + \rho_{yy}^2(x_i, y_k) + 2\rho_{xy}^2(x_i, y_k)\right] \tag{2.51}$$

with the discrete derivatives

$$\rho_{xx}(x_i, y_k) = \frac{\partial\rho_{i,k}}{\partial x^2} = \rho_{i+1,k} - 2\rho_{i,k} + \rho_{i-1,k}, \tag{2.52}$$

$$\rho_{yy}(x_i, y_k) = \frac{\partial\rho_{i,k}}{\partial y^2} = \rho_{i,k+1} - 2\rho_{i,k} + \rho_{i,k-1}, \tag{2.53}$$

$$\rho_{xy}(x_i, y_k) = \frac{\partial \rho_{i,k}}{\partial x \partial y} = \frac{1}{4}\left(\rho_{i+1,k} - \rho_{i+1,k-1} - \rho_{i-1,k+1} + \rho_{i-1,k-1}\right), \qquad (2.54)$$

is a measure for the global curvature of ρ [153, 154].

The likelihood function is given by

$$p(D|\rho, K) \sim \exp\left(-\frac{N}{2}\ln\chi^2(\rho)\right), \qquad (2.55)$$

where

$$\chi^2(\rho) = \sum_{i,k}\left[D(x_i, y_k) - \rho(x_i, y_k)\right]^2 \qquad (2.56)$$

is the misfit between the data and the spline. Thus, it follows for the probability of ρ that

$$p(\rho|D, K) \sim \exp\left(-\frac{N}{2}\ln\Psi(\rho)\right)\exp\left(-\frac{N}{2}\ln\chi^2(\rho)\right), \qquad (2.57)$$

$$p(\rho|D, K) = F_1(\Psi(\rho))\, F_2\left(\chi^2(\rho)\right), \qquad (2.58)$$

the maximum of which has to be found. This equation describes the competition between the misfit of the data and the global curvature. A smaller misfit in general means a larger value of the global curvature, and vice versa. The optimal solution will be as complex as necessary, and will simultaneously fit the data as well as possible. The maximum of the posterior probability can be found by

$$\begin{aligned}\max_\rho\{p(\rho|D, K)\} &= \max_\rho\left\{F_1(\Psi(\rho)) \cdot F_2\left(\chi^2(\rho)\right)\right\} \\ &= \max_\eta\left\{F_2\left(\chi^2 = \eta\right) \cdot \max_\rho\left\{F_1(\Psi(\rho))|_{\chi^2=\eta}\right\}\right\}, \end{aligned} \qquad (2.59)$$

where a standard software tool can be used to find the corresponding spline [128]. The resulting spline ρ is depicted in Fig. 2.11.

The approach is not restricted to smooth surfaces, such as the one depicted in Fig. 2.11. To demonstrate this, a step in the surface is simulated by adding a fixed constant to a part of the unwrapped data, which is used as input data for the spline reconstruction, and the spline reconstruction is performed again. The result is given in Fig. 2.12. This shows that complicated structures even with discontinuities can be reconstructed, if the data give rise to complicated structures.

2.5 Discussion

A method has been developed, in which regions with good data from phase-shifting images with a bias phase step of $\pi/2$ are chosen, and bad data with

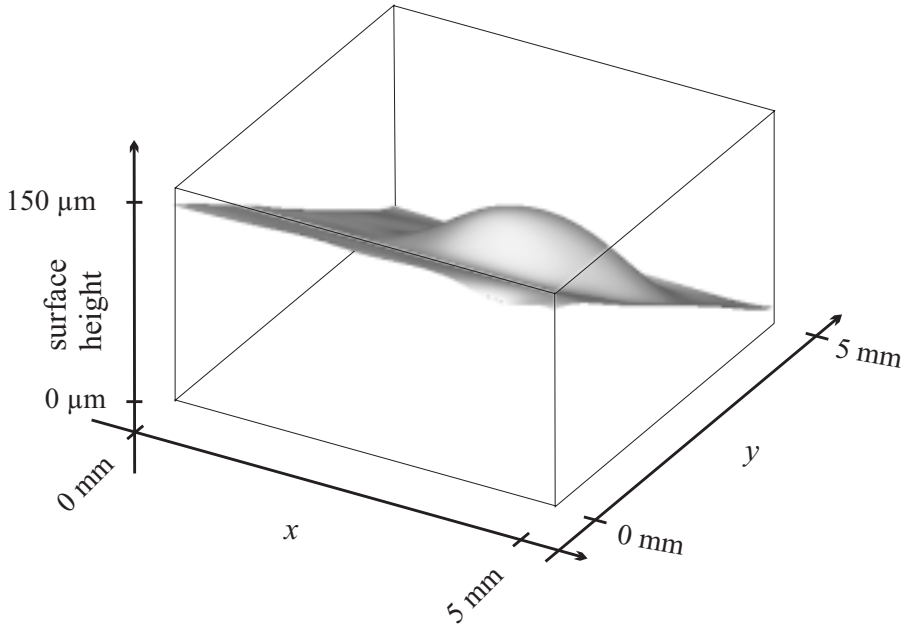

Figure 2.11: Spline reconstruction of the most probable surface of Fig. 2.10.

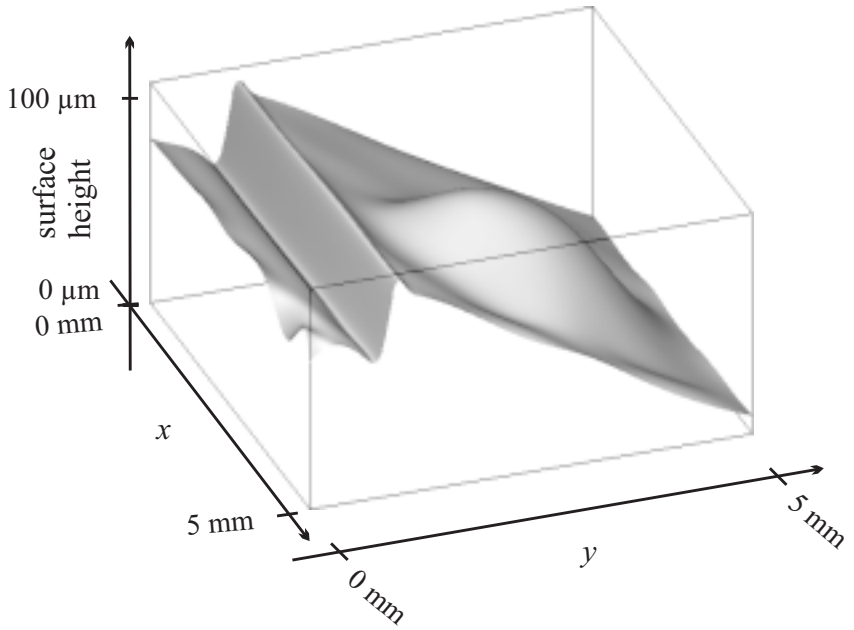

Figure 2.12: Spline reconstruction of the surface of Fig. 2.10 with a simulated step.

errors in the regions near the edges are not used. The errors caused by the arctan calculation in case of noisy input data are minimized, so that well-conditioned input data are used to reconstruct the measured surface three-dimensionally. The unwrapping performed with a wavelet transformation for edge detection does not depend on the complexity of the structures in the phase-shifting images. The only requirement is that the structures are on a different scale than the noise. In the example the noise is approximately on length scale 3, and the smallest structures are on length scale 15. The Bayesian probability theory is used to find the most probable surface to the unwrapped data. The optimal solution of a three-dimensional spline will be as complex as necessary and simultaneously fit the data as well as necessary. As has been shown, this method, used in phase-shifting speckle interferometry, is applicable to surface slope measurements as well as to deformation measurements.

Chapter 3

Detection of surface microrelief changes

In experimental fusion devices plasma-facing components, such as graphite tiles in the divertor region, are eroded, and the erosion may be compensated by local redepositions of eroded material. Since the amount of eroded material influences the characteristics of the plasma and the lifetimes of plasma-facing components, it is of interest to detect eroded surface areas and to determine the amount of erosion or redeposition.

3.1 Holographic interferometry

The dependence of fringe contrast of interference fringes on changes in the surface microrelief was first investigated in holographic interferometry, before it was examined in speckle interferometry. In case of holographic interferometry, the change in the surface microrelief between two exposures results in decorrelation of the reconstructed light waves, and thus the fringe contrast is reduced. An overview of the measurement of erosion rates due to chemical erosion and mechanical wear is given in [155]. The laser-induced erosion rate for an aluminum surface is determined in [156].

An analytical equation connecting the fringe contrast C_f with an average displacement $\langle \Delta r \rangle$ of a surface point has been derived in [157] for the case of chemical erosion of a metallic surface:

$$\langle \Delta r \rangle = \frac{\lambda}{2\pi \cos \alpha} \left(\frac{1}{C_f} - 1 \right)^{1/2}, \tag{3.1}$$

where the angular brackets denote the ensemble average, λ is the wavelength of the illuminating laser light, α is the angle between the surface normal and

the illumination direction, and Δr is the normal component of the displacement vector. The illumination and viewing directions have opposite angles α to the surface normal, and therefore the interferometer is out-of-plane sensitive. It is assumed that the random nature of the change in the surface microrelief only affects the phase of the reflected wave, thus the reflecting properties of the surface remain unchanged, and that the probability density function $f(\Delta r)$ is a Gaussian function. Hence, the mean displacement $\langle \Delta r \rangle$ can be derived by [157]

$$\langle \Delta r \rangle = \frac{\lambda}{2\pi \cos \alpha} \tan \frac{\Delta \phi}{2}, \tag{3.2}$$

where $\Delta\phi$ is the phase change due to the microrelief change. The random change of the surface microrelief results in a decrease of the fringe contrast and in an additional phase shift which changes the geometry of the fringes.

However, between zero and a certain maximum amount of erosion, i.e. a maximum surface height change, the fringe contrast change provides the quantitative information on the removed or added surface height. Because of the necessary contrast measurement the spatial resolution depends on the fringe spacing.

The phase-shifting method provides both the visibility γ and the additional phase shift $\Delta\phi$, e.g. with equations (1.77) and (1.79) [158]. The information on the surface microrelief change is given by equations (3.1) and (3.2), when the fringe contrast C_f is replaced by the visibility γ. The phase-shifting method is of advantage because of its high spatial resolution due to the calculation for each pixel and because there is no need for interference fringe formation.

3.2 Speckle interferometry

The determination of the phase shift and the fringe contrast depending on the surface microrelief change is based on a sinusoidal modulated intensity, as, for instance, in equations (1.44) and (1.45) for speckle interferometry. Hence, equations (3.1) and (3.2) can be applied for out-of-plane sensitive speckle interferometers. However, it has to be taken into account that the maximum of the fringe contrast is assumed to be unity.

The relation between the decorrelation in speckle interferometry and the surface microrelief changes is derived by Gülker [159, 160] by means of correlation coefficients. The dependence of intensities I_{a1} after, and I_{b1} before a phase change $\Delta\phi$, on the correlation coefficient C_t for any pixel, is given by

$$\left(\left\langle (I_{a1} - I_{b1})^2 \right\rangle\right)^{1/2} = \left\{ 2 \langle I_o \rangle^2 \left(1 - |C_t|^2\right) + 4 \langle I_o \rangle \langle I_r \rangle \right.$$

$$-4\left\langle I_o\right\rangle \left\langle I_r\right\rangle \left|C_t\right| \cos\Delta\phi\Big\}^{1/2}, \tag{3.3}$$

where I_o and I_r are the intensities of the measurement and the reference beams. It is assumed that the phase change only affects the measurement beam, and that the ensemble averaged intensities of both the measurement beam and the reference beam are not affected by the phase change. The correlation coefficient C_t

$$C_t = C_c C_d \tag{3.4}$$

contains the decorrelations C_c due to surface microrelief changes and other decorrelations C_d caused by the movement of the measurement object, e.g. rotation, in-plane motion, or large out-of-plane movements. The correlation coefficient C_t is directly related to surface microrelief changes when $C_d = 1$.

Equation (3.3) may be expressed as

$$\left(\left\langle \left(I_{a1} - I_{b1}\right)^2\right\rangle\right)^{1/2} = \left\{I'^2_0 \left(1 - \gamma' cos\Delta\phi\right)\right\}^{1/2}. \tag{3.5}$$

A decreasing correlation coefficient leads to a decreasing fringe contrast and to a decreasing visibility γ', but the dependence of the fringe contrast on the correlation coefficient C_t is too complicated to determine a direct relation to surface microrelief changes.

To separate the correlation coefficient C_t, the visibility γ' may be derived by the phase-shifting method, according to equation (1.79), from four phase-shifted squared intensities

$$\begin{aligned} I_i^2 =& \left(\left\langle \left(I_{ai} - I_{b1}\right)^2\right\rangle\right)^{1/2} \\ =& I'^2_0 \left(1 - \gamma' cos\left[\Delta\phi + \beta_i\right]\right), \end{aligned} \tag{3.6}$$

with $i = 1 \ldots 4$ and $\beta_i = (i-1)\,\pi/2$. Since the correlation coefficient $|C_t|$ depends on the mean reference intensity $\langle I_r\rangle$, a smooth reference beam should be used, i.e. a constant mean reference intensity. The influence of the dependence on the unknown mean object beam intensity $\langle I_o\rangle$ may be reduced when initial values of the correlation coefficient C_t are determined without decorrelation, and the correlation coefficients are normalized to the initial values to measure the surface microrelief changes. The ensemble averages are replaced by the spatial means of small subareas of the images, and thus the spatial resolution is reduced. This method has been used to measure water-induced changes at surfaces of natural stones [160] and can be applied to detect any surface microrelief changes.

3.3 Simulation

The analytical derivation of the dependence of the fringe contrast or the phase change on surface microrelief changes is feasible for simple probability density functions $f(\Delta r)$ for the normal component of the surface displacement vector, e.g. for a Gaussian distribution or an equal-probability distribution. The simulation method based on ray tracing, described in [49, 50, 51], makes it possible to determine the dependence of various parameters of the speckle measurement techniques on any given surface microrelief and any surface microrelief change. The fringes shown in Fig. 3.1 are simulated as-

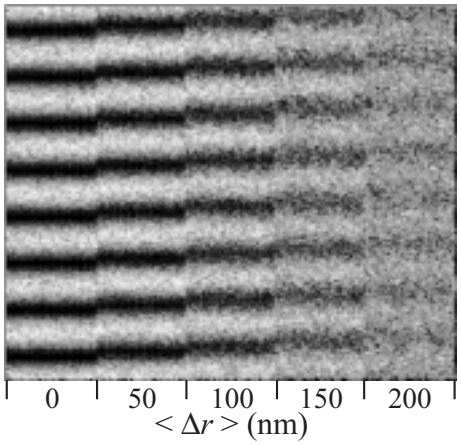

Figure 3.1: Simulation of the fringe contrast.

suming a wavelength of $\lambda = 488$ nm, and a speckle interferometer set-up with equal, but opposite, illumination and observation angles $\alpha = \pm\pi/4$, where the fringes are introduced by tilting the measurement object. The image is divided into five vertically separated subareas (vertical stripes), which have different fringe contrasts caused by different erosion depths, i.e. different mean average displacements of surface points of the measurement object. The surface height distribution is an equal-probability distribution with surface heights r between 0 nm and r_2 before, and between 0 nm and r_1 after a surface microstructure change. Thus, the mean erosion depth, i.e. $\langle \Delta r \rangle$, is given by $0.5\,(r_2 - r_1)$ and gives rise to an additional phase change causing the slight movement of the interference fringes. The fringe contrast change depends on the change of the surface height distribution and decreases until a minimum value is reached (solid line of Fig. 3.2). This behavior should be investigated further for other surface height distributions. The dashed line of Fig. 3.2 shows the characteristic of equation (3.1) for $\lambda = 488$ nm and $\alpha = 0$ rad. Since the dependence of the fringe contrast C_f on the average

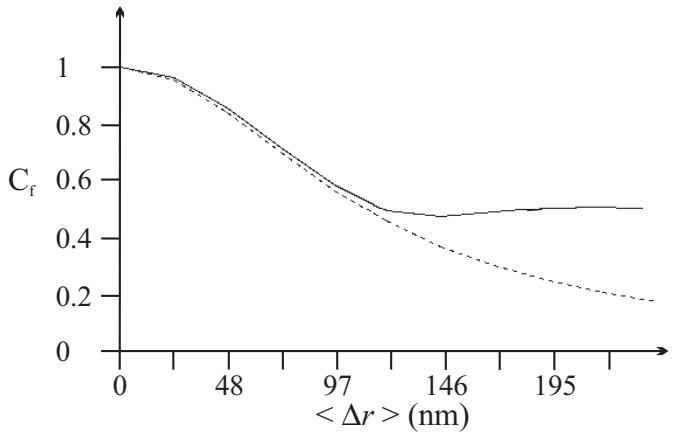

Figure 3.2: Comparison of simulation (solid) and analytical derivation (dashed).

erosion depth $\langle \Delta r \rangle$ exhibits a nonlinear behavior, small microrelief changes of the order of 20 nm lead to a noticeable decrease of the fringe contrast.

Since the fringe contrast depends on the change in the surface height distribution, knowledge on the distribution is needed to determine the erosion depth. Often a Gaussian distribution is assumed in the case of optically rough surfaces, but the knowledge on the influence of surface microrelief changes on parameters, such as fringe contrast or visibility in speckle interferometry, should be improved for several surface height distributions. The surface microrelief could be measured before and after a surface microrelief change with a measuring system which measures large surface areas with a high resolution, e.g. the MicroGlider of FRT GmbH [161], which measures surface heights of up to 3 mm with a vertical resolution of 50 nm and a lateral resolution of 100 nm of a measurement area of up to 30 mm $\times$ 30 mm. The measured surface heights could be used in the simulation program, and thus the comparison between simulation and speckle measurements results would improve the knowledge on the influence of surface microrelief changes.

3.4 Measurement results

The measurement results of Figs. 3.3 and 3.4 verify the detectability of surface microrelief changes using speckle interferometry methods. The measurements are performed with an out-of-plane sensitive interferometer set-up, as shown in Fig. 1.5, which is based on the Michelson interferometer set-up. The reference object is of the same material as the measurement object and

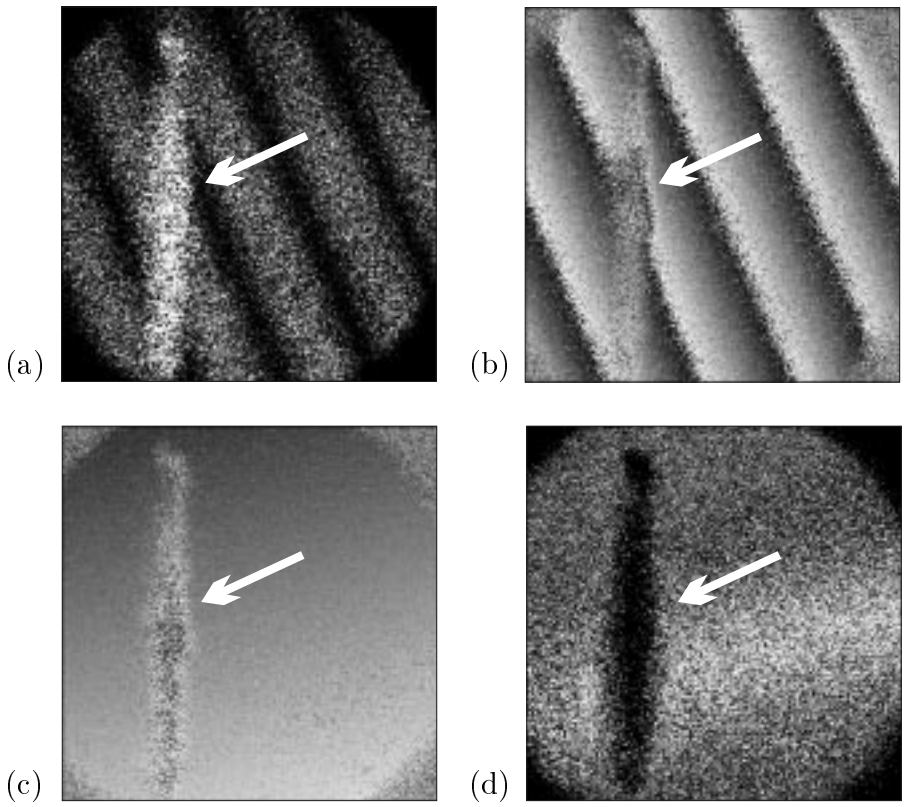

Figure 3.3: Surface microrelief change: (a) fringe pattern, (b) and (c) phase-shifting images, and (d) visibility.

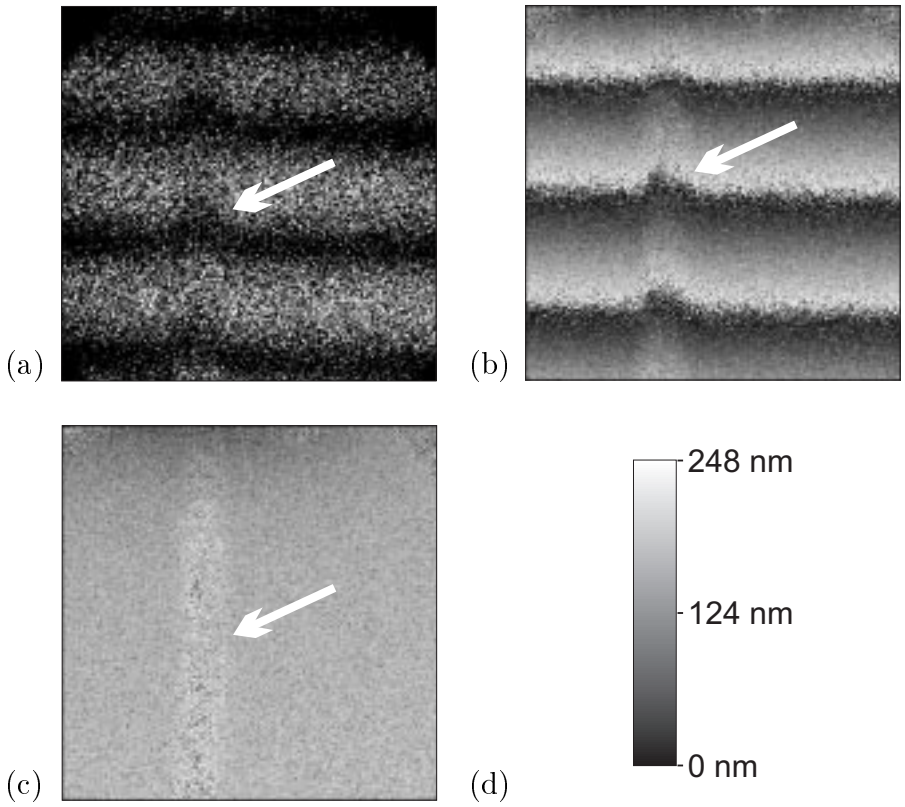

Figure 3.4: Surface microrelief change: (a) fringe pattern, (b) and (c) phase-shifting images, and (d) gray scales of the phase-shifting images.

is translated by piezoelectric transducers during the integration time of the CCD camera to introduce phase shifts of $\pi/2$ between two speckle images. Four phase-shifted speckle images are required before and after the surface microrelief change is introduced, and after an additional tilt of the measurement object, respectively. The phase modulo 2π is calculated by the Carré algorithm and by equation (1.89). The visibility is calculated by equation (1.79) using four phase-shifted fringe patterns, which are calculated by subtracting phase-shifted speckle images after the surface microrelief change from a speckle image before the change. The images correspond to a measured area of 14 mm $\times$ 14 mm at a measurement distance between measurement object and lens system of 320 mm. The wavelength of 496.5 nm of the used argon laser corresponds to a fringe spacing of $\lambda/2 \approx 250$ nm. The gray scales of Fig. 3.4(d) are used to visualize the phase values.

Graphite tiles are employed as measurement and reference objects, and the surface microstructure changes of the measurement object are caused by electrical arc erosion. The erosion shown in Fig. 3.3 is stronger than that of Fig. 3.4 since the fringes in Fig. 3.3(a) are interrupted, and those of Fig. 3.4(a) are only slightly curved. The phase-shifting images of the erosions are shown in Figs. 3.3(c) and 3.4(c), and those of the erosions together with an additional tilt of the measurement object are shown in Figs. 3.3(b) and 3.4(b). The erosion can be clearly detected in Fig. 3.3(d), where the visibility is reduced in the erosive area, since both the surface microrelief and the reflection properties of the surface have changed. The erosion shown in Fig. 3.4 changes the phase no more than approximately one fourth of the fringe spacing, i.e. $\pi/2$. This corresponds to a maximum erosion depth of 80 nm, when a Gaussian surface height distribution is assumed and equation (3.2) is used. Since the erosion, shown in Fig. 3.3, interrupts the fringes, and is detected as strong perturbation in the phase-shifting images, respectively, the erosion depth is larger than the amount which changes the phase 2π, i.e. 240 nm.

The detection of erosive areas may also be performed by measuring the surface contour with two differing wavelengths of the employed laser light. The chemical erosion of an aluminum surface, as shown in Fig. 3.5, is caused by hydrochloric acid. The synthetic wavelength of $\Lambda = 24$ μm is obtained using the wavelengths $\lambda_1 = 496.5$ nm and $\lambda_2 = 501.7$ nm, and an angle of $\alpha = 0°$. The plane reference surface is nearly perfectly aligned to the plane measured surface, so that the phase-shifting image of the surface contour measurement consists of only a few gray scales. Since the surface microrelief changes cause perturbations in the phase, and thus in the gray scales, the erosive areas can be detected clearly, as shown in Fig. 3.5.

The measurement results demonstrate that surface microrelief changes

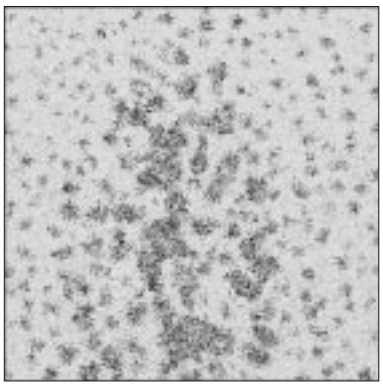

Figure 3.5: Surface contour measurement with surface microrelief changes caused by hydrochloric acid.

can be detected by speckle interferometry. When the average surface height change $\langle \Delta r \rangle$, e.g. caused by erosion or redeposition, is less than the maximum value causing a phase change of 2π, $\langle \Delta r \rangle$ may be determined with additional knowledge on the surface height distribution and its change.

Chapter 4

Four-camera interferometer

The temporal phase-shifting methods described in section 1.3 cannot be applied in noisy environment, and the spatial carrier methods described in section 1.4.2 reduce the lateral resolution of the measurement. The multi-camera approaches of the spatial phase-stepping method, described in section 1.4.1, allow measurements even if the measurement object is not vibration isolated. However, these methods are restricted to the use of only one wavelength of laser light.

The interferometer set-up which allows measurements with two differing wavelengths and with a high lateral resolution, is a multi-camera interferometer with at least three reference beams, each one containing a piezo-based phase shifter. In this chapter, the four-camera interferometer set-up and first measurement results are described [162].

4.1 Set-up

At least three phase-shifted interferograms are required to determine the phase. Using phase algorithms based on four phase-shifted interferograms gives the advantage of being insensitive to phase shift errors. Thus, a set-up with four cameras is chosen, which allows simultaneous acquisition of four phase-stepped interferograms. The set-up of the four-camera interferometer, which is a phase-stepping speckle interferometer, is shown in Fig. 4.1.

First measurements were performed with a multifrequency argon laser with an etalon, a fiber coupling, and a coherence length greater than 10 m. The output power of the polarization-preserving, single-mode fiber is up to 800 mW for wavelength 514 nm. Further measurements with a measurement object, which is not vibration isolated, may be performed with a frequency-doubled Nd:YAG pulsed laser with a pulse energy of up to 500 mJ, a pulse

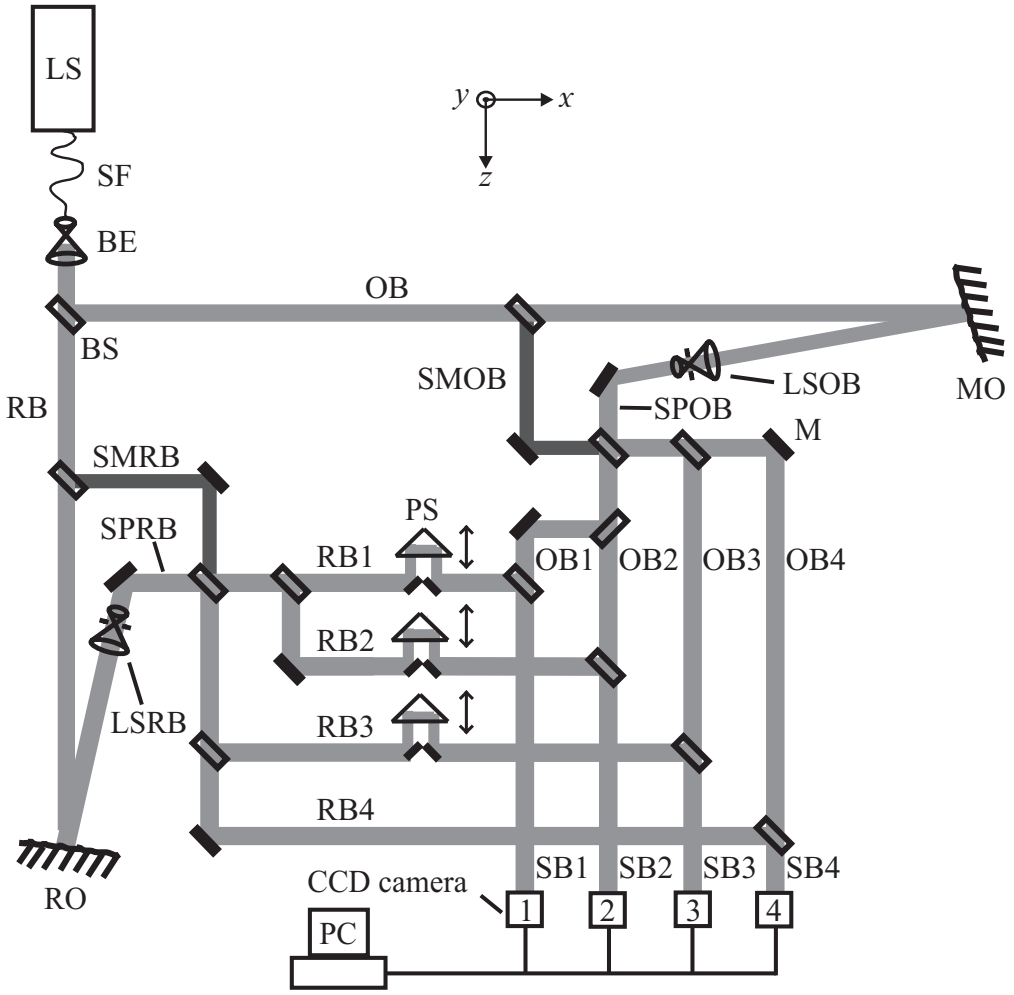

Figure 4.1: Four-camera interferometer set-up. BE: beam expander, BS: beam splitter, LS: laser, M: mirror, MO: measurement object, OB: object beam, LSOB: lens system of the object beam, LSRB: lens system of the reference beam, PC: personal computer, PS: phase shifter, RB: reference beam, RO: reference object, SB: superimposed beam, SF: single-mode fiber, SMOB: smooth object beam, SMRB: smooth reference beam, SPOB: speckled object beam, SPRB: speckled reference beam.

duration of 5 ns, a coherence length of about 0.2 m, a repetition rate of 10 Hz, and a wavelength of 532 nm. Another wavelength may be chosen with an additional optical parametrical oscillator system [49].

The four CCD cameras are progressive scan cameras with a 1/2" interline-transfer-type CCD sensor with 782 × 582 square-shaped pixels of the size of 8.3 μm × 8.3 μm, a chip size of 8.1 mm × 6.33 mm, and an electronic shutter with an exposure time of 0.1 ms up to 40 ms. The gain of each CCD camera may be set manually to equalize the different behaviors of the CCD cameras. The cameras are synchronized by an external pixel clock signal generated by the frame grabber. Thus, four images may be acquired simultaneously, digitized to 8 bits and transferred to the RAM memory of the personal computer with an image frequency of 25 Hz. The progressive scan CCD cameras produce a full frame output in the shutter mode, even if a pulsed laser is used.

Each phase shifter of the reference beams consists of a piezoelectrically movable linear translation stage with two 90°-prisms. The closed-loop positioning system with low-voltage piezoelectrical translators and LVDT (linear variable differential transformer) sensors allow computer-controlled movement of the prisms with a resolution of better than 10 nm. In order to reduce reflections which could influence the measurement, prisms and beam splitters are coated with thin films which reduce reflections below 0.3 %.

In principle, the four-camera interferometer set-up, shown in Fig. 4.1, consists of four parallel interferometers based on the Mach-Zehnder interferometer. The first beam splitter divides the laser light into object beam OB and reference beam RB. The light reflected by the measurement object passes through the lens system LSOB and is split by three beam splitters into the beams OB1, OB2, OB3, and OB4 with equal intensities. The measurement object is imaged by the lens system in the image planes onto the sensors of the CCD cameras. The smooth object beam SMOB is used to align the complex interferometer. This interferometer set-up has both a smooth reference and a speckled reference beam, where the reference object is imaged by the lens system LSRB in the image planes onto the sensors of the CCD cameras. The reference beam is divided by three beam splitters into the beams RB1, RB2, RB3, and RB4 with equal intensities. The piezoelectrically movable prisms, i.e. the phase shifters, introduce path differences between the reference paths. The reference beams RB1 to RB4 and the measurement beams MB1 to MB4 superimpose to form the beams SB1 to SB4. This interferometer has to be aligned, so that the CCD cameras will record identical object areas. The path length differences between reference beams and measurement beams have to be smaller than the coherence length of the used laser light. The path length differences between measurement beams MB1 to MB4 have to

be smaller than the length of a speckle.

4.2 Alignment

The smooth reference and the smooth object beams are used to align the interferometer with the occurring interference fringes. All beams should have nearly the same height, i.e. equal distances between the vibration-isolated table and the beams. Mechanical alignment components are chosen. The xz-plane of the beam splitters may be adjusted with a sensitivity of 10^{-4} rad, and the rotation around the y-axis of the beam splitters with a sensitivity of 10^{-3} rad, the xy-plane of the mirrors with a sensitivity of 10^{-5} rad, the xz-plane and the rotation around the y-axis of the lens systems, the prisms and the CCD cameras, with a sensitivity of 10^{-3} rad.

Figure 4.1 shows the basic set-up of the four-camera interferometer, where the path lengths of the measurement and the reference beams are not equal. For the used set-up all beams between the first beam splitter and the CCD cameras have almost equal path lengths. The allowable differences of the path lengths depend on the coherence length of the employed laser light. The interferometer may easily be aligned with path differences of a few millimeters. The set-up which has been carried out is shown in Fig. 4.2. The speckled reference beam is not implemented, and the smooth reference beam is generated by a beam splitter and a mirror.

After the alignment of all beam splitters, mirrors and prisms, four interference fringe patterns are observed at the positions of the CCD cameras when, for instance, the first beam splitter is just slightly rotated around the y-axis. The path length differences between the reference beams, introduced by the phase shifters, cause differences in the interference fringe patterns. When a phase shifter is translated by Δz_i, the path length is changed by $2\Delta z_i$, and the phase shift is given by

$$\beta_i = \frac{4\pi}{\lambda}\Delta z_i. \tag{4.1}$$

Since the measured intensities are sinusoidal functions of the path differences, relative phase shifts between the interference fringe patterns are introduced by phase shifters. These phase shifters may be adjusted such that four identical interference fringe patterns are obtained when all components after the first beam splitter are precisely aligned.

In order to generate four identical interference fringe patterns, perfect optical components are required. However, the optical components can only be fabricated within a finite precision and therefore each optical component

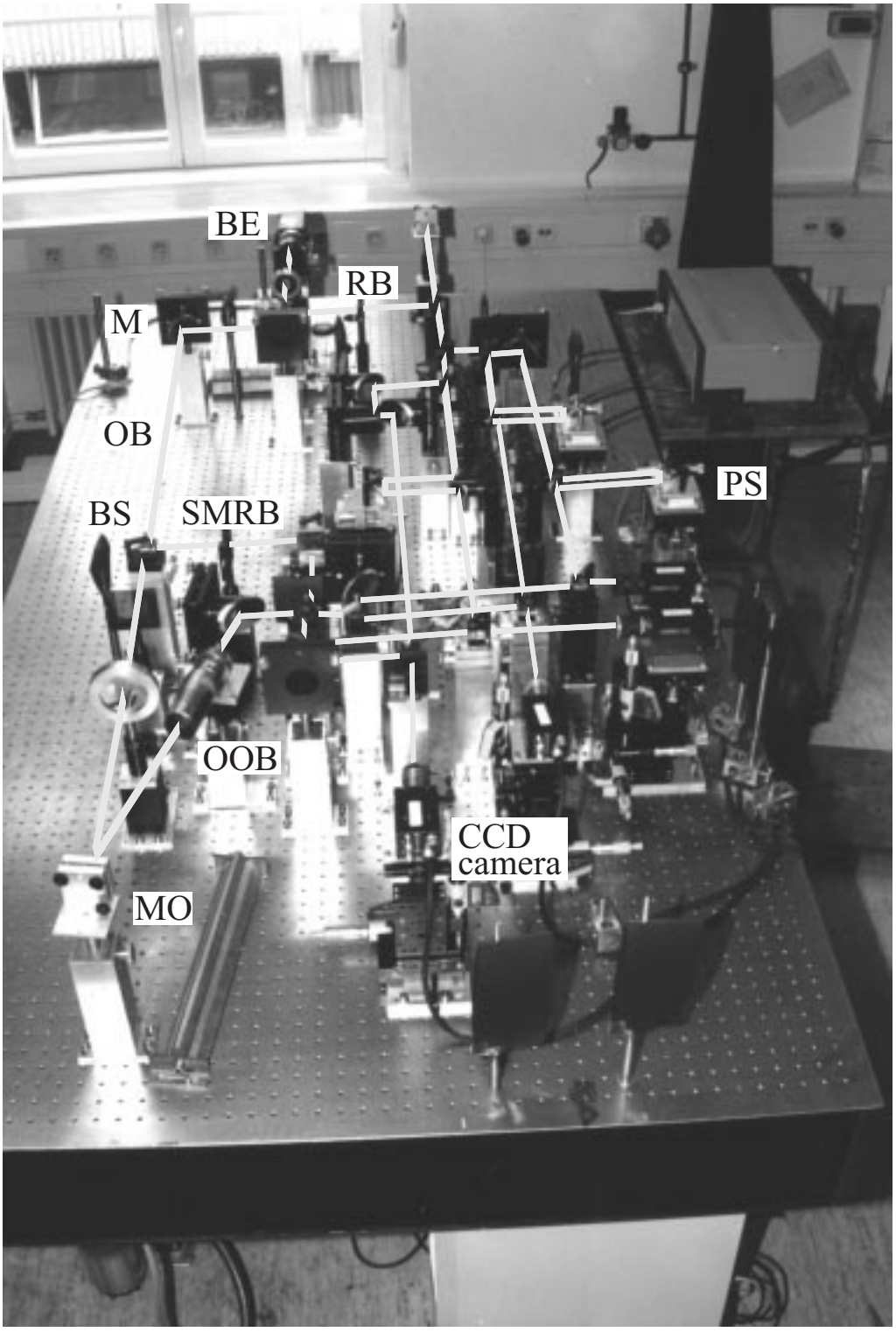

Figure 4.2: Realization of a four-camera interferometer set-up. BE: beam expander, BS: beam splitter, M: mirror, MO: measurement object, OB: object beam, LSOB: lens system of the object beam, PS: phase shifter, RB: reference beam, SMOB: smooth object beam, SMRB: smooth reference beam.

will introduce an error. The four interference fringe patterns will be different even if all optical components are precisely aligned, because the object and the reference beams propagate through different beam splitters, and are reflected by different mirrors, and because three reference beams propagate through different prisms. The deviation between any employed mirror and a perfect plane mirror is less than 80 nm at any point of the mirror. The deviation between any beam splitter or prism and a perfect plane surface is less than 400 nm. Since the height difference between two adjacent fringes of this out-of-plane sensitive interferometer is $\lambda/2$, differences in the interference fringe patterns are expected.

When all optical components are precisely aligned, using the smooth reference and smooth object beams, the CCD cameras have to be aligned. Firstly, a transparent measurement object with small non-transparent structures is back-illuminated by a non-monochromatic light source. The lens system LSOB and CCD camera 4 have to be positioned to image the structures onto the sensor of CCD camera 4. Then, the other three CCD cameras are focused by shifting the cameras along their z-axes. After this coarse alignment, the transparent object is replaced by a reflecting, optical rough measurement object, which is illuminated by laser light. The CCD cameras have to be aligned, so that they record identical object areas. Since the correlation between the recorded speckle patterns is mainly dependent on the mutual displacement of the CCD cameras along the x- and the y-axes, the camera positions can also be shifted in the x- and the y-directions with a sensitivity of 1 μm, and can additionally be shifted along the z-axis with a sensitivity of 5 μm. The CCD cameras may be positioned by inspecting the recorded speckle patterns visually. The correlation coefficient C_{12} of equation (1.13) is applied to determine the correlation between two speckle patterns. The ensemble averages are replaced by averages across the image planes, i.e. across the speckle patterns, which means, it is assumed that the recorded speckle patterns satisfy the ergodic property. Using the visual inspection of speckle images, correlation coefficients C_{12} up to 0.85 are obtained.

To perform the final alignment of the CCD cameras, the correlation coefficients between the speckle images of the various CCD cameras are calculated on-line and displayed on the monitor of the PC. Besides the correlation coefficients between two speckle images of several subareas, together with the displacement vectors, can be displayed on-line to align the CCD cameras correctly. Using this method, correlation coefficients greater than 0.9 can be obtained when the speckle sizes are greater than at least two pixels. Since the optical components and the CCD cameras are not perfect, the maximum correlation coefficient of unity will not be obtained, but a correlation coefficient of 0.97 between two CCD cameras could be obtained with a mean

speckle size of 7 pixels, i.e. about 60 μm. Using this technique, the cameras are mutually aligned within an estimated accuracy of better than 2 μm, 3 μm, and 50 μm along the x-, y-, and z-axes, respectively.

When the speckled object beam and the smooth reference beam superimpose to form a speckle pattern, a smooth reference beam speckle interferometer is realized. Measurements have shown that the relative phase shift between two corresponding pixels depends on the position of the considered pixel. In the center of the sensor areas, the mutual displacement between two corresponding pixels remains small. However, for pixels at the edges of the CCD sensor areas, the relative shifts between corresponding pixels become significant. Both the temporal phase-stepping method for each of the three parallel interferometers which contain a phase shifter in the reference beam, and the spatial phase-stepping method may be applied when the measurement object is placed on the vibration-isolated table together with the interferometer set-up. The maximum of the correlation coefficient between two speckle images of two different CCD cameras is reduced since the optical components are not perfect. The differences of the paths which contain a phase shifter may be determined. The larger the differences of the beams, the smaller are the maxima of the correlation coefficients. The phase shift between two speckle images of two different CCD cameras is determined by equation (1.91), when the range of values $[C_{12min}, C_{12max}]$ is transformed in the range of values $[0, 1]$, where C_{12min} is the minimum, and C_{12max} the maximum of the correlation coefficient.

The speckle interferometer set-up with a speckled reference beam is obtained when both the speckled object beam and the speckled reference beam are used. The alignment of this interferometer set-up is more complicated, but may be performed using on-line correlation coefficients and displacement vectors. After the alignment of the CCD cameras using the measurement object, the mirrors and the beam splitters of the reference paths have to be aligned until the correlation coefficients between the different speckle images are maximized.

4.3 Measurement results

The measured intensity of a pixel (m, n) of the CCD camera i is given by equation (1.70) and may be expressed as

$$I(m,n,i) = I_0(m,n,i)\left(1 + \gamma(m,n,i)\cos\left[\Phi(m,n,i) + \beta(m,n,i)\right]\right), \quad (4.2)$$

with $i \in [1, 4]$. The temporal phase-stepping method is introduced by

$$\beta(m,n,i) = k\beta_1(m,n), \quad (4.3)$$

with equal phase shifts $\beta_1(m,n)$ between N measured intensities of the parallel interferometers which contain a phase shifter, i.e. $i \in [1,3]$ and $k \in [1,N]$. The spatial phase-stepping method is obtained with

$$\beta(m,n,i) = i\beta_1(m,n), \tag{4.4}$$

when equal phase shifts $\beta_1(m,n)$ between the measured intensities of the different CCD cameras are assumed. The phase $\phi(m,n) = \phi(m,n,i)$ may be determined by the standard algorithms of section 1.3.1, when $I_0(m,n,i)$, $\gamma(m,n,i)$, and $\phi(m,n,i)$ are independent of $i \in [1,4]$.

Figure 4.2 shows the realized four-camera interferometer set-up. The vibration-isolated table has the dimensions 2.4 m $\times$ 1.2 m, the lens system has a focal distance of 150 mm, the measuring distance between measurement object and lens system is 260 mm, the distance between lens system and image planes of the CCD cameras is 710 mm. The measured area of the measurement object is about 1.7 mm $\times$ 1.7 mm when 512 $\times$ 512 pixels of the CCD cameras are used. Thus, the imaging system has a magnification of about 3.3. The measurement object has an aluminum surface.

Figure 4.3 shows a result of this four-camera interferometer when the smooth reference and smooth object beams are used and an argon laser with the wavelength of 514 nm is employed. Figures 4.3(a) to (d) are four temporal phase-stepped interferograms with a phase shift of about $\pi/2$, and are acquired with CCD camera 1 by applying the temporal phase-stepping method. The phase shifter has to be translated by $\lambda/8 \approx 64$ nm to introduce a phase shift of $\pi/2$. The tilt is introduced by rotating the first beam splitter around the y-axis and the interference fringes map out the differences between the reference beams and the object beams as contours of $\lambda/2 = 257$ nm. The resulting phase-stepping image, calculated with the Carré algorithm, is shown in Fig. 4.3(e). Figures 4.3(f) to (i) are four phase-stepped interferograms of four different CCD cameras. Since the optical components and the alignment of the interferometer set-up are not perfect, several interference fringes are not oriented vertically, e.g. those of Fig. 4.3(g). The number of interference fringes of Figs. 4.3(f) and (g) is different from that of Figs. 4.3(h) and (i). Hence, the interferometer set-up is not perfectly aligned. Nevertheless, the resulting phase-stepping image shown in Fig. 4.3(j), is of good quality. With these interference fringe patterns the complex interferometer set-up can be aligned, and the amounts of phase shift between the parallel interferometers may be verified.

The speckle image of CCD camera 4 with a mean speckle size of about 7 pixels, obtained by the four-camera set-up with a smooth reference beam, is shown in Fig. 4.4. Both measurement and reference beam contain neutral

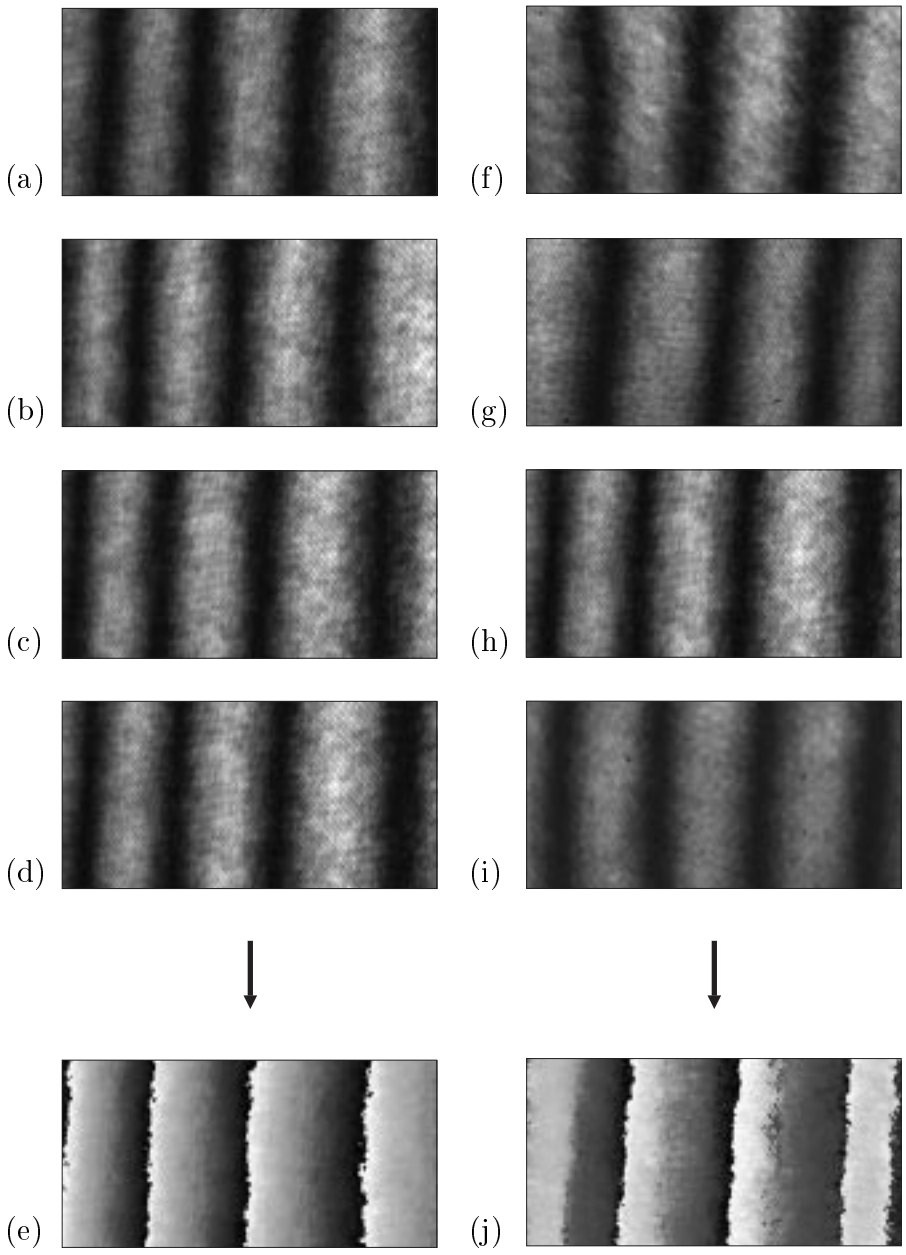

Figure 4.3: Temporal and spatial phase stepping: The interferograms (a) to (d) of one camera, and the interferograms (f) to (i) of four different cameras, and the resulting (e) temporal and (j) spatial phase-stepping images.

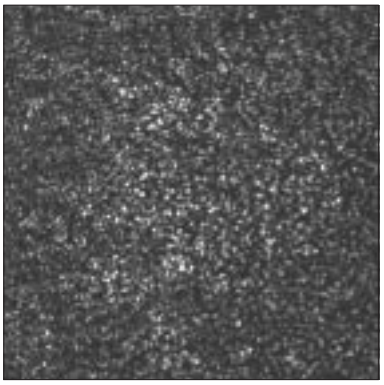

Figure 4.4: Speckle image of CCD camera 4.

density filters to adjust the intensities of the beams. An argon laser with a wavelength of 488 nm and a maximum power of about 1 W is employed, but only about 4 mW are used to illuminate the measurement object. To obtain the results shown in Fig. 4.5, using the temporal phase-stepping method, four phase-stepped speckle images are recorded by each CCD camera (1, 2, and 3) before and after tilting the measurement object, respectively. The phase is calculated using the Carré algorithm. In order to reduce the influence of temporal perturbations, the phase shifts are controlled by correlation coefficients between the speckle patterns. The phases calculated for each CCD camera show nearly the same result.

Figure 4.6 shows the result of the spatial phase-stepping method, and table 4.1 contains the desired phase shifts $\beta(m, n, i)$ of equation (4.4), which

Phase shift	Camera 1	Camera 2	Camera 3	Camera 4
0				×
$\pi/2$			×	
π		×		
$3/2\pi$	×			

Table 4.1: Desired phase shifts of the spatial phase-stepping method.

would be obtained with perfect components of a perfectly aligned interferometer set-up. Four phase-stepped speckle images before and after tilting the measurement object are recorded with the respective CCD cameras, and the phase-stepping image is calculated by the Carré algorithm. Since the measurement object and the interferometer set-up are placed on a vibration-isolated table, the phase shifts between speckle images of different CCD cam-

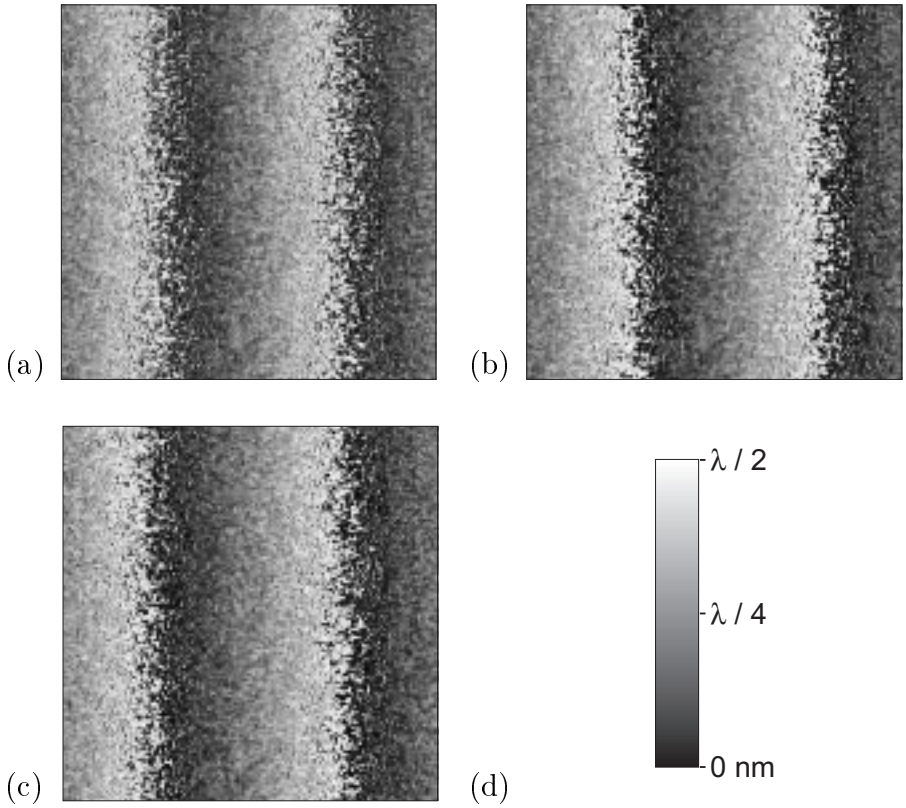

Figure 4.5: Temporal phase-stepping images of CCD cameras (a) 1, (b) 2, and (c) 3, with the gray scales of (d).

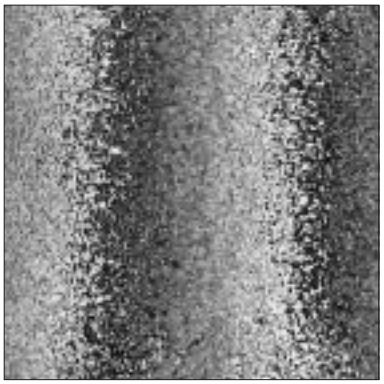

Figure 4.6: Spatial phase-stepping image.

eras are controlled on-line by correlation coefficients. The quality of the spatial phase-stepping image is only slightly inferior to those of the temporal phase-stepping method shown in Fig. 4.5. Since gray scales are used to visualize the phase which contains edges, the perturbations are better detected near transitions from black to white. In order to improve the result, pixels with a low visibility may be marked and, for instance, a median filter employed in order to minimize errors. However, the main error source is the inaccuracy of phase shifts caused by non-perfect optical components.

The phase $\phi(m,n) = \phi(m,n,i)$ of equation (4.2) is calculated correctly if the background intensities $I_0(m,n,i)$, the phases $\phi(m,n,i)$, and the visibilities $\gamma(m,n,i)$ of the CCD cameras $i \in [1,4]$ are independent of i. Furthermore, the phase shifts $\beta(m,n,i)$ have to be spaced equally for using the Carré algorithm. The phase errors, which differ from those of the temporal phase-stepping method, are caused by different sensitivities of CCD cameras or pixels, electronic noise, non-linearities of the CCD cameras, inaccuracy of the phase shifts, and by pixel mismatch relying on the correct alignment of the CCD cameras. The intensity errors due to different sensitivities have to be determined once for each CCD camera and may be considered. The influence of pixel mismatch is minimized by the alignment using on-line correlations.

Figure 4.7 shows the phase differences between the three beams, which impinge on the CCD cameras 1, 2, and 3, when the phase shift between the beams is minimized by maximizing the correlation between the beams. Four temporal phase-stepped speckle images are recorded by each camera, and a phase-stepping image is calculated using the Carré algorithm from 8 speckle images of two different CCD cameras, respectively. These images contain small perturbations, but a significant error caused by pixel mismatch is not observed. The phase differences between beams SB1 and SB3 are about $\lambda/2$ at the right edge at the bottom of Fig. 4.7(b). Hence, the spatial phase-stepping method will have a large error in this region. Therefore, the spatial phase-stepping image of Fig. 4.6 contains larger errors in this region.

Since the employed optical components are not perfect, the temporal phase-stepping method using the smooth reference and the smooth object beams, results in phase-stepping images for each CCD camera, which differ from the images with only one value of gray, even if the components are perfectly aligned. Figure 4.8 shows the result of the aligned interferometer set-up. The components of the paths, which result in beam SB2, are aligned almost perfectly, and only a small tilt around the y-axis is detected. Paths SB1 and SB3 have a curved phase error. The reference path of beam SB4 does not contain a phase shifter, and thus only an interference fringe pattern may be obtained. This pattern has no interference fringes, and the phase

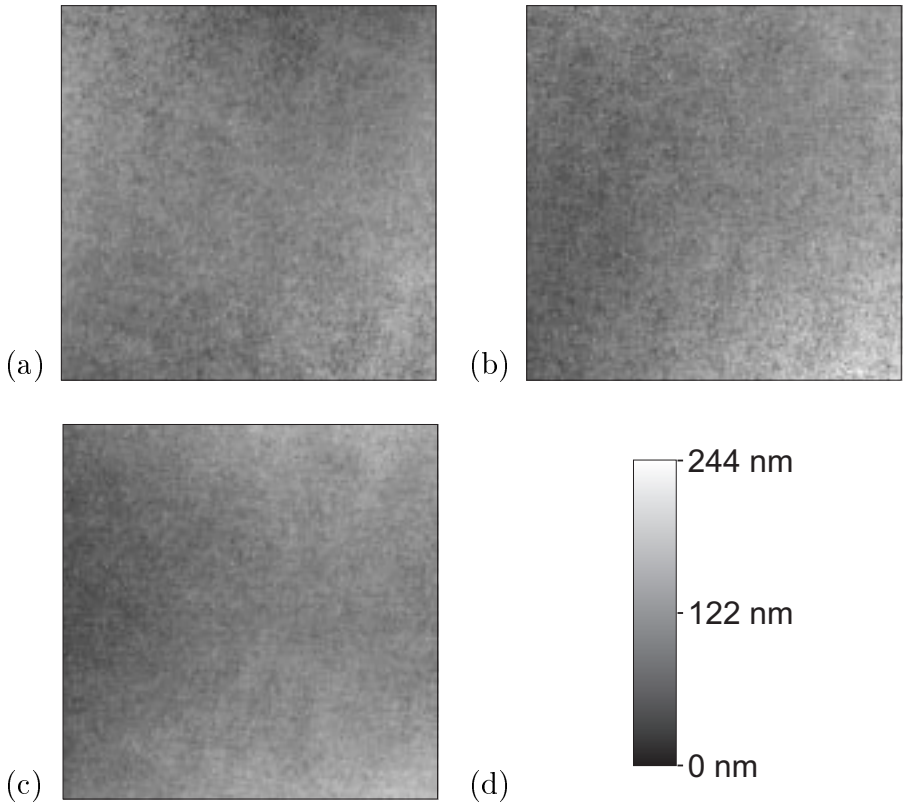

Figure 4.7: Path differences between beams (a) SB1 and SB2, (b) SB1 and SB3, and (c) SB2 and SB3 of Fig. 4.1, with the gray scales of (d).

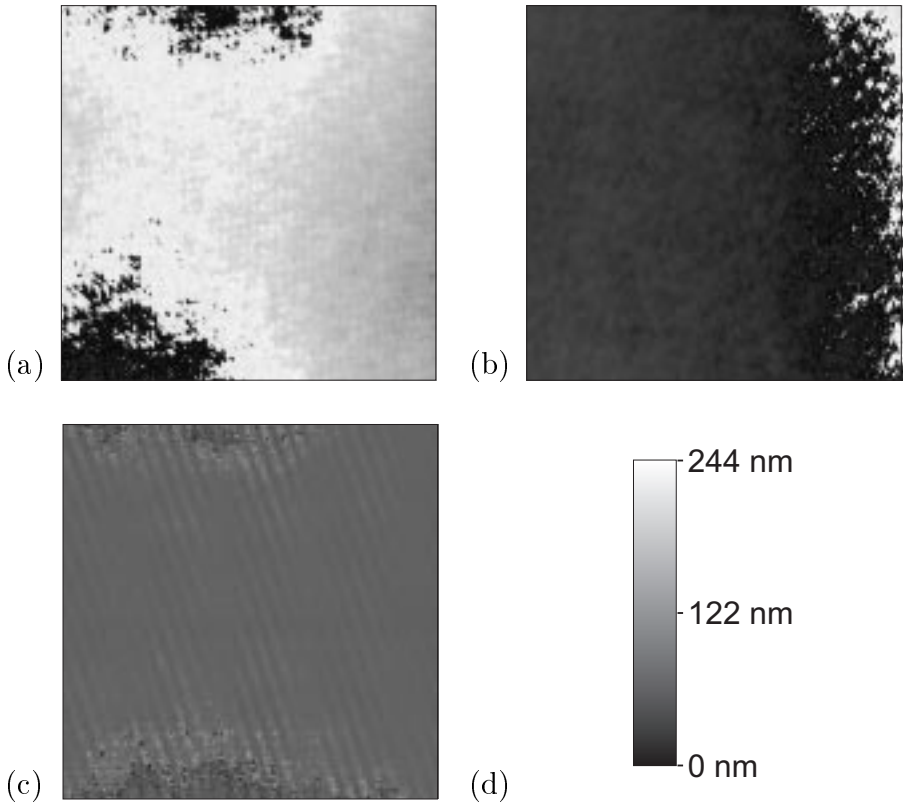

Figure 4.8: Path differences between the reference and object beams of beams (a) SB1, (b) SB2, and (c) SB3 of Fig. 4.1, with the gray scales of (d).

error caused by non-perfect components cannot be determined exactly, but the phase error is less than $\lambda/2 = 244$ nm. Hence, the main error source is the inaccuracy of phase shifts, and the good quality of the spatial phase-stepping image of Fig. 4.6 could not be expected.

In order to improve the accuracy of the phase calculation, the temporal phase-stepping images of Fig. 4.8 have to be determined once for an aligned interferometer set-up, and the phase errors should be eliminated by the phase calculation using an algorithm which permits unequal phase shifts between three phase-stepped interferograms, e.g. a least-squares algorithm. The least-squares solution has to be determined once for any pixel of the CCD cameras, in order to achieve a better accuracy of the phase calculation.

Since the mutual alignment of the CCD cameras leads to high correlation coefficients between recorded speckle images of different CCD cameras, the accuracy of the measurement should be improved by increasing the number of phase-stepped interferograms. Thus the use of an additional phase shifter in the reference beam RB4 of Fig. 4.1, or in the smooth reference beam SMRB, would allow to perform the phase calculation with four phase-stepped interferograms using a least-squares algorithm in order to improve the accuracy.

4.4 Limitations

The measuring distance of the realized four-camera interferometer set-up, the distance between the measurement object and the beginning of the lens system LSOB, is about 260 mm. It may be extended to up to 700 mm employing an lens system with a focal distance of 500 mm, and thus the interferometer set-up would have to be aligned again. A better method to increase the measuring distance, is to use a second, exchangeable lens system as first element of the imaging system. This imaging set-up is shown in Fig. 4.9. For further considerations, the lens systems LSOB1 and LSOB2 are replaced by the imaging lenses IL1 and IL2 with focal distances f_i given by

$$\frac{1}{f_i} = \frac{1}{u_{bi}} + \frac{1}{u_{gi}}, \tag{4.5}$$

with $i \in \{1, 2\}$. Depending on the lens systems, the measuring distances u_{mi} differ from the distances u_{gi}, but the measuring distance u_{m1} is nearly equal to u_{g1} for distances u_{g1} of a few meters. The lateral magnification M_{li} of imaging systems 1 and 2 is given by

$$M_{li} = \frac{u_{bi}}{u_{gi}}. \tag{4.6}$$

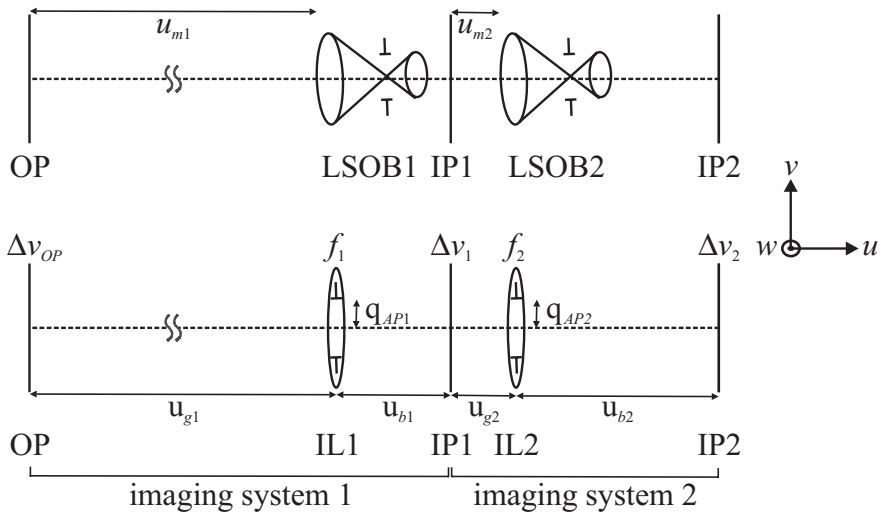

Figure 4.9: Imaging set-up. IL: image lens, IP: image plane, LSOB: lens system of the object beam, OP: object plane.

The spatial resolution Δv_i of the imaging system i is derived by the Raleigh criterion of equation (1.63)

$$\Delta v_i = 1.22 \frac{\lambda u_{bi}}{2q_{APi}}. \tag{4.7}$$

In image plane IP2 the second imaging system has a spatial resolution of $\Delta v_2 = 13.5$ μm if $\lambda = 514$ nm, $2q_{AP2} = 40$ mm, and $u_{b2} = 860$ mm are used. This value may be enhanced by increasing the radius q_{AP2} of the lens system LSOB2. The lateral magnification of this imaging system is $M_{l2} = 3.3$ with $u_{g2} = 260$ mm, and thus two points with a distance of $\Delta v_1 = 4.1$ μm can be just resolved in image plane IP1. The lens system LSOB1 may be used to adapt the imaging system to the measuring distance and to the inspected area of the measurement object. Table 4.2 shows the characteristics

u_{g1}	f_1	u_{b1}	$2q_{AP1}$	Δv_1	M_{l1}	Δv_{OP}
5 m	300 mm	319 mm	70 mm	2.9 μm	1:15.7	45.5 μm
10 m	500 mm	526 mm	60 mm	5.5 μm	1:19	105 μm

Table 4.2: Characteristics of imaging system 1.

of imaging system 1 for two different lens systems and measuring distances of 5 m and 10 m. The spatial resolution in image plane IP1 of image system 2 $\Delta v_1 = 4.1$ μm is lower than that of image system 1 $\Delta v_1 = 2.9$ μm when

$u_{g1} = 5$ m is assumed. Therefore, the imaging system 2 limits the spatial resolution of the total system consisting of image systems 1 and 2. The spatial resolution in image plane IP2 is given by $\Delta v_2 = 13.5$ μm and in the object plane $\Delta v_{OP} = 64$ μm. The spatial resolution of the total system depends on the characteristics of both imaging systems, i.e. the chosen lens systems and the measuring distance.

The employed CCD cameras have a pixel size of 8.3 μm $\times$ 8.3 μm in dimensions and the diameters of the diaphragms $2q_{APi}$ are reduced to obtain a speckle size in image plane IP2, which is at least twice the pixel size. Since high correlation coefficients are obtained with a mean speckle size of three pixels or more, the highest lateral resolution with a measuring distance of 5 m is given by three times the pixel size and thus $\Delta v_2 = 24.9$ μm in image plane IP2, and $\Delta v_{OP} = 120$ μm in the object plane, when, according to table 4.2, $u_{g1} = 5$ m is assumed. The inspected area of the measurement object is 28 mm $\times$ 30 mm when the sensor area of 8.1 mm $\times$ 6.33 mm is used.

Assuming an isotropic and plane measurement surface, a uniform object illumination, no loss of light within the imaging system, and the object being large compared to the finest detail which the imaging system can resolve, the intensity in the image plane decreases as the fourth power of the cosine of angle α between the u-axis of Fig. 4.9 and the principal ray through the image point in the image plane [163]:

$$I \sim cos^4\alpha. \tag{4.8}$$

The average speckle intensity is reduced towards the edges of the CCD sensor area, as shown in Fig. 4.4. Thus, large measuring distances or large distances between lens system and image planes of the CCD cameras should be chosen.

Assuming the optical components of the interferometer to be perfect, approximately 25 % of the energy of the laser light reflected by the measurement object and collected by the imaging system, arrives at each CCD sensor. Thus, four times more energy of laser light is necessary than in a single-camera interferometer set-up. For large measuring distances, e.g. more than 2 m, and for a poorly reflecting measurement object, a high amount of energy is required, and both the smooth object beam and the smooth reference beam need no more than a few percent of the energy which is used to illuminate the measurement object. The distance between the first beam splitter and the reference object has to be increased, but the distance between the reference object and the lens system of the reference beam may remains unchanged. When a highly reflecting rough surface is used as reference object, the amount of energy to illuminate the reference object may be

low, i.e. only a few percent of the energy of the laser light which illuminates the measurement object. Thus, the whole amount of energy of the laser light needed is four to five times more than that of a single-camera interferometer set-up.

The accuracy of this interferometer is mostly dependent on the mutual alignment of the CCD cameras, the temporal perturbations, and the path differences introduced by non-perfect optical components. The CCD cameras may be adjusted by the alignment, using on-line correlation coefficients and displacement vectors. The path length differences caused by non-perfect optical components may be determined and used by the phase calculation. With this improvement, an accuracy of better than $\lambda/10$ should be obtained.

Since a large number of optical components is used, and the path lengths on the vibration-isolated table are up to 2 m, this interferometer set-up is susceptible to temporal perturbations, e.g. air flow, which introduces path length changes in the different beams. Thus, the presented measurement results of the temporal and spatial phase-stepping methods could be obtained using the on-line correlation to control the phase shifts between the speckle images, since the measurement object is placed on the vibration-isolated table, and the speckle images are recorded sequentially and not simultaneously for the spatial phase-stepping method. The interferometer set-up has to be realized to be more compact and to stand in a better shielded environment in order to reduce the influence of temporal perturbations.

With these improvements, the use of a pulsed laser would allow to remove the measurement object from the vibration-isolated table without a reduction of the accuracy of the measurement, since it should be possible to record simultaneously the four phase-stepped speckle patterns with accurate phase shifts. In the case of an interferometer set-up with a smooth reference beam, the four reference beams may be replaced by four polarization-preserving, single-mode fibers to realize a more compact set-up, where the phase shifts are introduced by stretching the fibers. The reference beams may be replaced by image fibers in the case of a speckled reference beam, but the currently available image fibers are not polarization preserving, and thus the change of the state of polarization which reduces the visibility, would have to be taken into account.

Chapter 5

Facts relevant to fusion

In thermonuclear fusion devices, the plasma has to be confined in magnetic fields, but this confinement cannot be perfect. Plasma-wall interactions damage the plasma chamber walls and contaminate the plasma. IPP has concentrated, for instance, its tokamak research with the ASDEX Upgrade experiment on the divertor principle, a special magnetic field configuration. The poloidal cross-section of divertor II ('Lyra') of ASDEX Upgrade is shown in Fig. 5.1. In this region, the magnetic lines of flux cross components of the

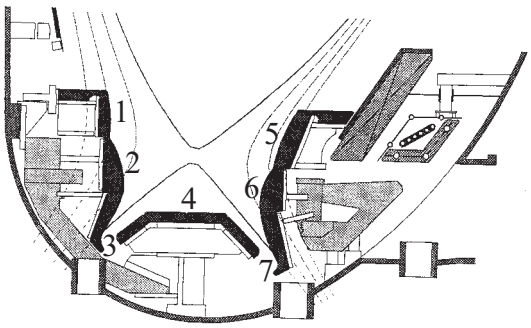

Figure 5.1: Poloidal cross-section of ASDEX Upgrade with divertor II in the 'Lyra' configuration. 1: inner retention module, 2: inner transition module, 3: inner strike point module, 4: roof baffle, 5: outer retention module, 6: outer transition module, 7: outer strike point module.

divertor as well as plasma-wall interactions are concentrated on the target plates (1-7). The divertor principle solves such problems as energy transfer to the walls, erosion, and impurity of plasma. A dense and cold plasma can be formed in front of the target plates in order to limit erosion and impurity flow into the main plasma. The energy flux to the target plates can be reduced by converting it into radiation. The old divertor I used fine-grain

graphite target plates, and divertor II uses carbon fiber composites (CFC). The divertor principle has been adopted for ITER, and CFC or tungsten may be used for the target plates and beryllium for the plasma chamber walls.

Erosion and redeposition processes at target plates have been studied by exposing probes covered with thin layers of examined materials and by measuring the thickness of the remaining layer after exposure. A manipulator system allows the probes to be exchanged through an airlock system to avoid breaking the vacuum in the entire manipulator system. Several materials, such as fine-grain graphite, CFC, silicon, vanadium, molybdenum, or tungsten, have been examined [2, 6, 164]. This manipulator system allows accurate examination of erosion and redeposition processes at several positions and moments, but on-line inspection is impossible.

A high-resolution infrared system allows the measurement of the divertor surface temperature. The system consists of two fast infrared line cameras, one of which viewing from the bottom and the other one viewing from the top of the plasma chamber. The strike point modules are observed from the bottom, using an infrared endoscope and mirrors behind the outer divertor and roof baffle. The measured temperature can be used to calculate the heat flux. Edge-localized modes (ELMs) lead to loss of particles and energy from the plasma and to erosion of the target plates. The infrared system allows, for instance, the time-resolved detection of ELMs. Speckle measurement methods may allow the detection and characterization of surface microrelief changes, such as erosion or redeposition, as shown in chapter 3, and may allow the measurement of surface contours.

5.1 Surface contour

Surface contour measurements may be performed by the two-wavelength method of speckle interferometry, as described in section 1.2.6. The measuring range depends on the two wavelengths used to illuminate the measurement object, and thus on the synthetic wavelength of equation (1.54). The lower limit of the measuring range is given by the surface roughness of the measurement object. The upper limit can be extended to up to some tens of centimeters, but the resolution is decreased accordingly.

A simulation result of a surface contour measurement with differing surface roughnesses, obtained by the simulation program of Ref. [51], is shown in Fig. 5.2. The set-up with a rough measurement and reference object of Fig. 1.5, and the temporal phase-stepping method of section 1.3 are used. The surface contour of a plane measurement object is compared to the surface contour of a plane reference object, which is tilted 48 μm relative to the

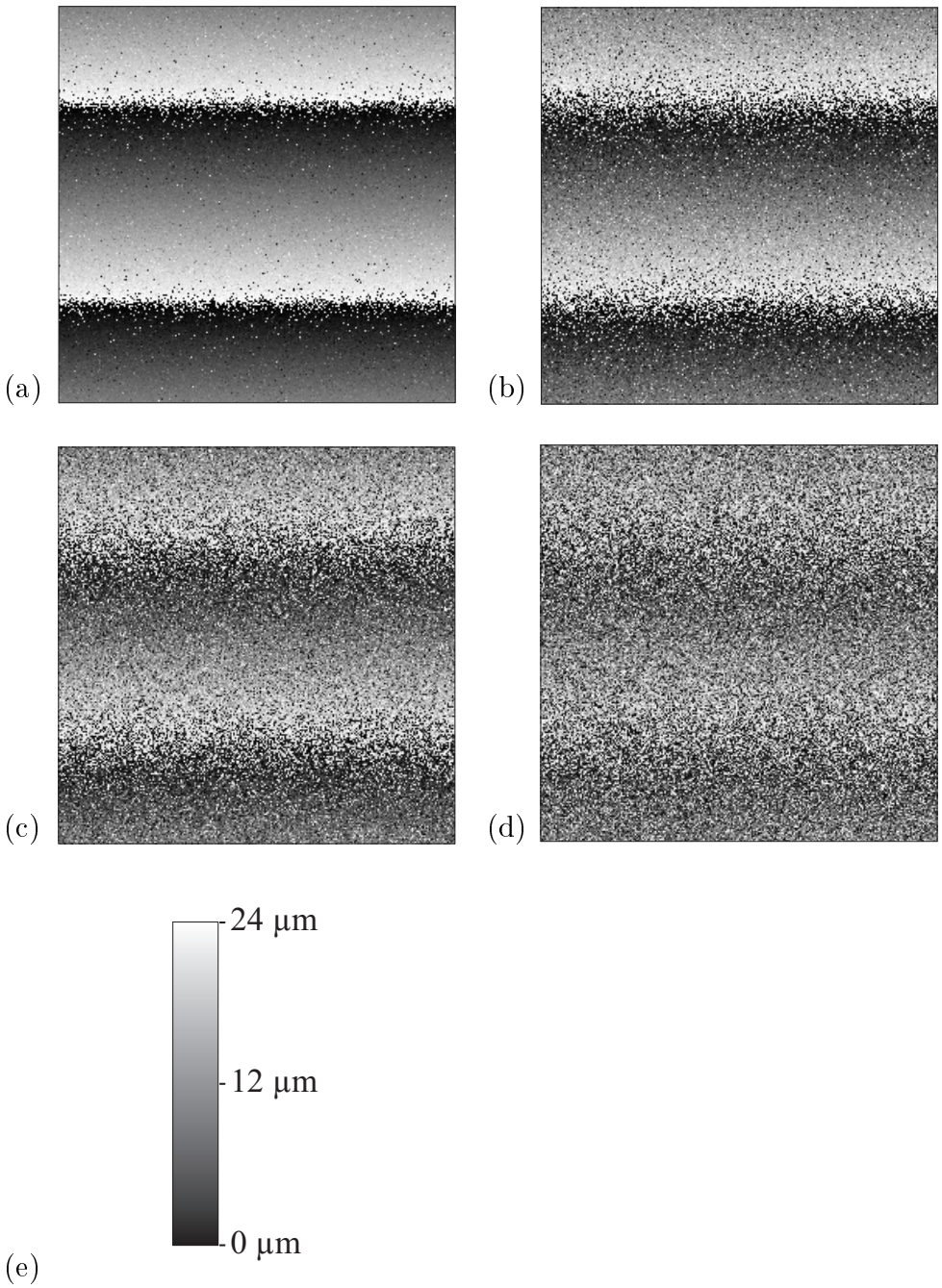

Figure 5.2: Simulation of a surface contour measurement with differing rms surface roughnesses σ_r: (a) 1 μm, (b) 2 μm, (c) 4 μm, and (d) 12 μm; (e) gray scale for $\Lambda = 24$ μm.

measurement object. The observation and illumination angle $\alpha = 0$, and the wavelengths $\lambda_1 = 496.5$ nm and $\lambda_2 = 501.7$ nm yield a synthetic wavelength of $\Lambda = 24$ μm. The result in Fig. 5.2(a), simulated with a rms surface roughness of $\sigma_r = 1$ μm (of both the measurement and the reference object) is of good quality. The quality deteriorates with increasing surface roughness, as shown in Figs. 5.2(b), (c), and (d). In order to obtain surface contour measurements with reasonable quality, the synthetic wavelength should be at least eight times σ_r.

The lower limit of measuring an erosion depth, using a surface contour measurement, is revealed in Fig. 5.3. Two dents in an aluminum surface with

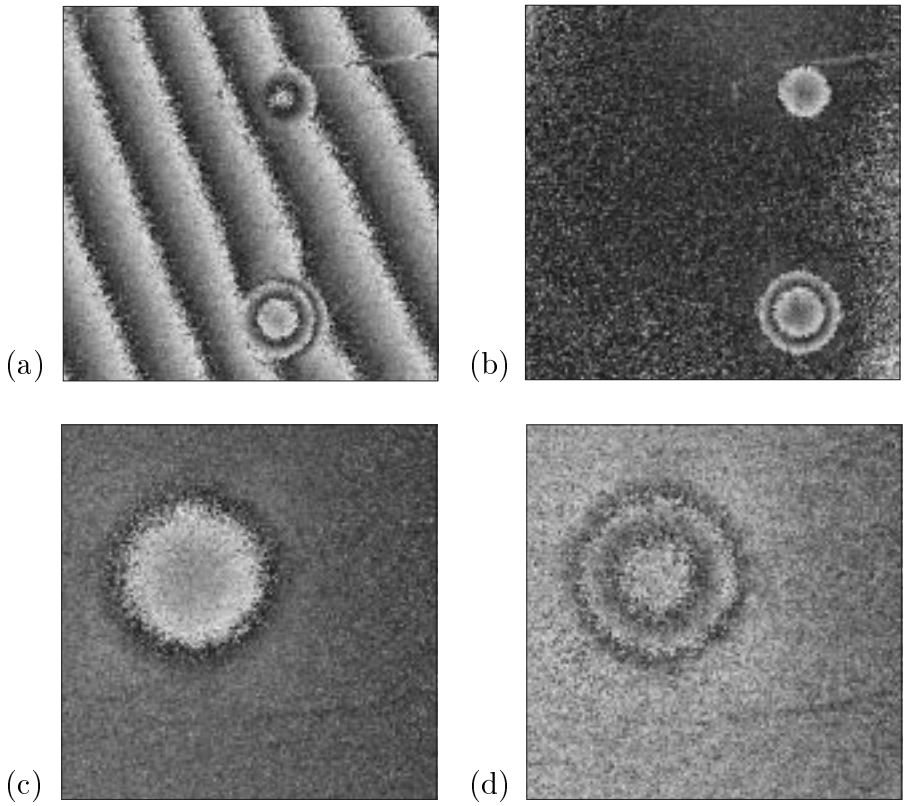

Figure 5.3: Surface contour measurements of two dents with synthetic wavelengths (a), (b), and (c) $\Lambda = 24$ μm, and (d) $\Lambda = 8.9$ μm.

a depth of 20 μm and 40 μm each are measured with synthetic wavelengths $\Lambda = 24$ μm and 8.9 μm. In Fig. 5.3(a) the measured area of 12 mm $\times$ 12 mm is tilted about 170 μm relative to a plane reference surface. The measuring distance used was about 300 mm. The dents are detected clearly, but the depth of the dents may be measured more easily after removing the tilt, as

shown in Fig. 5.3(b). The smaller dent is shown in Figs. 5.3(b) and (c) with two differing synthetic wavelengths, and a measured area of 4 mm × 4 mm, and has been obtained at a measuring distance of about 200 mm. Since the measured area is being decreased, the lateral resolution increases. It is obvious that a surface height difference of 5 μm can be determined. A line scan through the middle of the small dent, measured by a scanning white light interferometer (Zygo NewView 100 [165]), is shown in Fig. 5.4. Surface

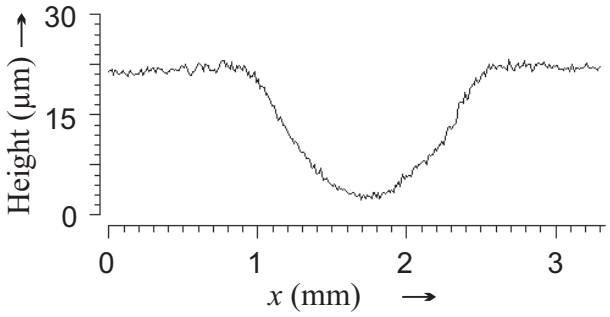

Figure 5.4: Surface contour measured by a scanning white light interferometer.

contour measurements with measuring distances of 3 m and 5.3 m are shown in Fig. 5.5. The measurements have been performed on a vibration-isolated

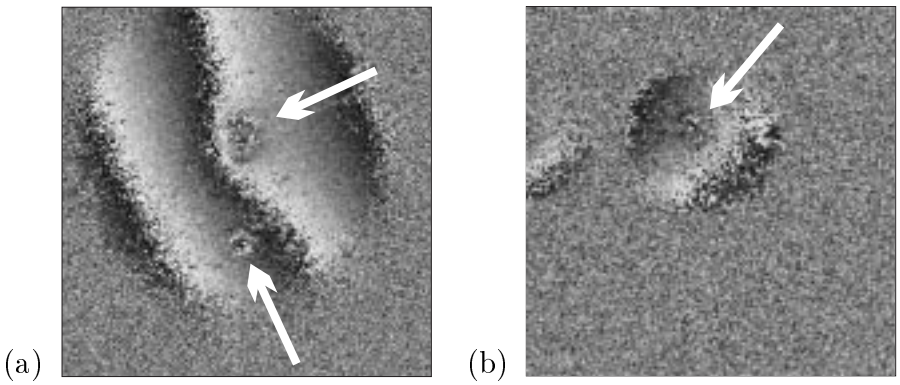

Figure 5.5: Surface contour measurement with differing measuring distances: (a) 3 m and (b) 5.3 m (Λ = 24 μm).

table, where a lot of mirrors were used to extend the measuring distance to up to several meters. The measured area in Fig. 5.5(a) is 20 mm × 20 mm, and 45 mm × 45 mm in Fig. 5.5(b). Since the illuminated area is smaller than the measured area, only part of the images contains a measured surface contour. In Fig. 5.5(a) the dents can be detected, but in Fig. 5.5(b) it is impossible

to detect the small dent. In order to obtain a higher lateral resolution, two lens systems can be used instead of one lens system with large focal distance, as described in section 4.4. Thus, it is possible to measure surface contours which are greater than 5 μm at a measuring distance of 5 m with a lateral resolution of 120 μm.

The surface contour measurements shown have been performed by the temporal phase-shifting method, using the set-up of Fig. 1.5, where the measurement object is positioned on the vibration-isolated table. Since the plasma chamber walls or the target plates cannot be positioned on a vibration-isolated table, the temporal phase-shifting method cannot be applied. But the spatial phase-stepping method can be applied, e.g. when using the smooth reference beam set-up of Fig. 1.6 which is based on a Mach-Zehnder interferometer. The set-up of Fig. 5.6 allows simultaneous

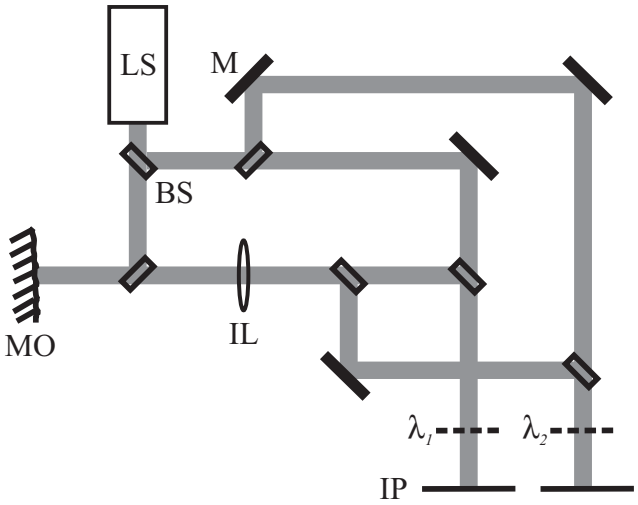

Figure 5.6: Set-up for two wavelengths. BS: beam splitter, IL: image lens, IP: image plane, LS: laser, M: mirror, MO: measurement object.

acquisition of two speckle images with two differing wavelengths when, for instance, interference filters are used to separate the wavelengths λ_1 and λ_2. But the smooth reference set-up only allows comparison of the measurement object to a smooth reference wavefront. Figure 5.7 shows the result of a surface contour measurement performed by the temporal phase-shifting method and by the spatial phase-stepping method with one CCD camera and a smooth reference beam. If the surface contour of the measurement object were more complex and if small surface contour differences, e.g. 20 μm, were to be measured, the reference wavefront would have to be more complex. The four-camera set-up of Fig. 4.1 with a speckled reference beam may

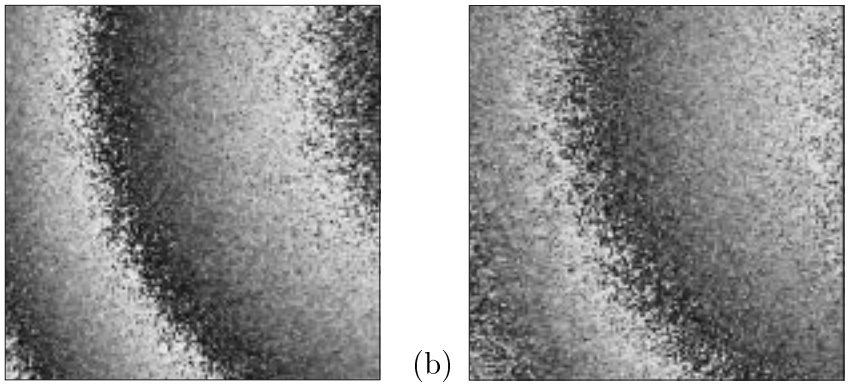

Figure 5.7: Surface contour measurement: (a) temporal and (b) spatial phase-shifting method ($\Lambda = 24$ μm).

be used to measure the surface contour of the measurement object relative to the surface contour of the reference object. Thus, small differences between the measurement object and the reference object can be measured, using small synthetic wavelengths, when the surface contour of the reference object nearly corresponds to the surface contour of the measurement object.

The illumination and observation angles are restricted, because the maximum surface height difference of the smallest surface element has to be smaller than the synthetic wavelength. For the sake of simplicity, the illumination and observation directions are assumed to be parallel, but opposite and perpendicular to the horizontal (dashed) line, as shown in Fig. 5.8. The

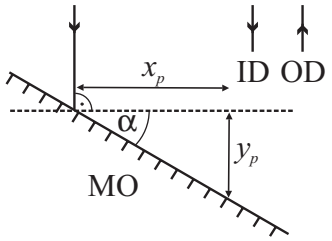

Figure 5.8: Observation geometry. ID: illumination direction, MO: measurement object, OD: observation direction.

smallest surface element is given by the lateral resolution of the optical imaging system, i.e. it depends on the speckle size. In Fig. 5.8 it is assumed that the measurement object and the horizontal line form angle α, and the size of the smallest surface element is x_p in the x-direction. The maximum surface height difference $y_p = x_p \tan\alpha$ has to be smaller than the synthetic

wavelength Λ, i.e.

$$x_p \tan\alpha < \Lambda. \tag{5.1}$$

In the case of a measuring distance of 5 m, a spatial resolution of $x_p = 120$ μm and $\Lambda = 24$ μm, angle α is limited by $\alpha < 11°$. For a measuring distance of 1 m, the spatial resolution could be $x_p = 30$ μm, and yielding $\alpha < 39°$ for $\Lambda = 24$ μm. Thus, the surface contour of the target tiles of divertor II of ASDEX Upgrade cannot be measured from the top of the plasma chamber, but it could be measured from the bottom. An available laser system, consisting of a Nd:YAG laser (second and third harmonic: 532 nm and 355 nm) and an OPO, generates laser pulses (about 5 ns) in the visible range with a pulse energy of up to 200 mJ (Continuum). Because angle α is limited, this pulse energy is sufficient to perform surface contour measurements at low reflecting target plates (e.g. graphite) at distances of at least up to 5 m.

5.2 Detection of erosion

Methods to determine surface contours, as described before, can be used to measure changes of the measurement object when using only one wavelength of laser light at two different states of the measurement object, e.g. before and after a surface microrelief change. In chapter 3 it is described how speckle interferometry allows the detection of surface microrelief changes (e.g. due to erosion or redeposition), the determination of erosion depths or redeposition heights in the nanometer scale, or the determination of a deformation of the measurement object in the nanometer or micrometer scale (e.g. caused by expansion due to temperature changes or mechanical force).

In chapter 3 the temporal phase-shifting method is used in order to reveal the possibilities of speckle interferometry. Measuring distances of up to 500 mm have been used, but they can be extended to up to some tens of meters. Figure 5.9 shows two measured deformations of the measurement object (tilt) at measuring distances of 6.8 m and 9.8 m, respectively. The set-up of Fig. 1.5, based on a Michelson interferometer on a vibration-isolated table, has been used with several mirrors to obtain path lengths of several meters. The measured area of Fig. 5.9(a) is 40 mm $\times$ 40 mm, the measuring distance 6.8 m, the difference between black and white of a gray scale corresponds to a deformation of $\lambda/2 = 244$ nm, and the graphite tile (measurement object) is tilted about 0.75 μm. Figure 5.9(b) shows a deformation of about 0.25 μm of an aluminum surface at a measuring distance of 9.8 m with a measured area of 55 mm $\times$ 55 mm. Since the illuminated area is smaller than the measured area, only part of the images contains a measured deformation. The measured area can be reduced by using either

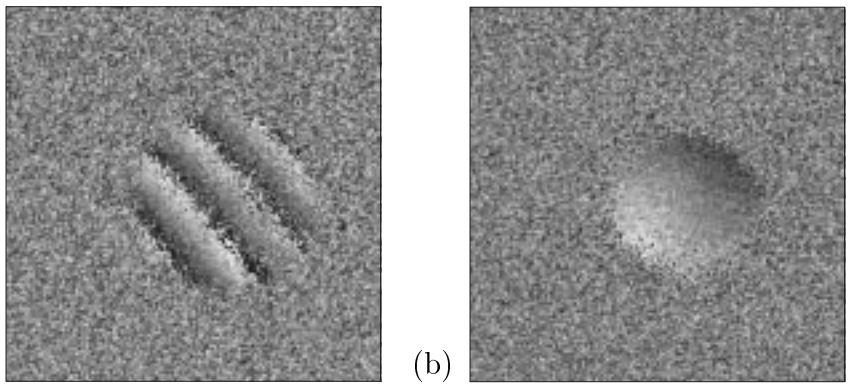

Figure 5.9: Measurement of deformations with differing measuring distances: (a) 6.8 m and (b) 9.8 m.

a lens system with a larger focal distance or two lens systems, as described before. Thus the lateral resolution would be increased.

The temporal phase-shifting method cannot be applied to a measurement object which is not positioned on a vibration-isolated table together with the measuring set-up. Thus, a pulsed laser, together with other speckle interferometry methods, has to be applied. Almost all set-ups can be used to obtain interference fringes. The simplest set-up is the shearing interferometer, as shown in Fig. 1.8. Surface microrelief changes can be detected, but the determination of erosion depths is not possible since surface points are compared to each other. Spatial phase-shifting methods can be used to obtain measurement results for any pixel of the CCD camera, i.e. for any measured surface element. Figure 1.6 shows a simple set-up based on the Mach-Zehnder interferometer with a smooth reference beam. This set-up is suited for the detection of surface microrelief changes and the determination of erosion depths or redeposition heights. It has the advantage that it is very compact when using a polarization-preserving, single-mode fiber in the reference beam. The four-camera set-up of chapter 4 can also be used, but it is more complex.

Angle α of Fig. 5.8 is, in contrast to surface contour measurements, not limited. But it is necessary that sufficient laser light is scattered back from the measurement object to the CCD camera. Thus, the measuring distance depends on angle α, the surface microrelief, and the laser energy available. Deformation measurements, as shown in Fig. 5.9, have been carried out at graphite tiles, at a measuring distance of 9.8 m, with $\alpha = 0°$, $\lambda = 488$ nm, with a continuous-wave argon laser with a maximum power of 1 W, and with a CCD camera with an integration time of 20 ms. Thus, the maximum

energy corresponds to 20 mJ. Frequency-doubled Nd:YAG pulsed lasers with a pulse energy of 1 J, $\lambda = 532$ nm and a pulse duration of 5 ns are available (Continuum), i.e. with 50 times more energy than necessary for $\alpha = 0°$ and a measuring distance of 9.8 m. When an isotropic, rough surface is assumed, the intensity I of the scattered light complies with Lambert's law [163]

$$I = I_0 \cos \alpha, \tag{5.2}$$

where I_0 is the intensity for $\alpha = 0°$. The intensity is reduced to $I = 0.5\, I_0$ when $\alpha = 60°$. If the surface is non-isotropic, the surface microrelief can be measured, and the simulation program of Ref. [51] can be used to determine $I(\alpha)$. Otherwise this dependence $I(\alpha)$ has to be measured directly using a CCD camera. According to equation (1.62) $I_0 \sim 1/x^2$, where x is the measuring distance. Generally, the available laser energy of 1 J should be sufficient to perform measurements with one wavelength at measuring distances of up to 10 m.

5.3 Limitations

In speckle measurement methods, characteristic data, e.g. measuring distance or measuring range, are limited for many reasons. Surface roughness measurement methods, as described in section 1.1, can be used to determine a surface roughness change. Measurements have been performed at measuring distances of up to 500 mm, but it would be difficult to do the same at measuring distances of several meters. Speckle interferometry methods can be applied at measuring distances of several meters, as described before, but other limitations have to be taken into account.

The material of the measurement object should be optically rough, i.e. materials such as graphite, CFC, tungsten, aluminum or steel can be used. If the material is partially optically transparent, light is not only reflected from the surface, but also from the interior, and will disturb the measurement. But measurements using graphite with a thin layer of silicon have worked well.

Since the measurement object is not positioned on a vibration-isolated table together with the measuring set-up, motions of the measurement object during the measurement will cause perturbations. When a pulsed Nd:YAG laser with a pulse duration of 5 ns is used, the motion of the measurement object during 5 ns can be neglected. But the motion during two consecutive time instances of the measurement (two states of the measurement object or two wavelengths) has to be considered. This time duration depends on the repetition rate of the laser and the CCD camera system. In the case

of the four-camera system, described in chapter 4, and a Nd:YAG pulsed laser with a repetition rate of 10 Hz, the time duration is 100 ms. During this time duration the motion of the measurement object must not lead to a decorrelation which is too strong. In case of an out-of-plane sensitive measurement, an out-of-plane motion only leads to an additional phase shift. But, depending on the optical imaging system, i.e. on the speckle size, an in-plane motion leads to decorrelation. The in-plane motion has to be much smaller than the smallest, optically resolved surface element. Without larger decorrelation, a measurement uncertainty of $\lambda/10$ and $\Lambda/10$ is to be expected.

Plasma emits light in the visible range, and this leads to a background intensity which perturbs the measurement. In order to reduce the background intensity, a filter has to be used, which transmits only the wavelength of the laser light used. Further, the integration time of the CCD cameras of the four-camera system can be reduced down to 1 ms and synchronized with a pulsed laser. This should be sufficient. Other CCD cameras allow an integration time of as little as 64 μs, or multichannel-plate cameras would allow integration times as little as the pulse duration of the laser, e.g. 5 ns.

When the laser beam passes the optical access to the plasma chamber, e.g. a quartz window, a very small part of laser light will be reflected by the window. These reflections must not reach the CCD camera since already reflections of 1 % of laser light will cause a higher intensity than the scattered light of a low-reflecting graphite target at a distance of 3 m behind the window. Thus, multichannel-plate cameras have to be used in order to separate the reflections by time, or else two windows have to be used, one for the laser beam and the other for the scattered light.

A change of the refractive index, e.g. due to change of temperature or pressure, causes an additional phase change. If this change is homogeneous over the cross-section of the laser beam or the scattered light, the measurements are not affected by perturbations. If not, the additional phase change will be measured and cannot be distinguished from other phase changes. But surface microrelief changes can be distinguished from the additional phase change since surface microrelief changes reduce the fringe contrast or the visibility.

Conclusions

Laser-speckle-based measurement techniques, which are relevant to fusion devices, have been examined. The surface measurement techniques should be able to detect surface microrelief changes due to erosion or redeposition, and should allow to determine erosion depths or redeposition heights at inner wall materials of fusion devices at measuring distances of several meters. Speckle interferometry meets these requirements.

It has been shown that surface microrelief changes can be detected, when using the temporal phase-shifting method of speckle interferometry. When the surface height distribution and its change are known, the erosion depth or redeposition height may be determined in the range of 0 nm up to one fourth of the wavelength of the used laser light (e.g. 133 nm with $\lambda = 532$ nm), using a simulation program of speckle interferometry. Depths or heights greater than 5 μm can be measured by surface contour measurements with two differing wavelengths. In order to adapt the measuring range, the wavelengths are chosen accordingly. The uncertainty of measurement is typically $\Lambda/10$ and $\lambda/10$, respectively if only one wavelength is used. In order to apply the temporal phase-shifting method, the measurement object has to be positioned on a vibration-isolated table together with the measuring set-up. Since inner wall materials of fusion devices cannot be vibration-isolated, other phase-shifting methods of speckle interferometry have to be applied.

Spatial phase-shifting methods using a pulsed laser are suitable to perform measurements at measurement objects which are not vibration-isolated. A simple and compact interferometer set-up uses a smooth reference beam, in which a large tilt is introduced to obtain a phase shift between adjacent pixels of the CCD camera. This set-up allows the detection of surface microrelief changes and the determination of erosion depths or redeposition heights, but the surface contour of the measurement object can only be compared to a smooth reference beam, i.e. to a plane surface contour. When the measurement object has a more complex surface contour, e.g. a curvature of 10 mm in the measured area, a small depth or height, for instance, a dent of 20 μm, cannot be measured.

In order to allow such kind of measurements, a new four-camera set-up has been developed. Four phase-stepped interferograms can be recorded simultaneously with four CCD cameras, and the phase steps are introduced by path length changes of the reference beams. First measurement results using smooth reference beams, a continuous-wave argon laser, and a measurement object together with the measuring set-up on a vibration-isolated table, have shown that this set-up works well. This four-camera set-up offers the possibility to use a reference object in order to allow surface contour measurements of the measurement object compared to the reference object. Thus, even if the measurement object has a complex surface contour, small differences, e.g. a dent of 20 μm, may be determined.

Phase-shifting methods yield the measurable variable modulo π or 2π, which means that the phase contains edges. A new method has been developed to reconstruct three-dimensionally the phase change or the surface contour. The edge detection is performed by means of a wavelet transformation, and the Bayesian probability theory is used to find the optimal solution of a three-dimensional spline which will be as complex as necessary and will simultaneously fit the data as well as necessary.

Much work remains to be done, and the following proposals for further research are made: The four-camera set-up has to be developed further, so that a pulsed laser and a reference object can be used. Polarization-preserving, single-mode fibers may be used for the smooth reference beams and the phase steps should be obtained by stretching the fibers. Thus, the set-up may be realized to be more compact and less susceptible to perturbations. In the case of a speckled reference beam, i.e. when using a reference object, image fibers may be used.

The influence of surface microrelief changes on speckle interferometry has to be investigated further. In experiments in a laboratory, the surface microrelief may be measured before and after an erosion or a redeposition, using conventional surface measurement techniques. Using these data in the simulation program of speckle interferometry, simulation results and measured results of speckle interferometry may be compared. Thus, the knowledge of the influence of surface microrelief changes on the speckle interferometry may be improved, and the measuring range of erosion depths or redeposition heights and the uncertainty of their measurement may be determined.

List of symbols

a, s	Dilation
b	Translation
c	Speed of the light
d	Data
$d_{t,m}$	Theoretical data value
$\vec{e}$	Unit vector
f	Function
g	Numerator
h	Denominator
i, k	Incremental counter
j	Unit imaginary
k_λ	Wave number
$\vec{k}_\lambda$	Wave vector
l, l_x, l_y, l_z	Speckle dimension
m, n	Integer
p	Probability
q	Dimension of the illuminated area
r	Surface height
Δr	Variation in the surface height
s	Path length
t	Time
$u, v, w, x, y, z, \vec{x}$	Spatial coordinates
x_f	Focal distance
x_s	Lateral shear
$\vec{x}'$	Translation

A, A_i, B	Proposition
C, C_I	Contrast
C_c, C_d, C_t	Correlation coefficients
C_f	Fringe contrast
C_s	Spatial autocorrelation

C_{12}	Correlation coefficient
C_ψ	Normalization constant
D	Data
$E, \vec{E}$	Electric field
$\vec{F}$	Two-dimensional wavelet transform
G	Area
I	Intensity
I_0	Background intensity
K	Information, knowledge
M_l	Lateral magnification
N	Number of data values
O_ν	Observable
P	Power
R_a	Average roughness
R_I	Reflectivity
S	Shannon entropy
T^{wav}	Continuous wavelet transform
α	Angle
β	Phase
γ	Visibility
ϵ	Permittivity
λ	Wavelength
μ	Parameter
ν	Integer
ξ	Coordinate
ρ	Surface model
σ	Error
σ_b	Spectral bandwidth
σ_I	Root-mean-square of intensity I
σ_p	Root-mean-square of the optical path fluctuations
σ_r	Root-mean-square of the surface roughness
ϕ	Function
ϕ_s	Function dilated by s
φ	Function
$\varphi^{(i)}$	i th derivative of function φ
χ^2, η	Random variables
ψ	Wavelet
$\psi_{a,b}$	Wavelet with dilation a and translation b
$\vec{\psi}$	Two-dimensional wavelet

$\vec{\psi}_s$	Two-dimensional wavelet dilated by s
$\hat{\psi}$	Fourier transform of ψ
ω	Angular frequency
ω_s	Spatial angular frequency
Δ	Difference
Φ	Phase
Φ_r	Reference phase
Ψ	Measure for the global curvature
$\mathcal{L}$	Lagrange function
$\mathcal{R}$	Real number
$\mathcal{Z}$	Integer number
$\vert$	Given
$\vert \quad \vert$	Modulus
$\vert\vert \quad \vert\vert$	Norm
$\cdot$	Multiplication
$*$	Convolution product
*	Complex conjugation
$\sim$	Proportional to
$\vec{\nabla}$	Gradient
$\sum$	Sum
$\int$	Integral
$<>$	Expectation value, ensemble average
$\circ$	Degree
$\bar{}$	Mean value
not	Negation
$\mathcal{R}e$	Real part
exp	Exponential function

List of abbreviations

AP	Aperture Plane
ASC	Angular Speckle Correlation
ASDEX	Axially Symmetric Divertor Experiment
BE	Beam Expander
BS	Beam Splitter
CCD	Charge Coupled Device
CCIR	Comité Consultatif International Radio
CFC	Carbon Fiber Composites
CLA	Center Line Average
ELM	Edge Localized Mode
ESPI	Electronic Speckle Pattern Interferometry
Fig.	Figure
Figs.	Figures
ID	Illumination Direction
IL	Image Lens
IP	Image Plane
IPP	Max-Planck-Institut für Plasmaphysik
ITER	International Thermonuclear Experimental Reactor
JET	Joint European Torus
LS	Light Source or Laser
LSOB	Lens System of the Object Beam
LSRB	Lens System of the Reference Beam
LVDT	Linear Variable Differential Transformer
M	Mirror
MO	Measurement Object
Nd:YAG	Neodymium Yttrium Aluminum Garnet
OB	Object Beam
OD	Observation Direction
OP	Object Plane
OPO	Optical Parametrical Oscillator
OSP	Observation Plane

PC	Personal Computer
PS	Phase Shifter
RAM	Random Access Memory
RB	Reference Beam
Ref.	Reference
RO	Reference Object
rms	Root-mean-square
SB	Superimposed beam
SF	Single Mode Fiber
SMOB	Smooth Object Beam
SMRB	Smooth Reference Beam
SPOB	Speckled Object Beam
SPRB	Speckled Reference Beam
SPS	Spatial Phase Shifting
SSC	Spectral Speckle Correlation
TPS	Temporal Phase Shifting

Bibliography

[1] U. Schumacher. *Fusionsforschung: Eine Einführung.* Wissenschaftliche Buchgesellschaft, Darmstadt, 1993.

[2] *Annual Report 1998.* Max-Planck-Institut für Plasmaphysik (IPP), Garching, 1999.

[3] *Kernfusion - Berichte aus der Forschung, Folge 1.* Max-Planck-Institut für Plasmaphysik (IPP), Garching, 1995.

[4] *Presseinformation des IPP 1/00: Eckdaten für Fusionsreaktor ITER neu festgelegt.* Max-Planck-Institut für Plasmaphysik (IPP), Garching, 2000.

[5] C. García-Rosales, R. Behrisch, D. Hildebrandt, B. Jüttner, W. Schneider, and H. Wolf. Erosion at the divertor tiles of ASDEX-Upgrade. In R. Pick and G. Thomas, editors, *Proceedings of the 21st European Conference on Controlled Fusion and Plasma Physics*, Montpellier, France, pages 718–721, 1994.

[6] *Annual Report 1997.* Max-Planck-Institut für Plasmaphysik (IPP), Garching, 1998.

[7] E. Hecht. *Optics.* Addison-Wesley, New-York, 1990.

[8] D. Malacara, editor. *Optical Shop Testing.* John Wiley, New York, 1992.

[9] I. Newton. *Opticks (Republication of the edition first published by G. Bell, book one, part I, prop. VIII, prob. II, 1730).* Dover, New York, 1952.

[10] P. Hariharan. *Optical holography.* Cambridge University Press, Cambridge, 1984.

[11] J. A. Leendertz. Interferometric displacement measurement on scattering surfaces utilizing speckle effect. *J. Phys. E*, 3:214–218, 1970.

[12] A. W. Koch, M. W. Ruprecht, O. Toedter, and G. Häusler. *Optische Meßtechnik an technischen Oberflächen.* Expert, Renningen, ISBN 3-8169-1372-5, 1997.

[13] K. Exner. Über die Fraunhofer'schen Ringe, die Quelet'schen Streifen und verwandte Erscheinungen. *Sitzungsbericht der kaiserlichen Akademie der Wissenschaften (Wien)*, 76:522–550, 1877.

[14] K. Exner. Ueber die Newton'schen Staubringe. *Annalen der Physik und Chemie*, 9:239–260, 1880.

[15] P. Hariharan. Speckle patterns: a historical retrospect. *Optica Acta*, 19:791–793, 1972.

[16] M. von Laue. Die Beugungserscheinungen an vielen unregelmäßig verteilten Teilchen. *Sitzungsberichte der königlich preussischen Akademie der Wissenschaften (Berlin)*, 44:1144–1163, 1914.

[17] J. C. Dainty. The statistics of speckle pattern. In E. Wolf, editor, *Progress in Optics*, pages 1–45. Elsevier, Amsterdam, 1976.

[18] J. D. Briers. Surface roughness evaluation. In R. S. Sirohi, editor, *Speckle Metrology*, pages 373–426. Marcel Dekker, New York, 1993.

[19] J. M. Bennett and L. Mattsson. *Introduction to surface roughness and scattering.* Optical Society of America, Washington DC, 1989.

[20] D. J. Whitehouse. *Handbook of surface metrology.* Institute of Physics Publishing, Bristol, 1994.

[21] H. Sorg. *Praxis der Rauheitsmessung und Oberflächenbeurteilung.* Carl Hanser Verlag, München, Wien, 1995.

[22] H. von Weingraber and M. Abou-Aly. *Handbuch Technische Oberflächen: Typologie, Messung und Gebrauchsverhalten.* Vieweg Verlag, Braunschweig, 1989.

[23] DIN 4760. *Gestaltabweichung: Begriffe, Ordnungssysteme.* Beuth Verlag, Berlin, 1982.

[24] DIN 4762. *Oberflächenrauheit: Begriffe, Oberfläche und ihre Kenngrößen.* Beuth Verlag, Berlin, 1989.

[25] DIN 4768. *Ermittlung der Rauheitskenngrößen R_a, R_z, R_{max} mit elektrischen Tastschnittgeräten.* McGraw-Hill, Berlin, 1990.

[26] J. W. Goodman. Statistical properties of laser speckle patterns. In J. C. Dainty, editor, *Laser Speckle and Related Phenomena*, pages 9–75. Springer, Berlin, 1975.

[27] R. Reif. *Fundamentals of statistical and thermal physics.* Mc Graw-Hill, New York, 1965.

[28] M. Françon. *Laser Speckle and Application in Optics.* Academic Press, New York, 1979.

[29] Q. B. Li and F. P. Chiang. Three-dimensional dimension of laser speckle. *Appl. Opt.*, 31:6287–6291, 1992.

[30] R. Jones and C. Wykes. *Holographic and speckle interferometry.* Cambridge University Press, Cambridge, 1983.

[31] J. W. Goodman. Dependence of image speckle contrast on surface roughness. *Opt. Comm.*, 14:323–327, 1975.

[32] H. Fujii and T. Asakura. A contrast variation of image speckle intensity under illumination of partially coherent light. *Opt. Comm.*, 12:32–38, 1974.

[33] G. Parry. Statistical properties of laser speckle patterns. In J. C. Dainty, editor, *Laser Speckle and Related Phenomena*, pages 77–121. Springer, Berlin, 1975.

[34] H. Fujii and T. Asakura. Statistical properties of image speckle patterns in partially coherent light. *Nouv. Rev. Optique*, 6:5–14, 1975.

[35] J. Ohtsubo and T. Asakura. Statistical properties of speckle intensity variations in the diffraction field under illumination of partially coherent light. *Nouv. Rev. Optique*, 6:189–195, 1975.

[36] G. Parry. Some effects of temporal coherence on the first order statistics of speckle. *Optica Acta*, 21:763–772, 1974.

[37] H. M. Pedersen. On the contrast of polychromatic speckle patterns and its dependence on surface roughness. *Optica Acta*, 22:15–24, 1975.

[38] Y. Hu. Dependence of polychromatic-speckle-pattern contrast on imaging and illumination directions. *Appl. Opt.*, 33:2707–2714, 1994.

[39] H. Fujii and J. W. Y. Lit. Measurement of surface roughness using dichromatic speckle. *Opt. Comm.*, 22:231–235, 1977.

[40] H. Fujii and J. W. Y. Lit. Surface roughness measurement using dichromatic speckle pattern: an experimental study. *Appl. Opt.*, 17:2690–2694, 1978.

[41] P. Lehmann, S. Patzelt, and A. Schöne. Surface roughness measurement by means of polychromatic speckle elongation. *Appl. Opt.*, 36:2188–2197, 1997.

[42] S. Patzelt, A. Ciossek, P. Lehmann, and A. Schöne. Laseroptische Rauheitsmessung an technischen Oberflächen durch prozeßangepaßte Erfassung und Auswertung polychromatischer Specklemuster. In *Proceedings X. Meßtechnisches Symposium des Arbeitskreises der Hochschullehrer für Meßtechnik (AHMT), TU München, 1996*, pages 37–42.

[43] P. Lehmann, S. Patzelt, and A. Ciossek. In-process-Charakterisierung von Mikrotopographien technischer Oberflächen durch polychromatische Speckleautokorrelation. *Technisches Messen*, 66:269–276, 1999.

[44] B. Ruffing. *Berührungslose Rauheitsmessung technischer Oberflächen mit Speckle-Korrelationsverfahren.* PhD thesis, Universität Karlsruhe (TH), Germany, 1987.

[45] B. Ruffing. Application of speckle-correlation methods to surface-roughness measurement: a theoretical study. *J. Opt. Soc. Am. A*, 3:1297–1304, 1986.

[46] B. Ruffing and J. Fleischer. Spectral correlation of partially or fully developed speckle patterns generated by rough surfaces. *J. Opt. Soc. Am. A*, 2:1637–1643, 1985.

[47] H. M. Pedersen. Object-roughness dependence of partially developed speckle patterns in coherent light. *Opt. Comm.*, 16:63–67, 1976.

[48] A. Papoulis. *Probability, random variables and stochastic processes.* Beuth Verlag, Tokyo, 1965.

[49] M. Ruprecht. *Ferndiagnostik technischer Oberflächen mittels Laser-Speckle-Verfahren.* Shaker Verlag, Aachen, ISBN 3-8256-4540-0, 1998.

[50] M. Jakobi, P. Evanschitzky, and A. W. Koch. Erosionsmessung an rauhen Oberflächen mittels Streifenkontrast in der Speckle-Interferometrie. *Technisches Messen*, 66:163–168, 1999.

[51] P. Evanschitzky, M. Ruprecht, and A. W. Koch. Coherent raytracing for simulation of laser speckle generated by light scattering on rough surfaces. *To be published.*

[52] A. E. Ennos. Speckle interferometry. In J. C. Dainty, editor, *Laser Speckle and Related Phenomena*, pages 203–253. Springer, Berlin, 1975.

[53] A. E. Ennos. Speckle interferometry. In E. Wolf, editor, *Progress in Optics*, pages 233–288. Elsevier, Amsterdam, 1978.

[54] J. A. Leendertz and J. N. Butters. An image-shearing speckle-pattern interferometer for measuring bending moments. *J. Phys. E*, 6:1107–1110, 1973.

[55] Y. Y. Hung. A speckle-shearing interferometer: a tool for measuring derivatives of surface displacements. *Opt. Comm.*, 11:132–135, 1974.

[56] D. E. Duffy. Moire gauging of in-plane displacement using double aperture imaging. *Appl. Opt.*, 11:1778–1781, 1972.

[57] R. Jones and J. A. Leendertz. Elastic constant and strain measurements using a three beam speckle pattern interferometer. *J. Phys. E*, 7:653–657, 1974.

[58] G. C. Holst. *CCD Arrays, Cameras, and Displays.* SPIE, Bellingham, 1996.

[59] S. Winther and G. A. Slettemoen. An ESPI contouring technique in strain analysis. *SPIE*, 473:44–47, 1984.

[60] Y. Zou, H. Daio, X. Peng, and H. Tiziani. Geometry for contouring by electronic speckle pattern interferometry based on shifting illumination beams. *Appl. Opt.*, 31:6616–6621, 1992.

[61] J. Evertz. *Optische 3D-Formerfassung durch den Einsatz von speckle-interferometrischen Meßverfahren.* Shaker Verlag, Aachen, 1997.

[62] C. Joenathan, B. Pfister, and H. J. Tiziani. Contouring by electronic speckle pattern interferometry employing dual beam illumination. *Appl. Opt.*, 29:1905–1911, 1990.

[63] T. Maack, G. Notni, and W. Schreiber. Three-coordinate measurement of an object surface with a combined two-wavelength and two-source phase-shifting speckle interferometer. *Opt. Comm.*, 115:576–584, 1995.

[64] V. Petrov and B. Lau. Electronic speckle pattern interferometry with a holographically generated reference wave. *Opt. Eng.*, 35:2363–2370, 1996.

[65] C. Wykes. De-correlation effects in speckle-pattern interferometry. I. Wavelength change dependent de-correlation with application to contouring and surface roughness measurement. *Optica Acta*, 24:517–532, 1977.

[66] R. Jones and C. Wykes. De-correlation effects in speckle-pattern interferometry. II. Displacement dependent de-correlation and applications to the observation of machine-induced strain. *Optica Acta*, 24:533–550, 1977.

[67] R. Jones and C. Wykes. General parameters for the design and optimization of electronic speckle pattern interferometers. *Optica Acta*, 28:949–972, 1981.

[68] G. A. Slettemoen. General analysis of fringe contrast in electronic speckle pattern interferometry. *Optica Acta*, 26:313–327, 1979.

[69] C. Wykes. A theoretical approach to the optimization of electronic speckle interferometry fringes with limited laser power. *Journal of Modern Optics*, 34:539–554, 1987.

[70] T. W. Ng and F. S. Chau. Effect of camera spatial resolution on fringe contrast in digital speckle correlation interferometry. *Optik*, 97:183–185, 1994.

[71] M. Lehmann. Measurement optimization in speckle interferometry: the influence of the imaging lens aperture. *Opt. Eng.*, 36:1162–1168, 1997.

[72] G. Cedilnik, A. Kiessling, and R. Kowarschik. One-shot interferometer with simultaneous recording of the signal intensity. In V. J. Corcoran and T. A. Goldman, editors, *Proceedings of the International Conference on LASERS'98*, Tucson, USA, pages 1110–1014, 1998.

[73] K. Creath. Temporal phase measurement methods. In D. W. Robinson and G. T. Reid, editors, *Interferogram Analysis: Digital Fringe Pattern Measurement Techniques*, pages 94–140. Institute of Physics Publishing, Bristol, 1993.

[74] J. E. Greivenkamp. Generalized data reduction for heterodyne interferometry. *Opt. Eng.*, 23:350–352, 1984.

[75] J. E. Greivenkamp and J. H. Bruning. Phase shifting interferometers. In D. Malacara, editor, *Optical Shop Testing*, pages 501–598. John Wiley, New York, 1992.

[76] K. Creath. Phase-measurement interferometry techniques. In E. Wolf, editor, *Progress in Optics*, pages 349–393. Elsevier, Amsterdam, 1988.

[77] P. Carré. Installation et utilisation du comparateur photoélectrique et interférentiel du bureau international des poids et mesures. *Metrologia*, 2:13–23, 1966.

[78] J. Schwider, O. Falkenstörfer, H. Schreiber, A. Zöller, and N. Streibl. New compensating four-phase algorithm for phase-shift interferometry. *Opt. Eng.*, 32:1883–1885, 1993.

[79] P. Hariharan, B. F. Oreb, and T. Eiju. Digital phase-shifting interferometry: a simple error-compensating phase calculation algorithm. *Appl. Opt.*, 26:2504–2506, 1987.

[80] J. Schwider, R. Burow, K. E. Elssner, J. Grzanna, R. Spolaczyk, and K. Merkel. Digital wave-front measuring interferometry: some systematic error sources. *Appl. Opt.*, 22:3421–3432, 1983.

[81] K. G. Larkin and B. F. Oreb. Design and assessment of symmetrical phase-shifting algorithms. *J. Opt. Soc. Am. A*, 9:1740–1748, 1992.

[82] C. J. Morgan. Least-squares estimation in phase-measurement interferometry. *Opt. Letters*, 7:368–370, 1982.

[83] G. Lai and T. Yatagai. Generalized phase-shifting interferometry. *J. Opt. Soc. Am. A*, 8:822–827, 1991.

[84] J. Schwider. Advanced evaluation techniques in interferometry. In E. Wolf, editor, *Progress in Optics*, pages 271–359. Elsevier, Amsterdam, 1990.

[85] M. Adams, K. D. Hinsch, F. Lange, and K. Wolff. Polarization effects in speckle correlation metrology. *Opt. Eng.*, 36:2225–2228, 1997.

[86] G. A. Slettemoen and J. C. Wyant. Maximal fraction of acceptable measurements in phase-shifting speckle interferometry: a theoretical study. *J. Opt. Soc. Am. A*, 3:210–214, 1986.

[87] J. Burke and H. Helmers. Performance of spatial vs. temporal phase shifting in ESPI. *SPIE*, 3744:188–199, 1999.

[88] T. Maack and R. Kowarschik. Camera influence on the phase-measurement accuracy of a phase-shifting speckle interferometer. *Appl. Opt.*, 35:3514–3524, 1996.

[89] M. Lehmann. Optimization of wavefield intensities in phase-shifting speckle interferometry. *Opt. Comm.*, 118:199–206, 1995.

[90] M. Lehmann. Phase-shifting speckle interferometry with unresolved speckles: A theoretical investigation. *Opt. Comm.*, 128:325–340, 1996.

[91] J. M. Huntley. Random phase measurement errors in digital speckle pattern interferometry. *Opt. and Lasers in Eng.*, 26:131–150, 1997.

[92] M. Kujawinska. Spatial phase measurement methods. In D. W. Robinson and G. T. Reid, editors, *Interferogram Analysis: Digital Fringe Pattern Measurement Techniques*, pages 141–193. Institute of Physics Publishing, Bristol, 1993.

[93] R. Smythe and R. Moore. Instantaneous phase measuring interferometry. *Opt. Eng.*, 23:361–364, 1984.

[94] M. Kujawinska, L. Salbut, and K. Patorski. Three-channel phase stepped system for moire interferometry. *Appl. Opt.*, 30:1633–1635, 1991.

[95] O. Y. Kwon. Multichannel phase-shifted interferometer. *Opt. Letters*, 9:59–61, 1984.

[96] O. Y. Kwon and D. M. Shough. Multichannel grating phase-shift interferometers. *SPIE*, 599:273–279, 1985.

[97] O. Y. Kwon, D. M. Shough, and R. A. Williams. Stroboscopic phase-shifting interferometry. *Opt. Letters*, 12:855–857, 1987.

[98] M. Kujawinska and D. W. Robinson. Multichannel phase-stepped holographic interferometry. *Appl. Opt.*, 27:312–320, 1988.

[99] B. Barrientos, A. J. Moore, C. Pérez-López, L. L. Wang, and T. Tschudi. Transient deformation measurement with ESPI using a diffractive optical element for spatial phase-stepping. In W. Jüptner and W. Osten, editors, *Fringe '97*, pages 371–378. Akademie Verlag, Berlin, 1997.

[100] A. J. P. van Haasteren. *Real-time Phase Stepped Speckle Interferometry.* PhD thesis, Delft University of Technology, The Netherlands, 1994.

[101] A. J. P. van Haasteren and H. J. Frankena. Real-time displacement measurement using a multicamera phase-stepping speckle interferometer. *Appl. Opt.*, 33:4137–4142, 1994.

[102] A. L. Weijers, H. van Brug, and H. J. Frankena. Real-time phase-stepped shearing speckle interferometer for non-destructive testing. In W. Jüptner and W. Osten, editors, *Fringe '97*, pages 540–546. Akademie Verlag, Berlin, 1997.

[103] M. V. Berry. Disruption of wavefronts: statistics of dislocations in incoherent Gaussian random waves. *J. Opt. Soc. Am. A*, 11:27–37, 1978.

[104] N. B. Baranova, A. V. Mamaev, N. F. Pilipetsky, V. V. Shkunov, and B. Y. Zeldovich. Wave-front dislocations: Topological limitations for adaptive systems with phase conjugation. *J. Opt. Soc. Am.*, 73:525–528, 1983.

[105] N. Shvartsman and I. Freund. Speckle spots ride phase saddles sidesaddle. *Opt. Comm.*, 117:228–234, 1995.

[106] J. Burke, H. Helmers, C. Kunze, and V. Wilkens. Speckle intensity and phase gradients: Influence on fringe quality in spatial phase shifting ESPI-systems. *Opt. Comm.*, 152:144–152, 1998.

[107] D. W. Robinson. Phase unwrapping methods. In D. W. Robinson and G. T. Reid, editors, *Interferogram Analysis: Digital Fringe Pattern Measurement Techniques*, pages 194–229. Institute of Physics Publishing, Bristol, 1993.

[108] J. Morlet. Sampling theory and wave propagation. In C. Chen, editor, *NATO ASI Series, Issues in Acoustic Signal-Image Processing and Recognition*, pages 233–261. Springer, Berlin, 1983.

[109] A. Grossmann and J. Morlet. Decomposition of hardy functions into square-integrable wavelets of constant shape. *SIAM J. Math. Anal.*, 15:723–736, 1984.

[110] N. Hess-Nielsen and M. V. Wickerhauser. Wavelets and time-frequency analysis. *Proc. IEEE*, 84:523–540, 1996.

[111] P. Guillemain and R. Kronland-Martinet. Characterization of acoustic signals through continuous linear time-frequency representations. *Proc. IEEE*, 84:561–585, 1996.

[112] H. Rix and O. Meste. Fine structure of ecg signal using wavelet transform. In C.E. D'Attellis and E.M. Fernández-Berdaguer, editors, *Wavelet Theory and Harmonic Analysis in Applied Sciences*, pages 143–154. Birkhäuser, Boston, 1997.

[113] M. Unser and A. Aldroubi. A review of wavelets in biomedical applications. *Proc. IEEE*, 84:626–638, 1996.

[114] G. Beylkin. On wavelet-based algorithms for solving differential equations. In J. J. Benedetto and M. W. Frazier, editors, *Wavelets: Mathematics and Applications*, pages 449–466. CRC Press, Boca Raton, 1994.

[115] G. Beylkin, R. Coifman, and V. Rokhlin. Fast wavelet transforms and numerical algorithms I. *Comm. on Pure and Applied Mathematics*, 44:141–183, 1991.

[116] S. Mallat. Wavelets for a vision. *Proc. IEEE*, 84:604–614, 1996.

[117] P. Schröder. Wavelets in computer graphics. *Proc. IEEE*, 84:615–625, 1996.

[118] S.G. Mallat. A theory for multiresolution signal decomposition: The wavelet representation. *IEEE Transactions on Pattern Analysis and Machine Intelligence*, 11:674–693, 1989.

[119] S.G. Mallat. Multifrequency channel decompositions of images and wavelet models. *IEEE Transactions on Acoustics, Speech, and Signal Processing*, 37:2091–2110, 1989.

[120] M. Zeller. Flinkes Wellenspiel. *Computer Technik c't*, 11:258–264, 1994.

[121] R. De Vore, B. Jawerth, and B. Lucier. Image compression through wavelet transform coding. *IEEE Transactions on Information Theory*, 38:719–746, 1992.

[122] S. Wong, L. Zaremba, D. Gooden, and H.K. Huang. Radiologic image compression-a review. *Proc. IEEE*, 83:194–219, 1995.

[123] C.M. Brislawn. Fingerprints go digital. *Notices of the AMS*, 42:1278–1283, 1995.

[124] J.N. Bradley, C.M. Brislawn, and T. Hopper. The fbi wavelet/scalar quantization standard for grey-scale fingerprint image compression. *Visual Information Processing II*, 1961:293–304, 1993.

[125] I. Ouzieli and D. Mendlovic. Two-dimensional wavelet processor. *Appl. Opt.*, 35:5839–5846, 1996.

[126] D. Roberge and Y. Sheng. Optical wavelet matched filter. *Appl. Opt.*, 33:5287–5293, 1994.

[127] V. Dose, G. Venus, and H. Zohm. Wavelet analysis of fusion plasma transients. *Phys. Plasmas*, 4:323–328, 1997.

[128] E. Berger. *Anwendungen der Wavelet-Transformation in der Plasmaphysik*. PhD thesis, Julius-Maximilians-Universität, Würzburg, Germany, 1997.

[129] A. Dogariu, J. Uozumi, and T. Asakura. Wavelet transform analysis of slightly rough surfaces. *Opt. Comm.*, 107:1–5, 1994.

[130] G. H. Kaufmann. Speckle noise reduction in television holography fringes using wavelet thresholding. *Opt. Eng.*, 35:9–14, 1996.

[131] E. Berger, W. von der Linden, V. Dose, M. Ruprecht, and A. W. Koch. Approach for the evaluation of speckle deformation measurements by application of the wavelet transformation. *Appl. Opt.*, 36:7455–7460, 1997.

[132] E. Berger, W. von der Linden, V. Dose, M. Jakobi, and A. W. Koch. Reconstruction of surfaces from phase-shifting speckle interferometry: Bayesian approach. *Appl. Opt.*, 38:4997–5003, 1999.

[133] I. Daubechies. *Ten Lectures on Wavelets*. Society for Industrial and Applied Mathematics, Philadelphia, 1992.

[134] P. Goupillaud, A. Großmann, and J. Morlet. Cycle-octave and related transforms in seismic signal analysis. *Geoexploration*, 23:85–102, 1984.

[135] G. Kaiser. *A Friendly Guide to Wavelets*. Birkhäuser, Boston, 1994.

[136] J. Froment and S. Mallat. Second generation compact image coding with wavelets. In C. K. Chui, editor, *Wavelets - A Tutorial in Theory and Applications*, pages 655–678. Academic Press, Boston, 1992.

[137] A. K. Louis, P. Maaß, and A. Rieder. *Wavelets*. B. G. Teubner, Stuttgart, 1994.

[138] W. von der Linden, V. Dose, R. Fischer, and R. Preuss, editors. *Maximum Entropy and Bayesian Methods, Proceedings of the 18th International Workshop on Maximum Entropy and Bayesian Methods of Statistical Analysis, Garching, Germany, 1998.* Kluwer, Dordrecht, 1999.

[139] J. J. K. Ó Ruanaidh and W. J. Fitzgerald. *Numerical Bayesian Methods Applied to Signal Processing.* Springer, New York, 1996.

[140] D. S. Sivia. *Data Analysis - A Bayesian Tutorial.* Oxford University Press, Oxford, 1996.

[141] R. T. Cox. Probability, frequency and reasonable expectation. *Am. J. Phys.*, 14:1–13, 1946.

[142] T. Bayes. An essay towards solving a problem in the doctrine of chances. *Philos. Trans. R. Soc.*, 53:370–418, 1763.

[143] J. Bernoulli. *Ars conjectandi, opus posthumum. Accedit tractatus de seriebus infinitis et epistola Gallice scripta de ludo pilae reticularis.* Thurnisiorum, Basel, 1713.

[144] P. S. Laplace. *Théorie analytique des probabilités.* Courcier Imprimeur, Paris, 1812.

[145] H. Jeffreys. *Theory of Probability.* Oxford University Press, Oxford, 1961.

[146] L. Sachs. *Statistische Auswertungsmethoden.* Springer, Berlin, 1984.

[147] E. T. Jaynes. Prior probabilities. In R. D. Rosenkrantz, editor, *E. T. Jaynes: Papers on Probability, Statistics and Statistical Physics*, pages 114–140. Kluwer, Dordrecht, 1983.

[148] J. N. Kapur and H. K. Kesavan. *Entropy Optimization Principles with Applications.* Academic Press, San Diego, 1992.

[149] C. E. Shannon. A mathematical theory of communication. *The Bell System Tech. J.*, 27:379–423, 623–656, 1948.

[150] E. T. Jaynes. Marginalization and prior probabilities. In R. D. Rosenkrantz, editor, *E. T. Jaynes: Papers on Probability, Statistics and Statistical Physics*, pages 337–375. Kluwer, Dordrecht, 1983.

[151] J. Honerkamp, editor. *Stochastische Dynamische Systeme*. VCH, Weinheim, 1990.

[152] A. J. M. Garrett. Ockham's razor. In W. T. Grandy, Jr. and L. H. Schick, editors, *Maximum Entropy and Bayesian Methods*, pages 357–364. Kluwer, Dordrecht, 1991.

[153] M. Abramowitz and I. A. Stegun. *Handbook of Mathematical Functions*. Dover, New York, 1965.

[154] J. Meinguet. Multivariate interpolation at arbitrary points made simple. *ZAMP*, 30:292–304, 1979.

[155] Yu. I. Ostrovsky and V. P. Shchepinov. Correlation holographic and speckle interferometry. In E. Wolf, editor, *Progress in Optics*, pages 87–135. Elsevier, Amsterdam, 1992.

[156] G.V. Dreiden and I. V. Semenova. Correlation holographic interferometry applied for studies of laser-induced erosion. *Opt. Comm.*, 118:21–24, 1995.

[157] K. N. Petrov and Yu. P. Presnyakov. Holographic interferometry of the corrosion process. *Optics and Spectroscopy*, 44:179–181, 1978.

[158] C. S. Vikram. Holography of erosion, corrosion, and mechanical wear: possible role of phase-shifting interferometry. *Opt. Eng.*, 35:1795–1796, 1995.

[159] G. Gülker. *Deformations- und Korrelationsmessung an Denkmalgestein unter Feuchteeinfluß mit elektronischer Specklemuster Interferometrie (ESPI)*. PhD thesis, Carl von Ossietzky Universität Oldenburg, Germany, 1993.

[160] G. Gülker and K. D. Hinsch. Detection of surface microstructure changes by electronic speckle pattern interferometry. *Opt. and Lasers in Eng.*, 26:165–178, 1997.

[161] *Product Info*. FRT GmbH, Bergisch-Gladbach, Germany, 1999.

[162] M. Jakobi, P. Evanschitzky, and A. W. Koch. Räumliche Phase-Shifting-Speckle-Interferometrie mit vier Kameras. *Technisches Messen*, 67:155–159, 2000.

[163] M. Born and E. Wolf. *Principles of Optics*. Pergamon Press, 6. edition, Oxford, 1991.

[164] *Annual Report 1995.* Max-Planck-Institut für Plasmaphysik (IPP), Garching, 1996.

[165] *Product Info.* Zygo Corporation, Middlefield, Connecticut, 1997.

Acknowledgment - Danksagung

Dem Max-Planck-Institut für Plasmaphysik (IPP) in Garching und der Max-Planck-Gesellschaft gilt mein Dank, dass mir diese Arbeit ermöglicht wurde. Herrn Prof. Dr.-Ing. Alexander W. Koch (zu Beginn dieser Arbeit Universität des Saarlandes, jetzt Technische Universität München) danke ich für die Betreuung und die Begutachtung dieser Arbeit. Für die stete Unterstützung und die Übernahme des Zweitgutachtens möchte ich mich bei Herrn Prof. Dr. Rolf Wilhelm (IPP) bedanken. Bei Herrn Prof. Dr. Dr. h.c. Volker Dose (IPP) und allen Mitarbeitern des Bereichs Oberflächenphysik bedanke ich mich für die gute Zusammenarbeit. Ein ganz besonderer Dank geht an Frau Dr. Elke Berger für die gemeinsame Arbeit an der Oberflächenrekonstruktion. Herrn Dr.-Ing. Dipl.-Phys. Michael W. Ruprecht und Herrn Dipl.-Ing. Peter Evanschitzky möchte ich meinen Dank aussprechen für die vielen Diskussionen und Anregungen. Bei allen Mitarbeitern der Werkstätten des IPP, der Universität des Saarlandes und der Technischen Universität München, und ebenfalls bei Herrn Dipl.-Ing. Horst Franke und Frau Dipl.-Ing. Sabine Bassen möchte ich mich für die Anfertigung der mechanischen Komponenten bedanken. Bei Frau Siv Johansson-Hocke bedanke ich mich für die Diskussionen in Schwedisch und die Motivation zur Verbesserung meiner Sprachkenntnisse. Ein besonderer Dank gilt allen Studien- und Diplomarbeitern, die einen Beitrag zu dieser Arbeit geleistet haben. Frau Marianne Hansen danke ich für die sprachliche Korrektur dieser Arbeit. Mein ganz besonderer Dank gilt meiner Familie für die langjährige Unterstützung.

Publications

Journals and Conference Reports:

M. Jakobi, P. Evanschitzky, and A. W. Koch. Erosionsmessung an rauhen Oberflächen mittels Streifenkontrast in der Speckle-Interferometrie. In *Proceedings of XII. Meßtechnisches Symposium des Arbeitskreises der Hochschullehrer für Meßtechnik (AHMT)*, Universität des Saarlandes, Saarbrücken, pages 133-140, 1998.

M. Jakobi, P. Evanschitzky, and A. W. Koch. Erosionsmessung an rauhen Oberflächen mittels Streifenkontrast in der Speckle-Interferometrie. *Technisches Messen*, 66:163-168, 1999. (identical with AHMT 1998)

E. Berger, W. von der Linden, V. Dose, M. Jakobi, and A. W. Koch. Reconstruction of surfaces from phase-shifting speckle interferometry: Bayesian approach. *Applied Optics*, 38:4997-5003, 1999.

M. Jakobi, P. Evanschitzky, and A. W. Koch. Vier-Kamera-System zur in-situ Phase-Shifting-Speckle-Interferometrie. In *Proceedings of XIII. Meßtechnisches Symposium des Arbeitskreises der Hochschullehrer für Meßtechnik (AHMT)*, Universität Hannover, pages 5.1-5.8, 1999.

M. Jakobi, P. Evanschitzky, and A. W. Koch. Räumliche Phase-Shifting-Speckle-Interferometrie mit vier Kameras. *Technisches Messen*, 67:155-159, 2000.

IPP Annual Reports:

M. Ruprecht, M. Jakobi, and A. W. Koch. Speckle measurement of thermal deformation of graphite tiles. *Annual Report 1996*, Max-Planck-Institut für Plasmaphysik, Garching, page 151, 1997.

M. Jakobi, T. Krivosic, M. Ruprecht, P. Evanschitzky, and A. W. Koch. Measurement and simulation. *Annual Report 1997*, Max-Planck-Institut für Plasmaphysik, Garching, page 151, 1998.

M. Jakobi, P. Evanschitzky, J. Heinrich, and A. W. Koch. Spatial phase-shifting. *Annual Report 1998*, Max-Planck-Institut für Plasmaphysik, Garching, page 151, 1999.

M. Jakobi, P. Evanschitzky, and A. W. Koch. Detection of erosive areas. *Annual Report 1999*, Max-Planck-Institut für Plasmaphysik, Garching, page 152, 2000.